Scanning Tunneling Microscopy studies of single layer high-Tc cuprate Bi2Sr2-xLaxCuO6+delta

Author: Jihua Ma

Boston College Electronic Thesis or Dissertation, 2009

Boston College
The Graduate School of Arts and Sciences

Department of Physics

SCANNING TUNNELING MICROSCOPY STUDIES OF SINGLE LAYER HIGH-T_c CUPRATE $Bi_2Sr_{2-x}La_xCuO_{6+\delta}$

a dissertation
by

JIHUA MA

submitted in partial fulfillment of the requirements
for the degree of
Doctor of Philosophy

August 2009

SCANNING TUNNELING MICROSCOPY STUDY ON SINGLE LAYER HIGH-T$_c$ CUPRATE $\mathbf{Bi_2Sr_{2-x}La_xCuO_{6+\delta}}$

JIHUA MA

Dissertation Co-advisor: Dr. Hong Ding

Dissertation Co-advisor: Dr. Vidya Madhavan

ABSTRACT

High temperature superconductivity has been one of the most challenging problems in condensed matter physics since its discovery. This dissertation presents systematic studies on the single layer high temperature superconductor $Bi_2Sr_{2-x}La_xCuO_{6+\delta}$ by scanning tunneling microscopy. The STM results have been compared to Angle-resolved photoemission spectroscopy (ARPES) data.

Using STM spectroscopy and ARPES we observed two distinct gaps that coexist both in real space and in the antinodal region of momentum space, below the superconducting transition temperature. By looking at the energy scale of these two gaps along with the temperature dependence data, we find that the small gap is associated with superconductivity. The large gap persists above T$_c$, and seems linked to observed charge ordering. We also find a strong correlation between the large and small gaps suggesting that they are affected by similar physical processes.

This is the first time that two coexisting and competing energy scales have been directly observed in STM spectroscopy. Combining this with ARPES data, we show that the pseudogap may be a different order parameter from the superconducting phase. This provides support to the recently proposed "two gaps scenario" and should lead to more experimental discovery and theoretical discussions.

In this dissertation we also discuss the spatial properties of the scanning tunneling microscopy conductance maps, as well as the charge ordering pattern at high energies. We observe interesting periodic patterns at low energies which can not be explained by a simple charge density wave picture. We also find the surprising bias dependence

in terms of the contrast reversal. We propose a model of STM measuring effect to explain these phenomena.

To my family.

Acknowledgments

This thesis would not have been completed without the help of many individuals.

First of all, I would like to thank my advisor Professor Hong Ding, for his guidance of my adventure into the vast high-temperature superconductivity field. Hong is unique in his comprehension and implementation of the theory that complements his experimentalist's intuition. Therefore, he has supported both the theoretical and experimental aspects of the thesis project, which makes this Ph.D. experience exceptional.

I would like to express my deep gratitude to my co-advisor Professor Vidya Madhavan, for the enlightening discussion, her constant encouragement, and incomparable optimism despite frequent setbacks with instrumentation. And the results of which always pushed me to become an ever better scientist.

My deep thanks also go to Professor Ziqiang Wang, for his continual willingness to give any help and the beneficial discussions with him.

I want to thank Professor Rein Uritam, Professor Zhifeng Ren, Professor Cyril P. Opeil, Professor Baldassare Di Bartolo, Professor Willie J. Padilla and Dr. Andrzej Herczynski for their kind help while I was teaching assistant to their courses.

I also want to thank my friend Alan Vachon in the machine shop who spent so much time giving me advice and critiquing my designs, thanks also go to Paul Mazrimas in the electronics shop for his advice and patience.

Thanks go to my former labmates, who doubled as friends and teachers, Shancai, Hongbo, Asoka, Mandar, Janhavi and Pierre. Thanks also go to other members of Ding group and Madhavan group, Zhihui, Madhab, Yiming, Francis, Shankar, Wenchen and Dimitiri for their kind assistance in my experiments.

I want to thank many of my peer graduate students, for their friendship and the help in various situations, especially, Chunhua Li, Yi Ma, Xiaowei Wang, Feng Cai, Jian Yang and Bo Yu.

I am deeply indebted to my parents, my parents-in-law, and my sister for their

continuous support, endless patience and encouragements through all these years, especially the hard time during my study at Boston College.

Finally, and most importantly, this thesis is for my dear wife, Weihua Zhou and our daughter Yanyi. They make my life really colorful, meaningful, enjoyable and complete.

Contents

List of Figures

List of Tables

Chapter 1

Introduction to high T_c cuprates

It has been more than 20 years since the discovery of the first copper-oxide high-temperature superconductor $La_{2-x}Ba_xCuO_4$ by J. G. Bednorz and K. A. Müller in 1986 [5] and 75 years after the great discover of superconductivity by Onnes in 1911 [43]. Despite the great efforts on both theoretical and experimental fronts the mechanism of high temperature superconductivity (HTSC) still remains elusive.

In this chapter, we review basic properties of the cuprate superconductors and look into current theoretical and experimental progress.

1.1 Crystalline structure and phase diagram

After the discovery of the new high T_c superconductor family: Fe-based superconductor in 2008 [27], the term of 'high T_c superconductor' no longer applies to only the cuprates, We emphasize that this thesis only focuses on the high T_c cuprates. In this section we will review the crystalline structure and phase diagram of High T_c cuprates.

1.1.1 Crystalline structure of the high T_c cuprates

All the cuprate superconductors have layered perovskite structure. The common structural unit is the CuO_2 plane, which is believed to hold the key for superconductivity. The primary differences between the variety of cuprates are in layered scheme of the CuO_2 planes and how charges are introduced into them.

Figure 1.1 shows the crystallographic structure of a prototypical high T_c cuprate $Bi_2Sr_2CaCu_2O_{8+\delta}$. All the planes except calcium oxide plane are square lattices and formed by oxygen and corresponding elements.

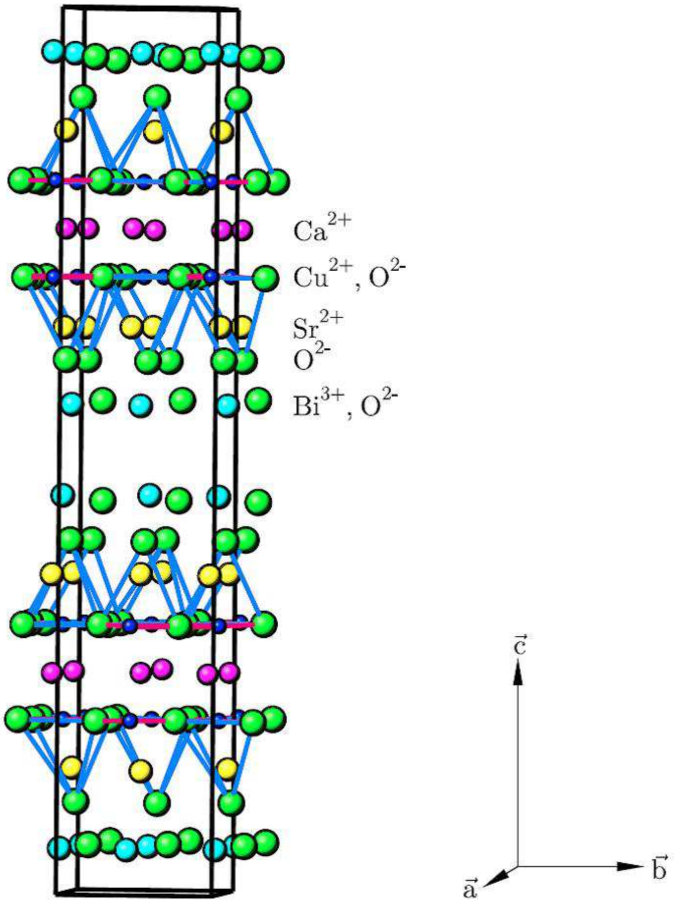

Figure 1.1: Crystalline structure of $Bi_2Sr_2CaCu_2O_{8+\delta}$

Most of the cuprates studied to date are hole-doped materials. According to their parent compounds, they can be classified into the following families:
Bismuth family-$Bi_2Sr_2Ca_{n-1}Cu_nO_{2n+4+\delta}$
Lanthanum family-$La_{2-x}(Ba,Sr)_xCuO_{4+\delta}$
Yttrium family-$YBa_2Cu_{2+n}O_{6+n+\delta}$
Thallium Mercury family-$(Tl,Hg)_2Ba_2Ca_{n-1}Cu_nO_{2n+4+\delta}$.
Table s 1.1 shows the critical temperature of a few compounds in these families.

Table 1.1: Critical temperature of some cuprates

Compound	T$_c$ at optimal doping (K)
$Bi_2Sr_2Ca_{n-1}Cu_nO_{2n+4+\delta}$	
n=1 (2201)	∼10
n=2 (2212)	85
n=3 (2223)	110
$La_{2-x}M_xCuO_{4+\delta}$ (M=Ba, Sr, Ca)	38
$RBa_2Cu_{2+n}O_{6+n+\delta}$ (R=Y, La, Nd, Sm, Eu, Ho, Er, Tm, Lu)	
n=1 (123)	92
n=1.5 (247)	95
n=2 (124)	82
$(Tl,Hg)_2Ba_2Ca_{n-1}Cu_nO_{2n+4+\delta}$	
n=1 (2201)	85
n=2 (2212)	105
n=3 (2223)	125
$Nd_{2-x}Ce_xCuO_{4-y}$ (electron doped)	30
$Ba_{1-x}K_xBiO_3$	30
$Pb_2Sr_2Y_{1-x}Ca_xCu_3O_8$	70

1.1.2 Electronics structure of high T$_c$ cuprates

As shown in Figure 1.2, in the parent compound (undoped cuprates), the Cu atom in the plane is in the $3d^9$ configuration. Due to the octahedral crystal field, the $3d$ states split into two degenerate states, a doubly degenerate e_g state and a triply degenerate t_{2g} state. The presence of oxygen and the associated Jahn-Teller distortion split the e_g orbital of Cu further into $3d_{x^2-y^2}$ and $3d_{3z^2-r^2}$. The t_{2g} states also split into $3d_{xy}$, $3d_{xz}$ and $3d_{yz}$ states. All the states are fully occupied except the $3d_{x^2-y^2}$ which is half filled.

The Cu $d_{x^2-y^2}$ orbital and the doubly occupied O p_x, p_y orbitals form a strong covalent bonding. In the absence of interaction among electrons, the hybridization of these three orbitals will build bonding and half-filled anti-bonding bands which

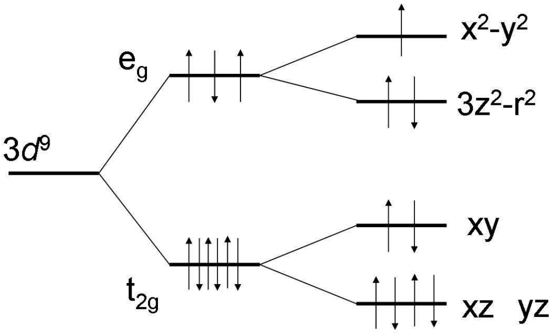

Figure 1.2: $3d$ orbitals configuration.

predicts a good metal instead of the large charge gap observed in the undoped compounds. But is the interaction among electrons really absent? It is not!

The failure of band theory, and hence that of conventional Fermi liquid approach to high T_c problems, stems from the existence of a large on-site Coulomb interaction (U) that well exceeds the bandwidth (W) of the tight-binding anti-bonding band. The band splits into an upper Hubbard band (UHB) and lower Hubbard band (LHB). The LHB is fully filled and UHB is empty. The energy difference is called Mott Gap which can be a few electrovolts and the system becomes an insulator (Mott insulator). The unpaired spins are anti-ferromagnetically aligned via the super-exchange interaction that involves virtual hopping to the neighboring O p orbitals. As a result, the parent compounds are anti-ferromagnetic Mott insulators.

The mechanism of how the Mott insulators become superconducting is still not clear yet. But it is well recognized that the transition happens when the charge carries are added to the parent compounds. Typically charge carriers in the form of holes are added by doping oxygen (e.g. $Bi_2Sr_2CaCu_2O_{8+\delta}$), by substituting a monovalent atom with a divalent atom (e.g. replacing La with Sr in $La_{2-x}Sr_xCuO_4$), or by removal of oxygen from their stoichiometric positions (e.g. $YBa_2Cu_3O_{7-\delta}$). More discussion on theoretical models will be introduced later.

1.1.3 Phase diagram of high T$_c$ cuprates

The current state of the understanding of high T$_c$ can be summarized by the generic phase diagram, as shown in Figure 1.3. This is only applicable to the hole-doped cuprates, where x is the number of holes per Cu and T is the temperature.

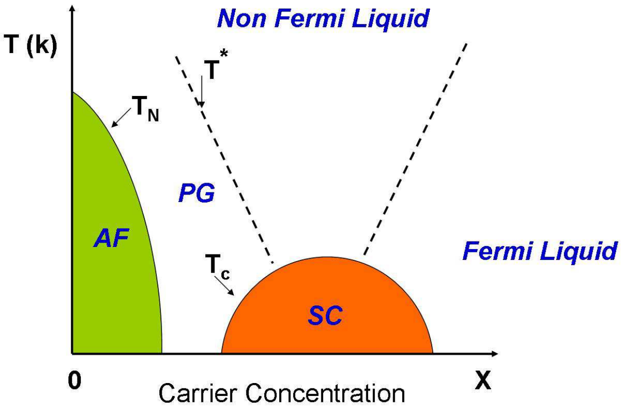

Figure 1.3: The phase diagram of hole doped high T$_c$ cuprate

There are several important phases and phase boundaries, as marked in the figure. When x is close to zero, the system is in a long-range, anti-ferromagnetic state (AF) below the Néel temperature T$_N$. The AF state is destroyed when more holes are doped into the Cu-O$_2$ plane, and superconductivity (SC) emerges as x exceeds 0.05. The transition temperature (T$_c$) has a characteristic dome shape that peaks around x=0.15 and ends at x=0.05 and x=0.25.

The AF and SC states are the only well defined phases in the phase diagram. In the underdoped regime, a so called "pseudogap" (PG) phase appears below a poorly defined crossover temperature T*. The nature of the PG phase and its relation to the SC phase has been one of the central issues of recent debate. And for samples with very high hole concentration, conventional Fermi liquid behavior starts to reappear. We will revisit these phases in the following sections.

1.2 Review of current theoretical and experimental status

To solve the puzzle of the high temperature superconductivity, physicists have been working on both theoretical and experimental fronts for more than 2 decades. Many theoretical models have been proposed and a huge amount of experimental data has been published.

In this section, a brief introduction to the theoretical progress will be made. We then go on to the highlights of recent experimental data.

1.2.1 Theoretical models of high T_c cuprates

To understand superconductivity was not easy. It was not until half a century after the discovery of superconductivity that the understanding of superconductivity was advanced by three American physicists, John Bardeen, Leon Cooper, and John Schrieffer. Their theory of superconductivity is known as the BCS Theory [4]. The BCS theory shows that electrons form Cooper pairs, despite the fact that electrons have the same charge and they are repelled by each other. When the atoms of the lattice oscillate, the cooper pair is pulled together or pushed apart without a collision. Once the two electrons are bound into a cooper pair, they no longer behave like Fermions but as one boson. They can therefore condense into a lower energy state.

BCS theory predicts a theoretical maximum to T_c of around 30 - 40 K for phonon based pairing. Above this temperature, thermal energy would cause electron-phonon interactions of an energy too high to allow formation of Cooper pairs. While BCS worked well for the conventional superconductors, once it met the challenge of HTSC in 1986 [5], the difficulties became life-threatening.

The breakdown of the BCS theory is mainly due to strong interactions between electrons in these systems [1], in particular the strong Coulomb repulsion between valence electrons at the same atomic site, or so called electron correlation U. Such a system with strong on-site electron-electron interactions is also called a highly correlated electron system. Any reliable theoretical calculation for a highly correlated system is extremely difficult, given its many-body nature, which can not be reduced to a single quasiparticle picture.

So far theorists have proposed dozens of new models, trying to solve the mystery of High T_c superconductivity. However they are still far from explaining everything.

Among all the new theories, one promising approach is based on the idea of a doped resonant valence bond (RVB) state, first proposed by Philip Anderson [3].

In 1987, Anderson revived his earlier work on a possible spin-liquid state in a frustrated antiferromagnet. He named this state resonating valence bond (RVB) [3]. RVB has no long-range antiferromagnetic order and is a unique spin-singlet ground state. It has spin -1/2 fermionic excitations which are called spinons. The idea is that when doped with holes, the RVB is a singlet state with coherent mobile carriers and is indistinguishable in terms of symmetry from a singlet BCS superconductor, RVB expands the life of BCS theory into the field of HTSC.

Other competing theories include those based on fluctuating stripes [28], SO(5) theory [19], and theories based on polarons (strong coupling between electrons and phonons) [13]. Recently most theorists seem to have reached agreement that the starting point of the physics of HTSC is the physics of the doping of a Mott insulator. Strong correlation is the driving force behind the phase diagram.

To calculate, the simplest model is the Hubbard model and its strong-coupling limit, the t-J model.

$$H = -\sum_{<i,j>,\sigma} t_{ij} c^{+}_{i\sigma} c_{j\sigma} + J \sum_{<i,j>} (\mathbf{S_i} \cdot \mathbf{S_j} - \frac{1}{4} n_i n_j) \tag{1.1}$$

where n_i is the number operator. The one band $t - J$ model captures the essence of the low energy electronic excitations of the Cuprates.

1.2.2 Experimental study of high T$_c$ cuprates: ARPES

With major improvements of resolution in electron spectrometers and photon flux of light sources, ARPES has played a powerful role in the field of high T$_c$ superconductivity, and made significant contributions to our understanding of underlying physics.

ARPES is the first experimental probe that made the observation of a large Fermi surface that satisfies Luttinger theorem, suggesting that the high T$_c$ cuprates are doped Mott insulators [12] [15] [16]. ARPES also made the discovery of an extended Van Hove singularity in high T$_c$ cuprates. The enhancement of density of states due to this singularity has significant influence to many-body interactions [25]. ARPES found the convincing evidence for the d-wave symmetry of the superconducting order parameter. Along with phase sensitive experiments, this ARPES finding has been widely cited as for the establishment of *d*-wave order parameter with nodes along (0,0)-(π,0) direction [48] [17] [18].

ARPES was the first tool to make the discovery of a pseudogap in the normal state of high T$_c$ cuprates. The pseudogap has since become one of the most studied phenomena in the high T$_c$ cuprates field [14]. ARPES also made the observation of spectral dip and dispersion kink, revealing possible collective (either magnetic or phonon) modes which may respond to pairing glue in the high T$_c$ cuprates [41] [33].

1.2.3 Experimental study of high T$_c$ cuprates: STM

For more than ten years, scanning tunneling microscopy (STM) has been playing an important role in the experimental physics in High T$_c$ field. STM studies have made many remarkable contributions to this field such as the gap inhomogeneity, electronic properties of the vortex cores, the observation of quasiparticle interference, and the observation of pseudogap. In this section we will quickly go through some of the primary STM results. The full review can be found in Fisher *et al.* [22].

Since Scanning Tunneling microscopy is an experimental technique that probes local properties. STM was critical to revealing the inhomogeneity of gap size in real space [27] [32] [37]. Figure 1.4 concludes the results. We also observed the inhomogeneity of the gap size in single layered BSCCO which will be presented in Chapter 4.

Scanning tunneling microscopy observed the existence of pseudogap in the high temperature Bi2212 and Bi2201. As the temperature is raised from T<T$_c$ the superconducting gap Δ_{sc} remains constant and smoothly evolves into a pseudogap across T$_c$.

By applying a magnetic field, STM is also able to observe the vortex state. The evolution of the spectra across a vortex core in overdoped Bi2212 is shown in Figure 1.5 [30]. When entering the core, the spectra evolve in the same way as when the temperature is raised above T$_c$. In this sense the vortex core spectroscopy provide new insights into the understanding of the pseudogap.

A single spectrum is not adequate to provide the global information of a material. Using local density of states mapping STM has observed periodic local density of states modulations, and this phenomena can be divided into two classes: one with dispersing wavelength and the other does not disperse. The dispersing one is due to quasi particle interference [36](Figure 1.6). The non-dispersing spatial modulation have been observed in the pseudogap state at high temperature, at low doping, or

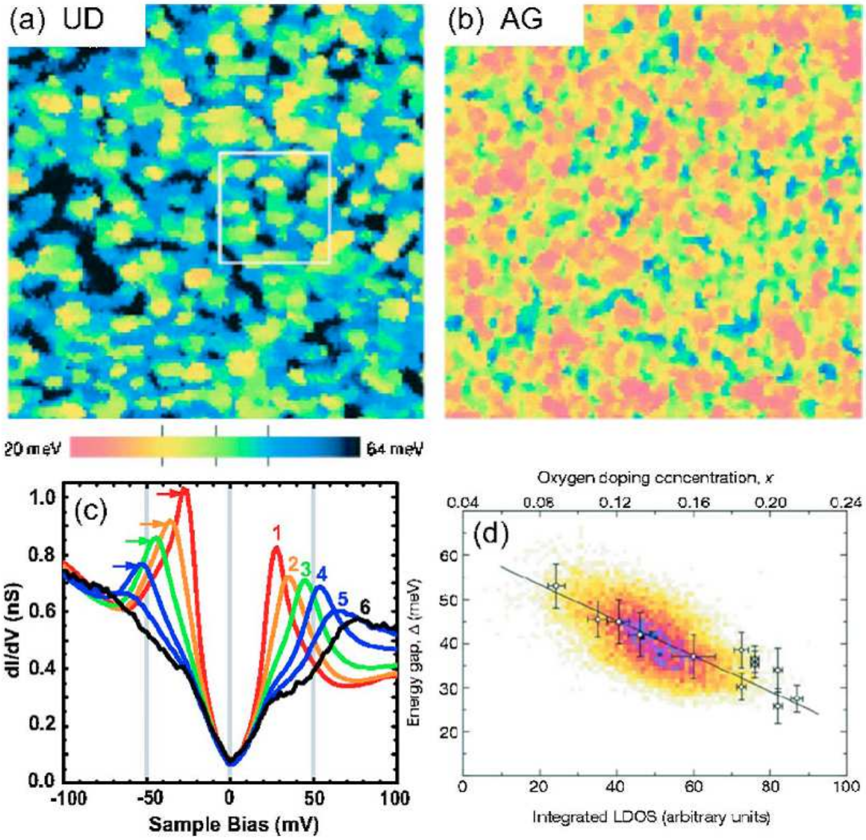

Figure 1.4: 560 Å × 560 Å maps of the spatial gap distribution in (A) underdoped and (B) as grown Bi2212 single crystals. Adapted from Lang *et al.* 2002. [32] (C) Range of tunneling conductance spectra measured on inhomogenneous superconducting Bi2212. From McElory *et al.* 2005. [37] (D) Scatter plot of the superconducting gap versus the integrated local DOS inoptimally doped Bi2212. From Pan *et al.* 2001. [27]

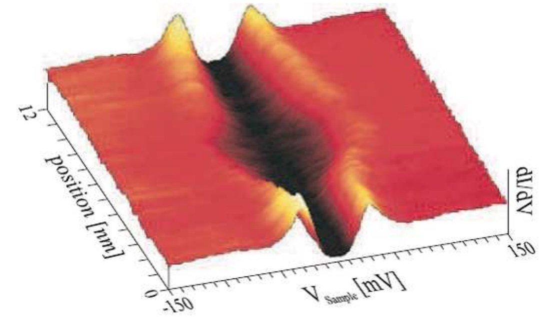

Figure 1.5: Conductance spectra taken along a 12nm path across a vortex core in overdoped Bi2212 (T$_c$=77K) at T=2.6K and H=6T. The spectra acquired at the center of the core reveal a pseudogap-like similar to the one observed above T$_c$. From Kugler *et al.* 2000. [30]

in the vortex cores. In chapter 6, we will present our data on the observation of the local density state modulation on La-Bi2201 samples, we will also come back to the findings on Bi2212 and make a comparison.

At the beginning, physicists focused on the easiest and most outstanding data could be collected from STM experiments such as the gap magnitue, the spatial properties. Then the experiments were expanded to the temperature dependence and doping dependence on all kinds of materials. Recently, along with the improvement of the energy resolution and spatial resolution, more and more physicists are trying to connect their data to other techniques and theoretical models. More and more analysis methods have been used and discussed as well.

There is one paper published by Davis' group recently can be an example [14]. By imaging the electronic structure of $Bi_2Sr_2CaCu_2O_{8+\delta}$ in real space and $\vec{k}$ space simultaneously, Kohsaka *et al.* demonstrated that the unusual real space excitation exists in the pseudogap state. Thus, as the Mott insulating state is approached by decreasing the hole density, the delocalized Copper pairs vanish from $\vec{k}$ space, to be replaced by locally translational- and rotational-symmetry-breaking pseudogap states in real space.

Another example can be taken from the work presented by the Yazdani's group [26]. Over a wide range of doping from 0.16 to 0.22, K. Gomes *et al.* found that pairing gaps nucleate in nanoscale regions above T$_c$. Despite the inhomogeneity, they observed that every pairing gap develops locally at a temperature T$_p$, following the

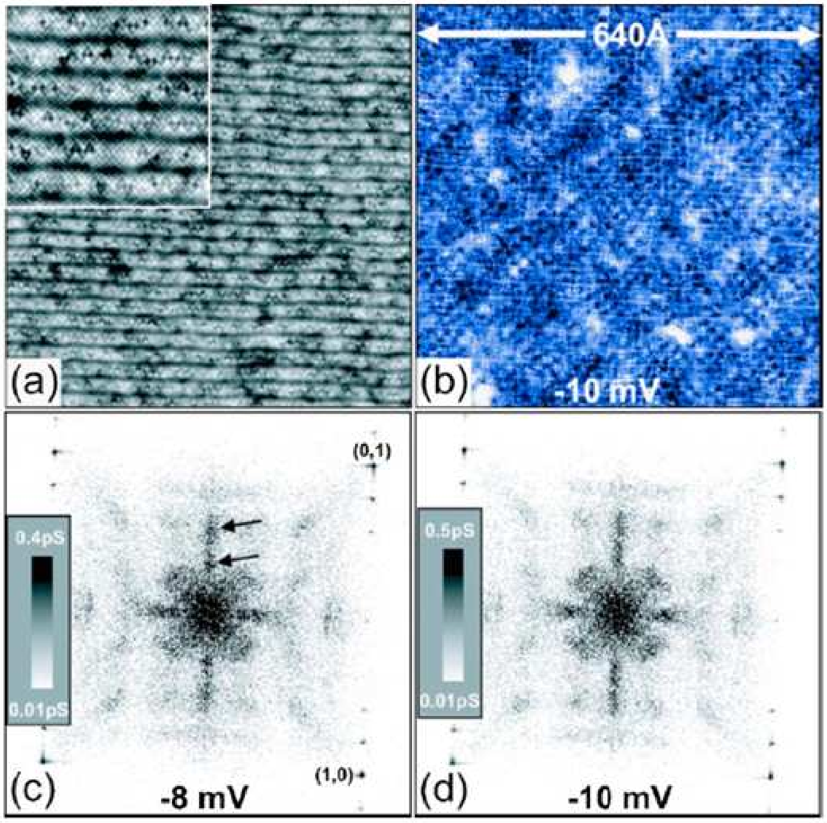

Figure 1.6: (A) Atomic resolution image of a 640 Å × 640 Å region on near optimally doped Bi2212. Inset: 160 Å × 160 Å magnification. (B) Conductance map of the same field view acquired at V=-10mv. (C) and (D) FFT of conductance maps at -8 and -10mv, respectively. The square of intense points near the corners of each panel corresponding to the atomic lattice, and the arrow in (C) indicate the q vectors of the supermodulation. These two sets of spots do not disperse with energy. The maps clearly show an addition pattern with fourfold symmetry. The corresponding wave vectors disperse in energy. From McElroy *et al.* 2003. [36]

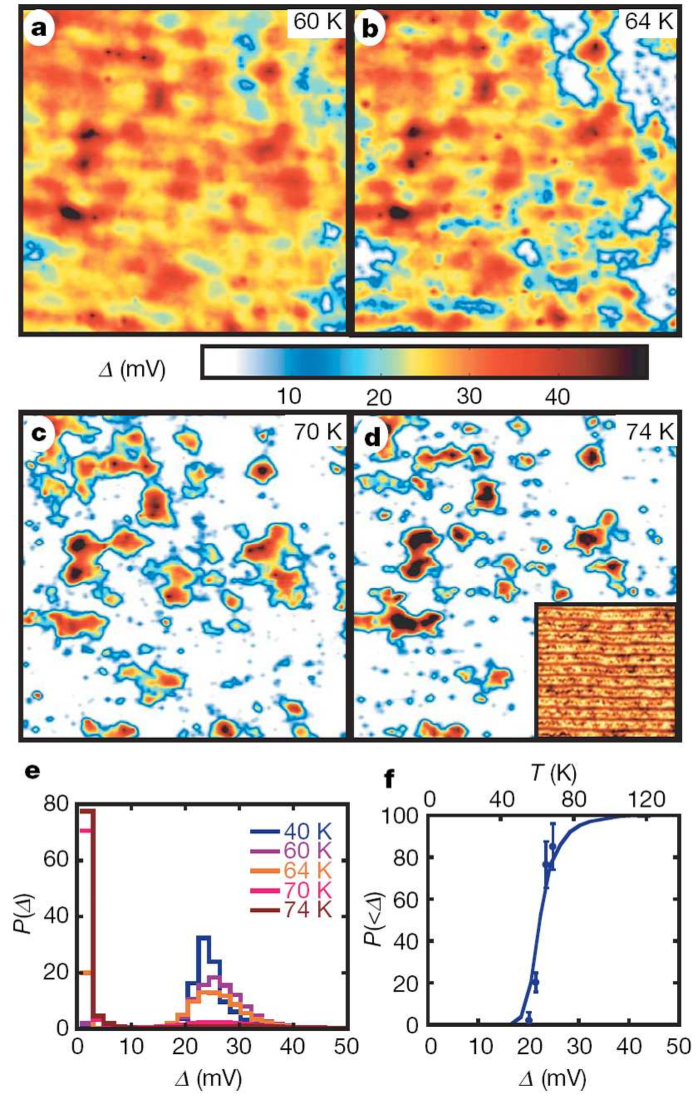

Figure 1.7: Gap evolution for overdoped (T$_c$=65K) Bi2212 samples. (A)-(D). Gap maps taken on the same 300$\mathring{A}$ area of an OV65 sample at different temperature near T$_c$. (E) The probability of finding a gap of a given size (gap distribution) for the gap maps shown in (A)-(D) and an additional gap map taken at 40K. (F) The probability P(<Δ) that the gaps are less than a given Δ (lower x axis). From K. Gomes *et al.* 2007. [26]

relation $2\Delta/K_BT_p$=7.9±0.5. At very low doping (≤0.14), systematic changes in the DOS indicate the presence of another phenomenon which is unrelated and perhaps competes with electron pairing, as shown in Figure 1.7.

Besides these great STM contributions, we must not forget the many great discoveries made by other experimental groups which have not been discussed here due to space and time constraints. This active field continues to progress both theoretically and experimentally. With the improvement of the STM system in terms of spatial and energy resolution, data acquiring techniques and new analysis methods, we believe the scanning tunneling microscopy will continue make remarkable contribution to the experimental side of this field.

1.3 Summary

In this chapter we introduced the concept of high T_c cuprate superconductor. We briefly went through current theoretical models have been proposed. We also browsed experimental data mainly by STM and ARPES experiments. In the next chapter we will look into the further details of these two experimental techniques.

Bibliography

[1] A. A. Abrikosov *et al*, Methods of Quantum Field Theory in Statistical Mechanics, **Dover Publications, Inc.**, New York, (1963).

[2] G. Aeppli *et al*, Science. **278**, 1432 (1997).

[3] P. W. Anderson *et al*, Science **235**, 1196 (1987).

[4] J. Bardeen, L. N. Copper and J. R. Schrieffer, Phys. Rev. **108**, 1175 (1957).

[5] J. G. Bednorz and K. A. Müller, Z. Phys. B. - Condensed Matter **64**, 189 (1986).

[6] . P. Bogdanov, *et al*, Phys. Rew. Lett. **89** 167002 (2002).

[7] P. C. Canfield and S. L. Bud'ko Scientific American **80**, April (2005).

[8] S.-W. Cheong *et al*, Phys. Rev. Lett. **67**, 1791 (1991).

[9] Y. -D. Chuang, *et al*, Phys. Rew. Lett. **87** 117002 (2001).

[10] P. Dai, *et al*, Physica C **243**(3-4), 201 (1995).

[11] P. Dai *et al*, Phys. Rev. B **63**, 054525 (2001).

[12] D. S. Dessau *et al*, Phys. Rev. Lett. **71**, 2781 (1993).

[13] T. P. Devereaux *et al*, Phys. Rev. Lett. **93**, 117004 (2004).

[14] H. Ding *et al*, Natuer **382**, 51, (1996).

[15] H. Ding *et al*, Phys. Rev. Lett. **76**, 1533 (1996).

[16] H. Ding *et al*, Phys. Rev. Lett. **78**, 2628 (1997).

[17] H. Ding *et al*, Phys. Rev. Lett. **74**, 2784 (1995).

[18] H. Ding *et al*, Phys. Rev. B **54**, R9678 (1996).

[19] A. Dorneich *et al*, Phys. Rev. Lett. **88**, 057003 (2003).

[20] H. Eisaki, *et al*, Phys. Rew. B **69** 064512 (2004).

[21] D.-L. Feng, *et al*, Phys. Rew. Lett. **86**, 5550 (2001).

[22] O. Fischer *et al*, Rev. Mod. Phys. **79**, 353 (2007).

[23] K. Fujita *et al*, Phys. Rev. Lett. **95**, 097006 (2005).

[24] M. Fujita *et al*, Phys. Rev. B **70**, 104517 (2004).

[25] K. Gofron *et al*, Phys. Rev. Lett. **73**, 3302 (1994).

[26] K. Gomes *et al*, Nature **447**, 569 (2007).

[27] Y. Kamihara *et al*, J. Am. Chem. Soc. **130**, 3296 (2008).

[28] S. A. Kivelson *et al*, Nature **393**, 550 (1998).

[29] Y. Kohsaka *et al*, Nature **454**, 1072 (2008).

[30] M. Kugler *et al*, Rev. Sci. Instrum. **71**, 1475 (2000).

[31] M. Kugler *et al*, Phys. Rev. Lett. **86**, 4911 (2001).

[32] K. M. Lang *et al*, Nature **415**, 412 (2002).

[33] A. Lanzara *et al*, Nature **412**, 510 (2001).

[34] A. G. Loeser, *et al*, Science **273**, 325 (1996).

[35] H. Luo, *et al*, Supercond. Sci. Technol. **21** 125024 (2008).

[36] K. McElory *et al*, Nature **422**, 592 (2003).

[37] K. McElory *et al*, Phys. Rev. Lett. **94**, 197005 (2005).

[38] W. Meevasana *et al*, Phys. Rev. Lett. **96**, 157003 (2006).

[39] W. Meissner and R. Ochsenfeld, Naturwissenschaften **21** 787 (1933).

[40] H. A. Mook *et al*, Phys. Rev. Lett. **70**, 3490 (1993).

[41] M. R. Norman, *et al*, Phys. Rew. Lett. **79**, 3506 (1997).

[42] Y. Okada, *et al*, J. Phys. Soc. Japan **77** 074714 (2008).

[43] Onnes, H. K., Commun. Phys. Lab. **12**, 120 (1911).

[44] S. H. Pan *et al*, Nature **413**, 282 (2001).

[45] S. H. Pan *et al*, Appl. Phys. Lett. **73**, 2992 (1998).

[46] P. Richard, *et al*, Phys. Rew. B **74** 094512 (2006).

[47] C. Renner *et al*, Phys. Rev. Lett. **80**, 149 (1998).

[48] Z.-X. Shen *et al*, Phys. Rev. Lett. **70**, 1553 (1993).

[49] J. A. Slezak, *et al*, Proc. Natl. Acad. Sci. **105** 3203 (2008).

[50] S. Tajima *et al*, Phys. Rev. B **43**, 10496 (1991).

[51] J. M. Tranquada *et al*, Nature **375**, 561 (1995).

[52] M.K. Wu, Phys. Rev. Lett. **58**, 908 (1987).

[53] K. Yamada *et al*, Phys. Rev. B **57**, 6165 (1998).

Chapter 2

Experimental techniques: STM and ARPES

Scanning tunneling microscopy was invented in 1982 by Binnig and Rohrer, for which they shared the 1986 Nobel prize in physics. In this chapter we will review the physics treatment of scanning tunneling microscopy. We will also review another experimental techniques: ARPES.

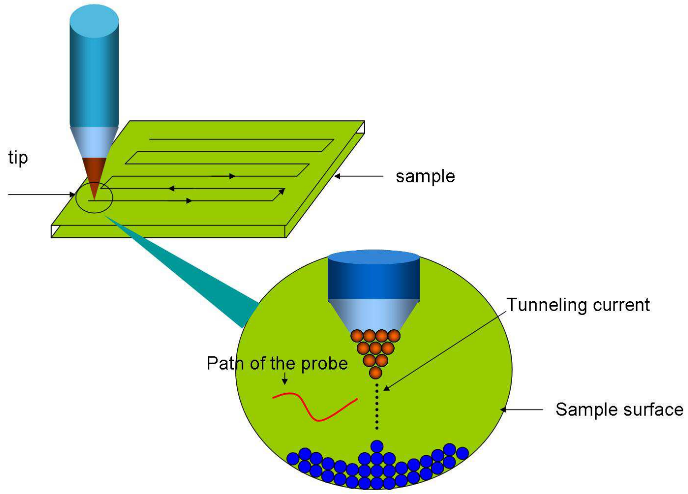

Figure 2.1: Schematic drawing of STM tip and sample.

2.1 Scanning tunneling microscopy

The core part of a scanning tunneling microscopy system consists of a sharp conducting tip which is used to scan a flat conducting or semi-conducting sample surface. When the distance between the tip and the sample is within the tunneling range and a voltage V is applied between them, a current will flow and this current can be measured as a function of (x,y) location and as a function of V. Figure 2.1 shows the basic idea schematically.

2.1.1 Calculation of tunneling current

The tip-sample current is based on quantum tunneling and the tunneling current can be calculated as following:

If the sample is biased by a positive voltage +V with respect to the tip, this effectively raises the Fermi level of the tip with respect to the sample. Electrons will flow out of the filled states of the tip into the empty states of sample as shown in Figure 2.2.

Using time independent perturbation theory the tunneling current from the filled states of tip to the empty states of sample, integrate over all energies ε (with respect to the Fermi level of the sample) can be written as:

$$I_{tip\rightarrow sample} = -2e\frac{2\pi}{\hbar}\int_0^{eV} |M|^2(\rho_t(\varepsilon)f(\varepsilon))(\rho_s(\varepsilon - eV)[1-f(\varepsilon - eV)])\,d\varepsilon \tag{2.1}$$

Where the factor of 2 is for spin, -e is the electron charge. $\hbar$ is the planck constant, $|\mathrm{M}|^2$ is the matrix element, $\rho_{s(t)}(\varepsilon)$ is the density of states of the sample (tip), and f(ε) is the Fermi distribution.

Although the overall flow direction of the electron is from the tip to the sample, there is also a smaller amount of tunneling from the sample to the tip:

$$I_{sample\rightarrow tip} = -2e\frac{2\pi}{\hbar}\int_0^{eV} |M|^2(\rho_t(\varepsilon)[1-f(\varepsilon)])(\rho_s(\varepsilon - eV)f(\varepsilon - eV))\,d\varepsilon \tag{2.2}$$

We sum these two currents and get rid of the Fermi function by going to T=0. We get the total tunneling current below:

$$I \approx -\frac{4\pi e}{\hbar}\int_0^{eV} |M|^2\rho_t(\varepsilon)\rho_s(\varepsilon - eV)\,d\varepsilon \tag{2.3}$$

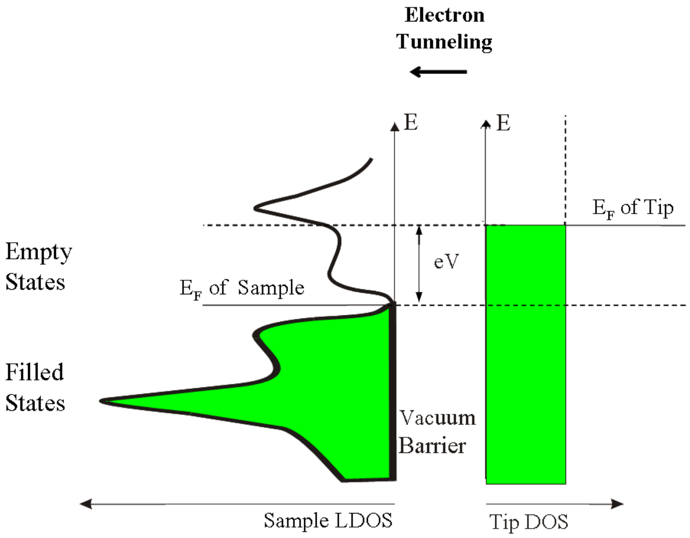

Figure 2.2: Schematic of tunneling current. Energy is along the vertical axis, and the density of states of the tip and sample are shown along the horizontal axis. Filled states are shown in red. In this case, a negative bias voltage -V has been applied to the sample, which effectively raises its Fermi level by eV with respect to the Fermi level of the sample. This allows for filled states on the right (Tip) to tunnel into empty states on the left (Sample).

In the Bardeen theory the matrix element |M| is the expectation value of the single-particle current in the direction z normal to the plane of the junction, through a surface S lying entirely in the barrier region [1]:

$$|M| = -\frac{\hbar}{2m}\int_S (\varphi_\rho^* \frac{\partial \varphi_\lambda}{\partial z} - \varphi_\lambda \frac{\partial \varphi_\rho^*}{\partial z})\, dS \tag{2.4}$$

Because of the lateral confinement, the one-electron states of the STM tip cannot be characterized by a single momentum in the (x,y) plane. Tersoff and Hamman proposed an expression for |M|, represented the tip apex by a spherical potential well and found that Bardeen's matrix element is proportional to the sample wave function at the center x of the tip apex [27] [28]:

$$|M|^2 \propto |\varphi_\rho(x)|^2 \tag{2.5}$$

2.1.2 Scanning tunneling microscopy data-sets

Basically there are two main type of scanning modes for measurements: constant current mode and constant height mode.

Compared to the constant height mode, the constant current mode invloves a feedback loop. The tunneling current which usually ranges from 0.01mA to 50mA is converted into a voltage by a current amplifier. To get a linear response with respect to the tunneling gap (the current is exponentially dependant on the tip-sample distance, see the text of last equation.) the signal is processed by a logarithmic amplifier. The output of the logarithmic amplifier is compared with a predetermined voltage which is used as a reference current. The error signal is passed to feedback electronics, which applies a voltage to the z piezo to keep the difference between the current set point and the tunneling current small. Constant current is more popular and safer, although constant height mode will provide faster scanning speed since there is no extra time taken by the feedback loop. So it can be a efficient choice for a very flat sample surface. In this thesis, all the data were acquired under constant current mode to ensure the safety and data quality.

Under constant current mode, we employ a feedback loop which controls the voltage on the piezo to keep the tunneling current constant. By recording the voltage value, we can effectively map the height of the surface, and because the material studied in this thesis has well known atomic resolution and lattice constant, obtaining a clear topographic image with good atomic resolution usually is our first step when we approach on a fresh sample or/and with a fresh tip to ensure the data quality.

Using the STM in spectroscopy mode, we can also measure the differential conductance dI/dV to get the local density of states (LDOS). From the equation (2.3) we know the tunneling current I is proportional the integrated local density of states (ILDOS). Therefore the derivative of the ILDOS (dI/dV) is proportional to the LDOS.

Usually people choose a tip material which has a flat density of states within the energy range of the Fermi surface that we wish to study, tips like W or Pt that are used in STM experiments. The matrix element $|\mathrm{M}|^2$ is also assumed to be independent of energy. So we arrive at that the tunneling current I proportional to the integrated local density of states (ILDOS) of the sample. Therefore the derivative of the ILDOS (dI/dV) will proportional to the LDOS of the sample. We employ a lock-in amplifier to measure dI/dV. A voltage modulation dV is applied to the bias, a resulting response in current dI is measured. Figure 2.3 shows a schematic of STM spectroscopy.

In our experiments, the bias voltage is always applied on the sample, as shown in Figure 2.3. When the bias voltage is negative, the electrons are moving from the filled states of the sample to the empty states of the tip, so we are actually measuring the filled states of sample considering the flat density of state of tip. And when the bias voltage is positive, the electrons are flowing from the filled states of the tip to the empty states of the sample, we are measuring the empty states of the sample.

Usually a detailed DOS map (dI/dV map) with high spatial resolution and energy resolution will be desired. In this thesis, the main type of data are dI/dV maps. Some high quality linecuts were also taken and presented.

2.2 Angle-resolved photoemission spectroscopy

When light impinges on solids, an electron in a solid can absorb a photon and be excited into an unoccupied state. If photon energy is high enough, electrons will get out of the surface and go into vacuum. This photoelectric phenomenon was first discovered by Hertz in 1887, which was explained later by A. Einstein in 1905, with quantization of light. Experimentally photoelectrons are analyzed with respect to their kinetic energy E and their momentum **p**. Given the energy of light and work function, the binding energy of electrons before excitation can be determined by:

$$|E_B| = h\nu - \phi - E_{kin} \tag{2.6}$$

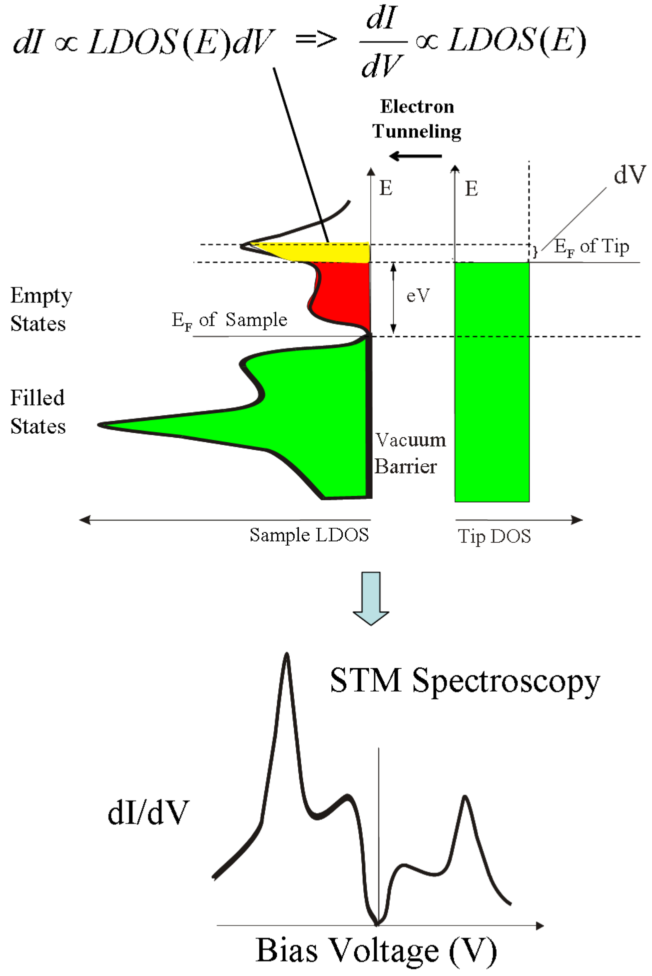

Figure 2.3: The dI/dV is proportional to the LDOS.

where $h\nu$ is the incident photon energy, ϕ is the work function of the solid and E_{kin} is the kinetic energy of photoelectrons.

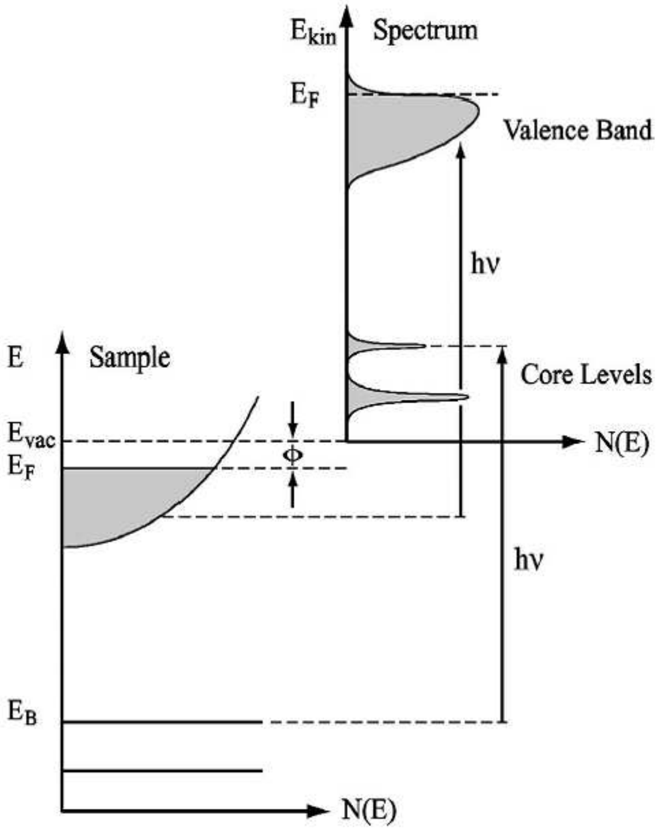

Figure 2.4: Photoemission spectroscopy. Electrons with binding energy E_B absorbs an photon $\hbar\nu$ and escapes into vacuum becoming an photoelectron with kinetic energy $E_{kin} = \hbar\nu - \phi - E_B$.

As shown in Figure 2.4, in the case of metal, core levels are at high binding energies and non-dispersing, valence bands are at low binding energies and the Fermi energy E_F is at the top of valence band and separated from vacuum by the work function ϕ. If an electron with a binding energy E_B absorbs an photon with energy $\hbar\nu$, the electron can excited into vacuum and an photoelectron can be detected with a kinetic energy $E_{kin} = \hbar\nu - \phi - E_B$. The kinetic energy distribution of photoelectrons reflects the binding energy distribution of the electrons in solids, and can reveal detailed information about the electronic structure of solids. Based on photoelectric effect, photoemission spectroscopy(PES) was developed and has been widely used in studying the electronic structure of solids.

Figure 2.5 shows schematically an ARPES setup, including a light source, a sample, and a detector. When photons impinge on the surface of a sample, electrons in solid can absorb photons and escape into vacuum, which are called photoelectrons and will be collected by the detector with energy and angle resolution.

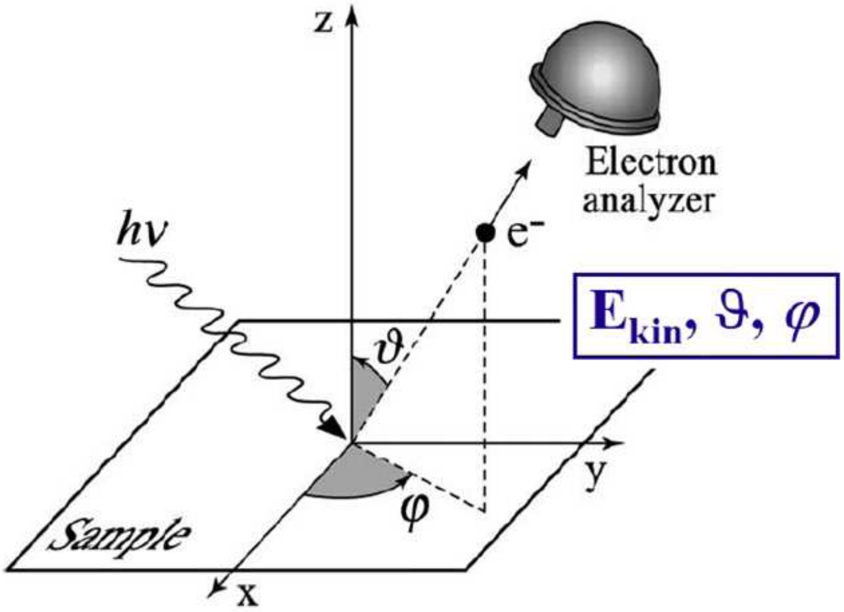

Figure 2.5: Schematic ARPES experiment. Photon with energy $\hbar\nu$ impinges on the surface of samples. Electrons can absorb photon and will be excited into vacuum. Those photoelectrons will be analyzed with respect to energy and momentum by an electron analyzer.

The kinetic energy E_{kin} can be measured and the momentum of photoelectrons can be derived by $p = \sqrt{E_{kin}/2m}$. During the process of photoemission, the energy E and parallel momentum $k_{//}$ are conserved and can be expressed as below in terms of the kinetic energy E_{kin} and angle θ, ϕ:

$$k_x = \frac{1}{\hbar}\sqrt{2mE_{kin}} sin\theta cos\phi \tag{2.7}$$

$$k_y = \frac{1}{\hbar}\sqrt{2mE_{kin}} sin\theta sin\phi \tag{2.8}$$

ARPES measures the electron distribution $I(E_{kin}, \theta, \phi)$ with respect to E_{kin}, θ and ϕ, there is one-to-one mapping to $I(\omega, k_x, k_y)$. The intensity map $I(\mathbf{k}, \omega)$ can be described as:

$$I(\mathbf{k}, \omega) = A(\mathbf{k}, \omega) f(\omega) I_0(\mathbf{k}, \omega, \mathbf{A}) \tag{2.9}$$

where $A(\mathbf{k}, \omega)$ is the single particle spectral function, $f(\omega)$ the Fermi-Dirac distribution function and $I_0(\mathbf{k}, \omega, \mathbf{A})$ the magnitude of matrix element $|M_{f,i}(\mathbf{k})|^2$.

Figure 2.6 shows a typical 2-dimensional intensity map $I(\mathbf{k}, \omega)$. The x-axis is the momentum and y-axis is the energy, the value gives the counting of photoelectrons at that momentum and energy.

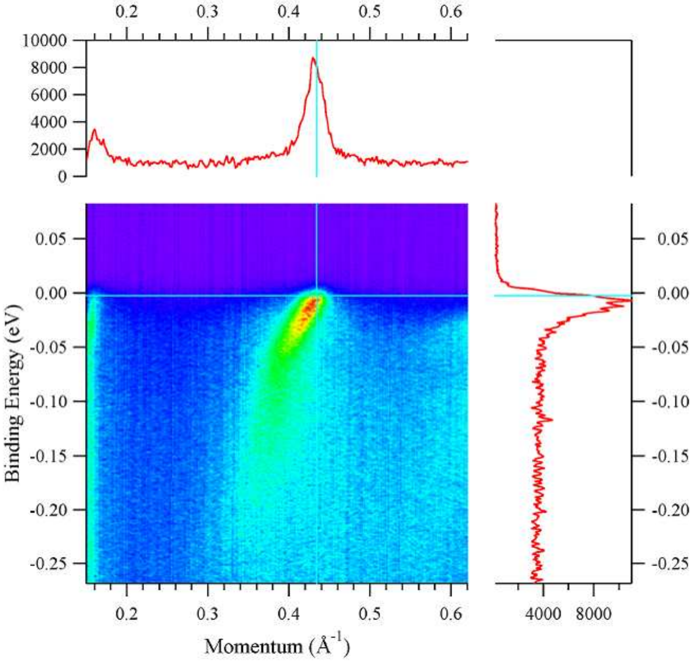

Figure 2.6: ARPES intensity map. The image plot is a typical ARPES intensity map. The upper panel is the MDC line. The right one is the EDC line.

ARPES has made significant contributes to the experimental condensed matter physics over the last two decades, a good summary can be found in the review articles [5] [23], we also need to notice that there are a few caveats when we compare it to STM:

(1) ARPES works well only on $2d$ systems. If the electrons in the materials are moving with an z component in their momentum, then it is more difficult to

reconstruct the z-axis dispersion relation.

(2) ARPES measures spatially averaged quantity. Therefore, all of the spatial dependence study on high temperature superconductors, such as electronic inhomogeneity, impurity and vortices states, are difficult to be detected by ARPES.

(3) ARPES measures mostly filled states, thus the information of empty states above the Fermi level is missing from ARPES measurement.

(4) ARPES can't work with a magnetic field, due to the interference of magnetic field and electron motion.

In summary, STM gives us the energy landscape in real space and ARPES gives us the energy landscape in $\vec{k}$ space, which makes them a perfect match for the study of the high T_c superconductivity.

2.3 Summary

In summary, this chapter we document the physics treatment of tunneling microscopy. We also compare it to ARPES, which is another important experimental technique in high temperature superconductivity field. Both STM and ARPES are surface sensitive techniques which require clean, flat surfaces for effective study. In next chapter we will start to look into the basic instrumentation of a scanning tunneling microscopy system including UHV subsystem, cryogenics subsystem, electronics subsystem and STM head.

Bibliography

[1] J. Bardeen *et al*, Phys. Rev. Lett. **6**, 57 (1961).

[2] Berglund, C. N., and Spicer, W. E., Phys. Rev. **136**, A1030 (1964).

[3] C. Berthier *et al.*, Journal de Physique I **6**, 2205 (1996).

[4] G. Binnig *et al*, Phys. Rev. Lett. **49**, 5761 (1982).

[5] Damascelli, A., Hussain, Z. and Shen, Z. -X., Rev. Mod. Phys. **75**, 473 (2003).

[6] A. Einstein, Ann. Physik **17** 132 (1905).

[7] Fan, H. Y., Phys. Rev. **68**, 43 (1945).

[8] Feibelman, P. J., and Eastman, D. E., Phys. Rev. B **10**, 4932 (1974).

[9] H. F. Fong *et al.*, Nature **398**, 588 (1999).

[10] H. Hertz, Ann. Physik **31** 983 (1887).

[11] Hüfner, S., "Photoelectron Spectroscopy", (Springer-Verlag, Berlin, 1995).

[12] H. Kambara *et al*, Rev. of Sci. Insturm. **78**, 073703 (2007).

[13] B. Khaykovich *et al.*, Physical Review B **66**, 014528 (2002).

[14] J. D. Koralek *et al.*, Phys. Rev. Lett. **96**, 017005 (2006).

[15] B. Lake *et al.*, Science **291**, 1759 (2001).

[16] G. D. Mahan Phys. Rev. **B**, 4334 (1970).

[17] V. F. Mitrovic *et al.*, Nature **413**, 501 (2001).

[18] H. A. Mook*et al.*, Phys. Rev. Lett.**88**, 097004 (2002).

[19] S. H. Pan *et al*, International Patent Publication NUmber WO **93**, 19494 (1993).

[20] S. H. Pan *et al*, Rev. Sci. Instrum. **70**, 1459 (1999).

[21] A. Rigamonti *et al.*, Reports on Progress in Physics **61**, 1367 (1998).

[22] Seah, M. P. and Dench, W. A., Surf. Interface Anal. 1, 2 (1979).

[23] Z. X. Shen, arXiv:cond-mat/0305576

[24] S. Souma, T. Sato, and T. Takahashi, Rev. of Sci. Instrument **78**, 123104 (2007).

[25] J. A. Stroscio *et al*, Phys. Rev. Lett. **57 20**, 2579 (1986).

[26] M. Takigawa *et al.*, Phys. Rev. Lett. **73**, 1287 (1994)

[27] J. Tersoff *et al*, Phys. Rev. Lett. **50**, 1998 (1983).

[28] J. Tersoff *et al*, Phys. Rev. B **31**, 805 (1985).

[29] T. Valla *et al.*, Science **285**, 2110 (1999).

[30] J. J. Yeh *et al.*, Atom. Data Nucl. Data Tabl. **32**, 1 (1985).

Chapter 3

Experimental setup and sample preparation

Building and trouble-shooting a scanning tunneling microscopy system operating at cryogenic temperature and in ultra high vacuum is part of this thesis. In this chapter we will review the instrumentation of this system along with a commercial STM system which is also located in Boston College. Most of our data has been taken using these two systems. In this chapter, we first describe the STM setup, and then we discuss the sample preparation procedures.

3.1 Instrumentation of STM

In this section, we will briefly review the instrumentation of the STM system, starting from the STM head which is the core part of the system. As a complete experimental system, the home made STM system can be divided into a few subsystems: the electronics subsystem, UHV subsystem and cryogenics subsystem.

3.1.1 STM head

There are a variety of distinct STM designs. In general, they differ in how the coarse approach is implemented and in their rigidity against vibrations. We adopted Pan's STM design with some variation [28] [30]. Pan's design employs a modified "Stick-slip" coarse approach mechanism that exploits the friction between parts to hold the unit against vibrational noise coupling.

As shown in Figure 3.1, the STM head consists of a macor housing (1), six shear-piezo stacks (2) with alumina contacts (3), a sapphire prism (4) that carries the scanning unit, a BeCu spring plate (7). The scanning unit is made of a macor inset (5), a piezo-tube scanner (6), and a metallic tip holder. The metallic tip holder is attached to the center of the piezo-tube scanner, and the scanner is glued to the top of the macor inset with Torr-Seal. The macor piece fits tightly to the central hole of the sapphire prism, and the scanning unit is locked to the sapphire with screws and Torr-Seal. By pressing down a 1/8" diameter sapphire ball (8) against the top macor block (1), the BeCu spring plate (7) holds the sapphire prism firmly between the six piezo stacks. All of the materials chosen are non-magnetic and UHV compatible.

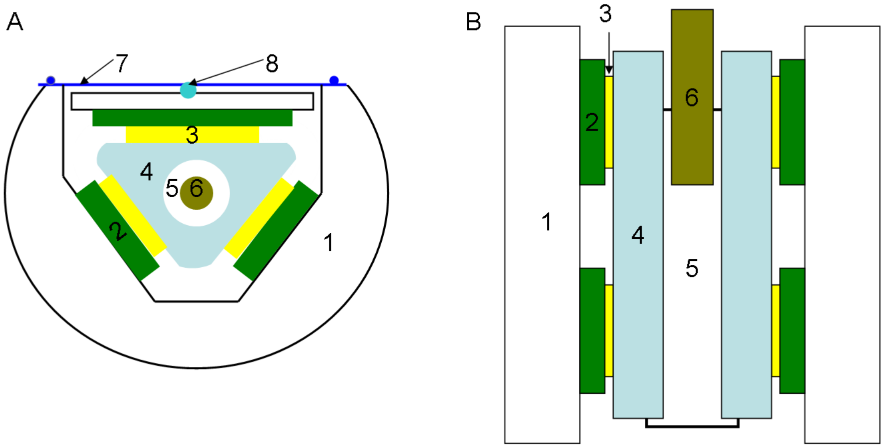

Figure 3.1: Schematic drawing of STM head. (A) Top view. (B) Side View. (1) Macor body. (2) Shear-piezo stacks. (3) Alumina plate contacts. (4) Sapphire prism. (5) Macor inset of the scanning unit. (6) Piezo-tube scanner. (7) BeCu spring plate. (8) Sapphire ball bearing.

This design is superior in its stability against external mechanical perturbations. The sapphire prism and the tip it carries are held steady by friction between the alumina contacts and the prism. The strength of the friction can be adjusted by varying the curvature of the thin BeCu spring plate. Therefore, there is very little relative motion between the macor body and the tip. Furthermore, after each step completed, all piezos return to their neutral positions. Thus, no voltage is needed to hold the prism in place, and the vibrational noises transmitted through the voltage noise applied to the piezos are eliminated.

One additional advantage of the design is its stability against thermal expansion. The STM head is designed to be concentric with the tip and sample located at the center. Therefore, it minimizes thermal drifting and enhances the STM performance at variable temperatures. The piezo stacks and piezo tube take care of all the motions needed by piezoelectric effect.

Although this whole delicate apparatus is only about half palm size, I still want to divide them into two parts according to their functions: Walker and Scanner.

Walker The walker consists of all the parts in Figure 3.1 except part 5 and 6. The six piezo stacks do the coarse approach whose schematic drawing is shown in Figure 3.2.

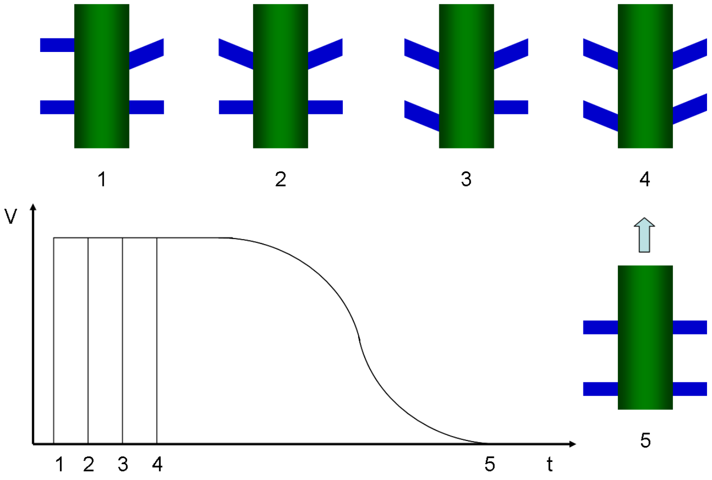

Figure 3.2: Schematic drawing of the working principle of the piezo stacks for the coarse approach: The sequence of the motions of shear piezo stacks and sapphire prism is caused by applying the sequence of voltage to each piezo stacks.

As shown in Figure 3.2, four stacks of piezo holds the sapphire prism. When a voltage is applied to one of them, it shears while the friction force between the other three stacks and the prism is still strong enough to hold the prism stationary. After an appropriate delay, the same voltage applied to one of the other stacks. After all the stacks have been sheared, the voltage on all stacks is ramped down, simultaneously. The stacks carry the prism one step forward together.

Scanner The scanner basically includes the part 5 and part 6 in Figure 3.1, A detailed drawing of scanner is shown in Figure 3.3 and a schematic drawing of the piezo tube is shown in Figure 3.4. By applying voltages to the X, Y and Z sections of the tube, the tube can make fine XYZ motions during the scanning.

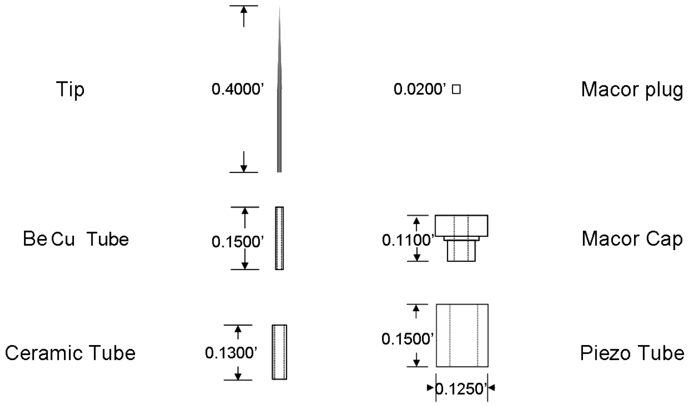

Figure 3.3: Detailed drawing of the scanner.

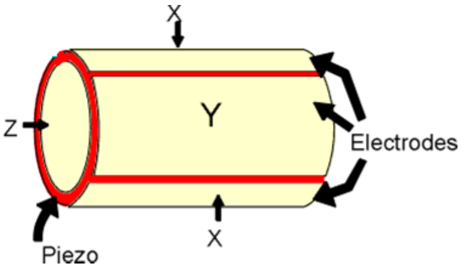

Figure 3.4: Schematic drawing of the Piezo tube.

3.1.2 STM electronic, UHV and cryogenics subsystems

Electronic subsystem The electronic subsystem takes care of STM control and data-acquisition. It consists of a high-gain low-noise current pre-amplifier, a controller and a homemade triggering circuit that controls the coarse approach piezos. The pre-amplifier and controller box are commercial products from RHK Technologies.

UHV subsystem UHV subsystem has three stages, as shown in Figure 3.5.

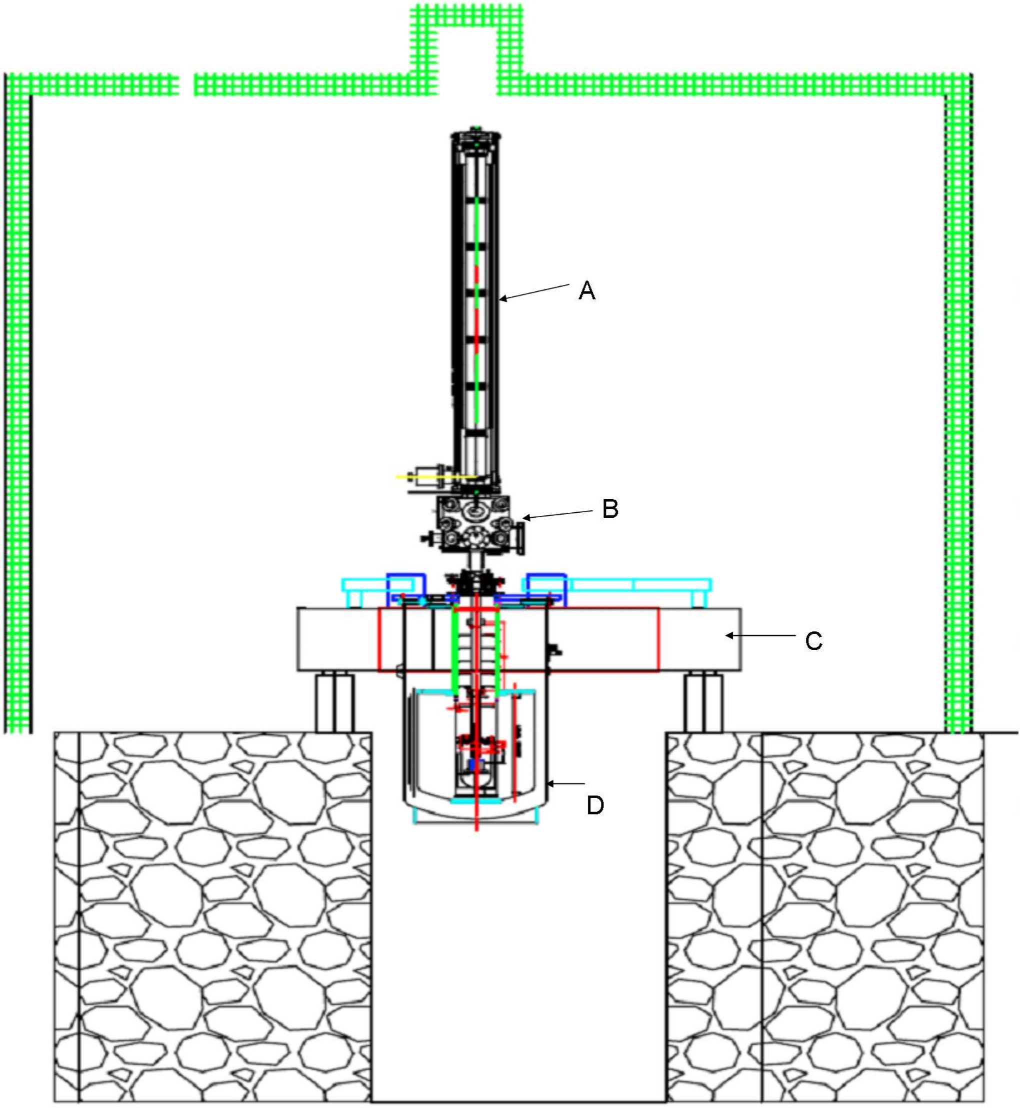

Figure 3.5: Detailed drawing of UHV subsystem (A) the manipulator on the second stage, (B) main chamber for second stage, (C) the vibration isolation table and (D) the dewar which shield the third stage.

The first stage or so called “Loadlock stage” has a six-way cross(a small volume chamber also will work) connected with four main parts: a turbo pump which supported by a rough pump, pressure gauge (here a pirani and a full range ion gauge do the job), a short transfer arm or manipulator and a easy-access door (the easy-access door can replaced by a simple flat flange cover, which provides better vacuum but need to be removed for sample transfer making it rather inconvenient.). The vacuum ranges from 10E-7 to 10E-9 Torr depending on how long it has been pumped. It may also need the bakeout for better vacuum performance.

The second stage consists a big chamber connected to the loadlock, ion pump, ion gauges, sample post magazine and the cleaver along with the pin basket, This stage is mainly for sample storage and cleaving. The pressure is always maintained below 10E-10 torr and even better. Ion pump’s speed is more than 300L/s.

The third stage is the last stage, and this one also can be referred as cold stage which includes the manipulator which can transfer the sample to the STM head. It has a shutter/valve separating the cold stage from other stages and we keep it shut during the experiment. Not only for isolating the different spaces due to the vacuum (cryo-pumping), the noise and thermal influences are also considered here.The cold stage’s pressure could be better than 10E-12 Torr although we do not have a gauge here since no gauge can measure these pressure. Unlike other stages, a thermal sensor is definitely needed and is placed on the STM head.

Another kind of detailed design for a versatile ultralow temperature scanning tunneling microscopy system can be found in the H. Kambara *et al.* [13]

Cryogenics subsystem The cryogenics subsystem has two parts, as shown in Figure 3.6.

One is the dewar whose volume is more than 80L. The dewar is accompanied by helium level sensor, thermal sensor and a heater for the variable temperature control. The boil off rate at 4.2K is about 10L/day. The other part is the exchange gas can. Usually there are two basic designs according to the thermal medium which help to adjust the STM head’s temperature. One is using liquid and the other is using gas. We choose the helium gas as the thermal medium for our homemade STM system. And on the top of this part, the pressure is being monitored using a regular pirani gauge. Usually the pressure will be around a few torr to 10E-2 torr. The lowest temperature is 4.2K (liquid helium temperature).

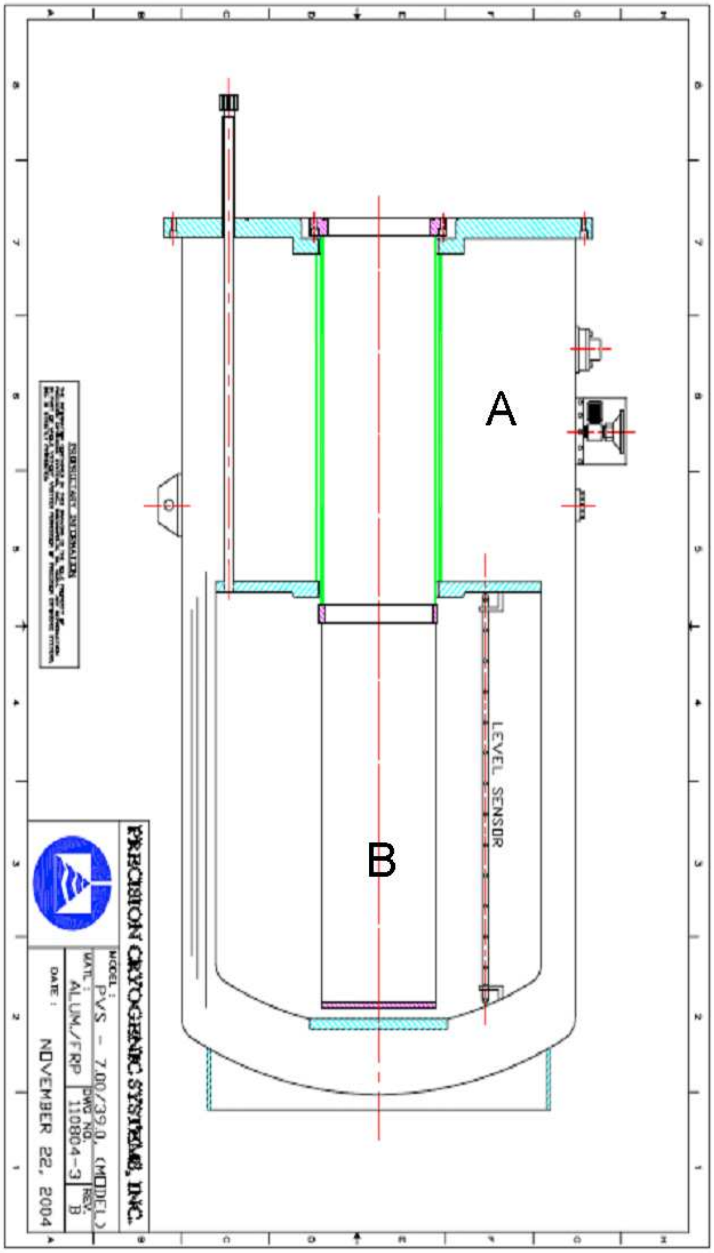

Figure 3.6: Detailed drawing of (A) the dewar and (B) exchange gas can.

3.1.3 STM systems at Boston College STM lab

In the last section we discussed the instrumentation of our home-made STM system. At Boston College, we have another commercial STM from Unisoku. These two STM systems share a lot in common such as sample preparation, approaching mechanism, controller boxes. The commercial Unisoku STM system also has the ability to go below 4K, there are extra parts designed for pumping down the Helium vapor.

The picture of the homemade STM system is shown in Figure 3.7. Figure 3.8 shows the topographic image using homemade STM system took on the optimal doped Bi2212 sample. The picture of the commercial Unisoku STM system is shown in Figure 3.9.

3.2 Experimental environment

Because bismuth family including $Bi_2Sr_{2-x}La_xCuO_{6+\delta}$ has weak bonds between the two BiO layers, so it can be easily cleaved to achieve an atomically flat surface. And because the STM approaches the sharp tip within a few Angstroms to the sample surface, it is very essential that the surface be atomically flat. So the following are two requirements for STM study of a surface.

(1) The surface must cleave between layers, make sure there is no residual parts of a missing layer which will cause a huge step of the surface and make a mess with the signals.

(2) The surface must be free from other contaminants, such as helium and water molecules.

To satisfy the requirements above, we cleave the $Bi_2Sr_{2-x}La_xCuO_{6+\delta}$ sample while it is in a UHV environment, the vacuum is usually better than 2E-10Torr. Cleaving is mechanically simple. We glue a small sample to the copper sample holder and glue a small metallic rod to the other side of the sample, then we insert the whole setup into the system and knock off the rod when the vacuum is ready. Figure 3.10 shows the typical cleaved surface after the experiment.

Right after cleave, the sample is inserted to the STM head which sitting in the cryogenics environment. Because of the cryo-pumping, the vacuum is much better than the cleave stage (<1E-11Torr). So the quality of the surface is guaranteed after a successful cleave. A sample in the cryogenic UHV environment can be used for weeks and even months.

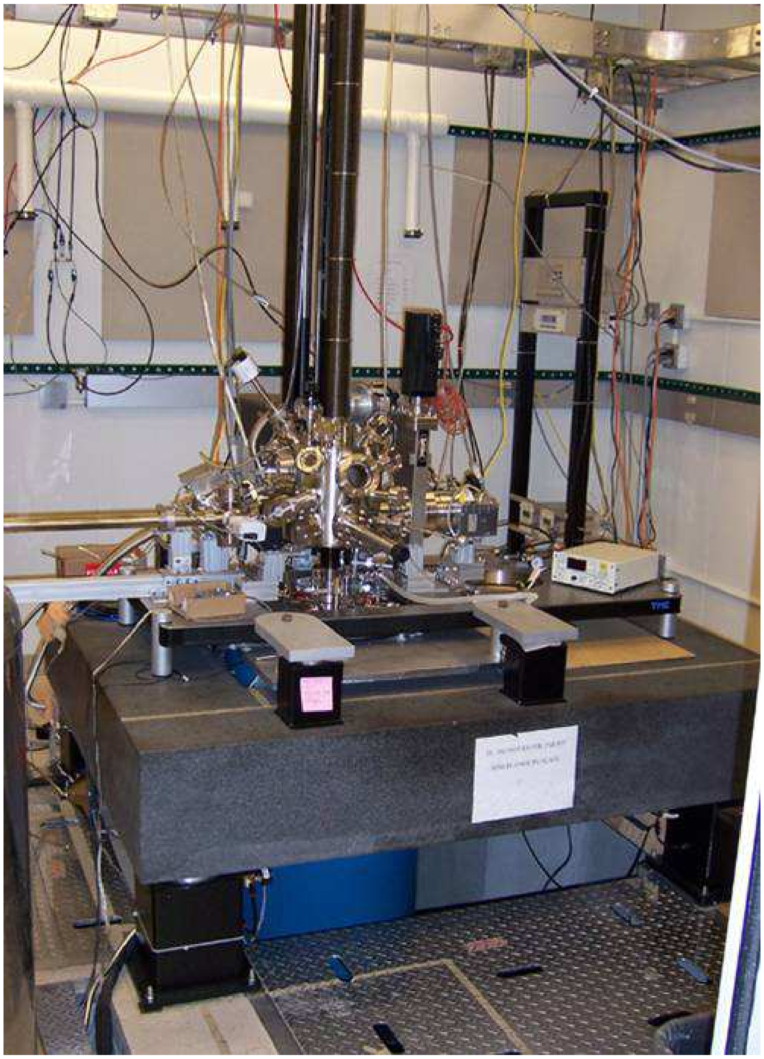

Figure 3.7: The homemade STM system at BC.

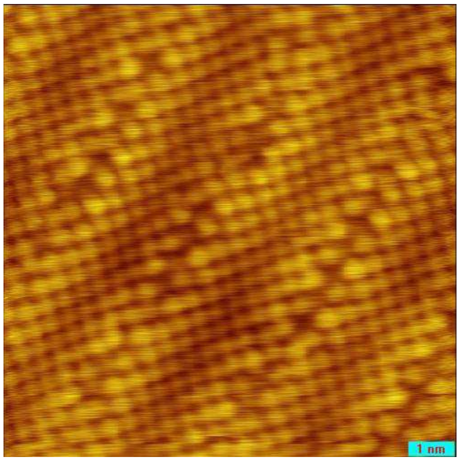

Figure 3.8: STM topographic image of optimal doped Bi2212 sample 100Å× 100Å.

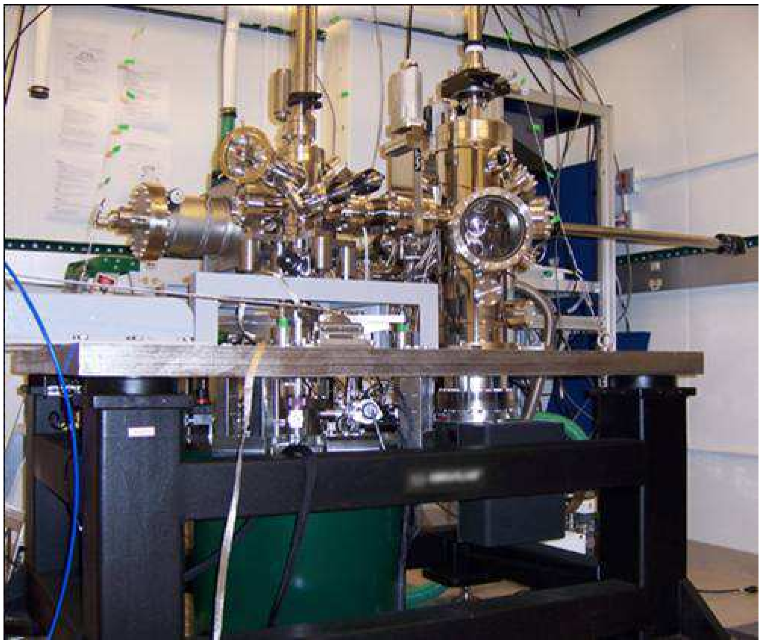

Figure 3.9: The Unisoku STM system at BC.

Figure 3.10: Photograph of a cleaved $Bi_2Sr_{2-x}La_xCuO_{6+\delta}$, glued with conducting epoxy to a copper sample holder. The samples we use are typically 1mm square.

There are a few things need to be addressed. One thing is whether the cleave causes surface re-distribution. So far, from the topographic measurements with atomic resolution we can tell the bismuth atoms remain ordered as expected. But the cleave may affect the oxygen dopant atoms which are invisible to STM right now.

Another issue is the cleave temperature. It is a easy to think that a cold cleave may be difference from the warm cleave. And because the sample will be inserted to the 4.2K environment in most of the experiments. The cooling down procedure can be damped by a warm cleave, and the cold cleave also can be good for lowing the atoms' mobility during and after the cleavage. The difficulty is the excise measurement of the cleaving temperature, we have tried the 100K and room temperature, luckily, so far we have not seen any difference of the data. It may because of the $Bi_2Sr_{2-x}La_xCuO_{6+\delta}$ is one “good” sample for STM, but this can be a really serious issue for other materials such as the new iron pnictide samples.

Last thing need to be addressed here is the following: We believe the key layer for superconductivity is the CuO layer, why are we taking the STM tip to the BiO layer? Actually there are two layers between the STM tip and CuO layer, BiO and SrO layers. We believe the BiO and SrO layers are insulating or at least semi-conducting with a large gap, so the tunneling current is going through these two layers regarding them as part of the vacuum tunneling barrier. And there is another "good" side-effect, the BiO and SrO layers actually protect the CuO layer from losing the charge carrier concentration in the CuO planes.

To summarize, we cleave the sample at UHV, and put the sample into the cold stage right away, by thinking through all the issues mentioned above, we are good to go.

3.3 Summary

In this chapter we reviewed the instrumentation of our home-made STM system in details. We also documented the sample preparation procedures and experimental environments. Start from next chapter we will go into the part of STM data analysis and discussions.

Bibliography

[1] K. Eisaki *et al*, Phys. Rev. B **69**, 064512 (2004).

[2] K. Fujita *et al*, Phys. Rev. Lett. **95**, 097006 (2005).

[3] H. Kambara *et al*, Rev. of Sci. Insturm. **78**, 073703 (2007).

[4] H. Luo, *et al*, Supercond. Sci. Technol. **21** 125024 (2008).

[5] W. Meevasana *et al*, Phys. Rev. Lett. **96**, 157003 (2006).

[6] S. H. Pan *et al*, International Patent Publication NUmber WO **93**, 19494 (1993).

[7] S. H. Pan *et al*, Rev. Sci. Instrum. **70**, 1459 (1999).

Chapter 4

Two coexisting and competing energy scales

4.1 Introduction

STM and ARPES studies have played a critical role in the observation of the pseudogap in the high T$_c$ cuprates such as Bi2212 and Bi2201. It has been observed that, in the underdoped cuprates, as the temperature is raised from T<T$_c$ the superconducting gap Δ_{sc} remains almost constant and smoothly evolves into a pseudogap across T$_c$. Above T$_c$, the pseudogap is gradually filled up and remains essentially a constant, before vanishes at the crossover temperature T* [29] [11] [17]. Figure 4.1 shows some representive STM data on Bi2212 and Bi2201 samples. The spectroscopies in red color on Bi2212 and Bi2201 panels mark the T$_c$, and the gap persists through T$_c$ while the coherence peaks start to smear out.

Right after the discovery of the pseudogap, the following question became one of the hottest issue in high T$_c$ superconductivity: What is the origin of the pseudogap and what is the relationship between the pseudogap and superconducting gap? The energy scales for both gaps are one important parameter to look at. S. Hufner *et al.* summarize the gap values from several experimental techniques [10], as shown in Figure 4.2. Most results on the pseudogap published so far are from ARPES, inelastic neutron scattering, Raman experiments and NMR. It is clear that there are two different energy scales observed from these experiments. The large body of experimental data which suggests a coexisting two-gap scenario, i.e. superconducting gap and pseudogap, over the whole superconducting dome.

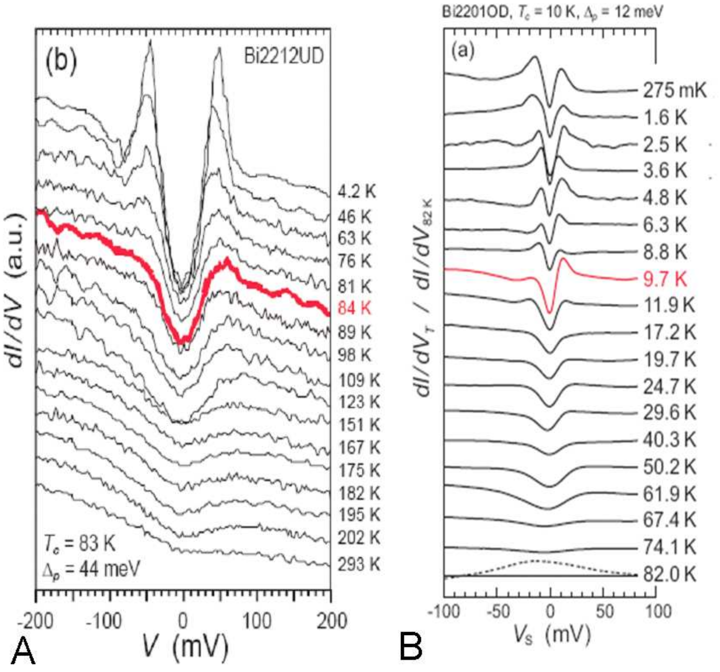

Figure 4.1: T dependencies of the DOS measured by STM. (A) Junction between an iridium tip and UD Bi2212 with T$_c$=9K,83K, Δ_{sc}=44mev, and the T* near room temperature. From Renner *et al.* 1998. [11] (B) Bi2201 From Kugler *et al.* 2001. [17]

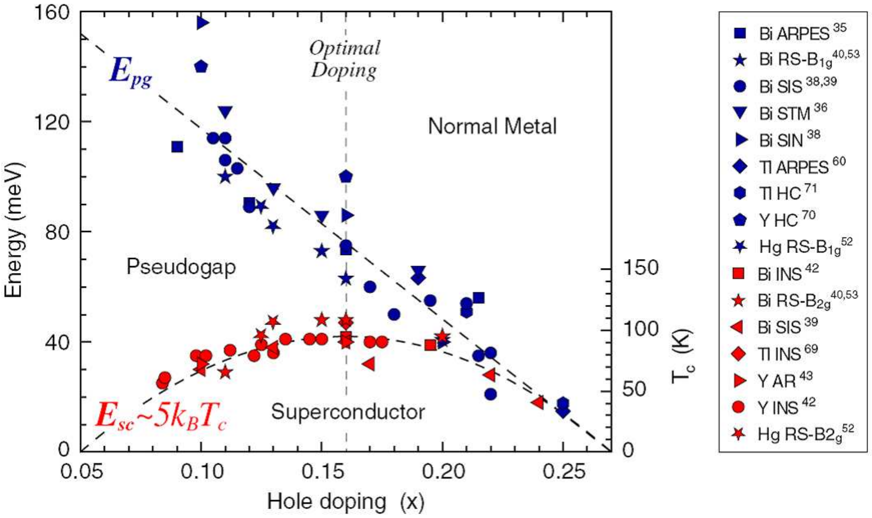

Figure 4.2: Pseudogap (E_{pg}=2Δ_{pg})and superconducting (E_{sc}~5$K_B T_c$) energy scales for a number of HTSCs with $T_c{}^{max}$~95K (Bi2212, Y123, Tl2201 and Hg1201). The datapoints were obtained, as a function of hole doping x, by ARPES, Tunneling (STM, SIN, SIS), Andreev reflection (AR), Raman scattering (RS) and heat conductivity (HC). From Hufner *et al.* 2008. [10]

Explanations for the origin of the pseudogap fall into two general categories. (1) The pseudogap is a precursor pairing state without the superconducting coherence. (2) The pseudogap is a competing phase with a hidden order parameter, for instance, CDW, SDW, etc. [5] [19]. Both of these have strong consequences for superconductivity.

Many earlier experimental results on the pseudogap demonstrated characteristics of a precursor pairing gap, including similar gap amplitudes and *d*-wave-like momentum dependence above and below T_c, and smooth temperature evolution through T_c [38], as shown in Figure 4.1. This also has led to a belief that the superconducting phase is characterized by a single *d*-wave pairing order parameter which finds support in the observation of a single *d*-wave gap function in cases where the Bogoliubov quasiparticle peak survives at the antinode [33].

Recently, there has been increasing evidence for the existence of two distinct gaps associated with different order parameters coexisting below T_c, such as opposite doping dependence for the two gaps [10] [26], and different temperature dependencies of the two gaps [33] [37] [12]. Figure 4.3 shows different doping dependence of the these two gaps. At temperature $\approx$10K above T_c, we can see there exists a gapless Fermi arc region near the node. With the increasing doping, this gapless Fermi arc elongates, as the pseudogap effect weakens. At $T<T_c$ a *d*-wave like superconducting gap begins to open near the nodal region; however, the gap profile in the antinodal region deviates from the simple *d* wave form. At the temperature well below T_c, the superconducting gap with the simple *d*-wave form eventually across entire Fermi surface in the underdoped sample with T_c=92K and the overdoped sample with T_c=86K but not in the underdoped sample with T_c=75K. Besides Bi2212, there are other samples show strong deviations from a single *d*-wave gap function such as Bi2201 [37] [11], as shown in Figure 4.4. The plot of gap versus Fermi angle shows stronger deviation from a single *d* wave form which may imply there are two coexisting gaps. Unlike the Bi2212, the Bi2201 samples has well separated energy scales between the supercondcuting gap and pseudogap which make it a good candidate for this study.

4.2 $\mathbf{Bi_2Sr_{2-x}La_xCuO_{6+\delta}}$

Among the families of the high T_c cuprates, the bismuth family is one of the most popular materials for surface probes such as STM and ARPES. Bi2212 has been studied extensively by STM due to the availability of high quality crystal, and good cleave

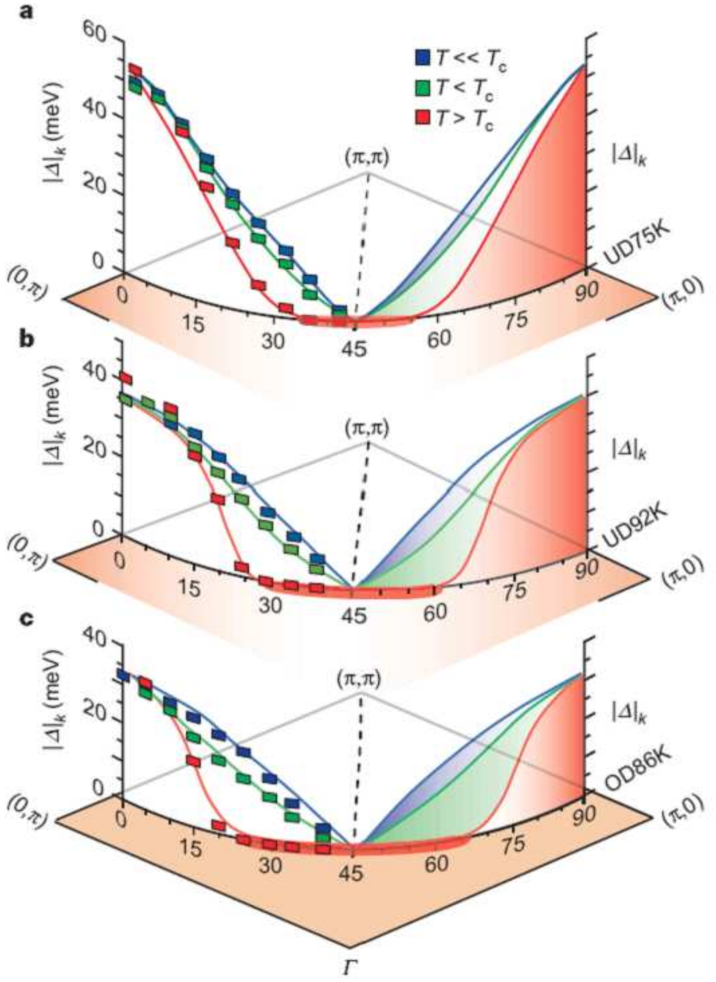

Figure 4.3: Schematic illustrations of the gap function evolution for three doping levels of Bi2212. (A) Underdoped sample with T$_c$=75K. (B) Underdoped sample with T$_c$=92K. (C) Overdoped sample with T$_c$=86K. From W. S. Lee *et al.* 2007. [12]

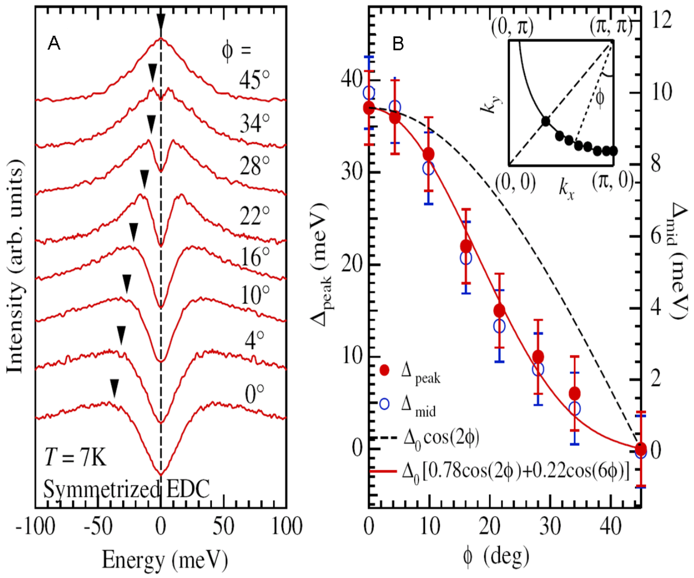

Figure 4.4: ARPES results on La-Bi2201 (A) Symmetrized EDCs show the peak gap values. (B) Plot of peak gap values versus Fermi angles. From T. Kondo *et al.* 2007. [11]

surface, which is critical to STM measurements. Many phenomena have been revealed within last 10 years on Bi2212, including spatial inhomogeneity, quasi-particle interference, vortex states, etc.

In this thesis, we study the single layer high T_c cuprate: $Bi_2Sr_{2-x}La_xCuO_{6+\delta}$ (La-Bi2201), In this section we will introduce this sample's crystalline structure, transport measurements, and sample growing methods.

4.2.1 Crystalline structure of $Bi_2Sr_{2-x}La_xCuO_{6+\delta}$

$Ln_xBi_2Sr_{2-x}CuO_{6+\delta}$ is a single layer system with the highest Tc of 36K. Figure 4.5 shows the crystal structure. The copper oxide plane is separated by SrO and BiO planes, Sr can be substituted by lanthanide (such as La, Nd, Sm, Eu, Gd) and bismuth. This substitution occurs right above the copper oxide plane which is believed to be the crucial plane to the superconductivity, so the substitution is expected to have strong effect on the electronic structure and chemical environment. Essentially, one can separate the effects of Ln-substitution into two parts: changing carrier concentration and introducing the out-of-plane disorder [7]. It is still not very clear how these effects influence superconductivity. But there is an important observation that the mismatch between the size of substituted ions introduces A-site disorders, which results in different T_c ranging from 30 to 10K at the optimal doping level in each system [6], as shown in Figure 4.6. The $La_xBi_2Sr_{2-x}CuO_{6+\delta}$ system has the weakest influence from the mismatch of the atoms' sizes and thus the highest T_c in this family, while the $Bi_{2+x}Sr_{2-x}CuO_{6+\delta}$ system represents the opposite extreme. The relationship between the disorder and T_c sheds light in the mechanism of HTSC.

4.2.2 Sample growth and transport measurements

The samples we studied in this thesis were provided by Hai-Hu Wen's group, Chinese Academy of Science in China.

$Bi_2Sr_{2-x}La_xCuO_{6+\delta}$ single crystals with high quality have been grown successfully using the traveling-solvent floating-zone technique. The patterns of X-ray diffraction indicate high crystalline quality of the samples. The crystals show sharp superconducting transitions revealed by AC susceptibility, which can be observed from the susceptibility results [6] [20] (Figure 4.7). The hole concentration p is deduced from the superconducting transition temperature, which exhibits a linear relation with La doping level x (Figure 4.8). It ranges from the heavily overdoped regime ($p \approx 0.2$) to

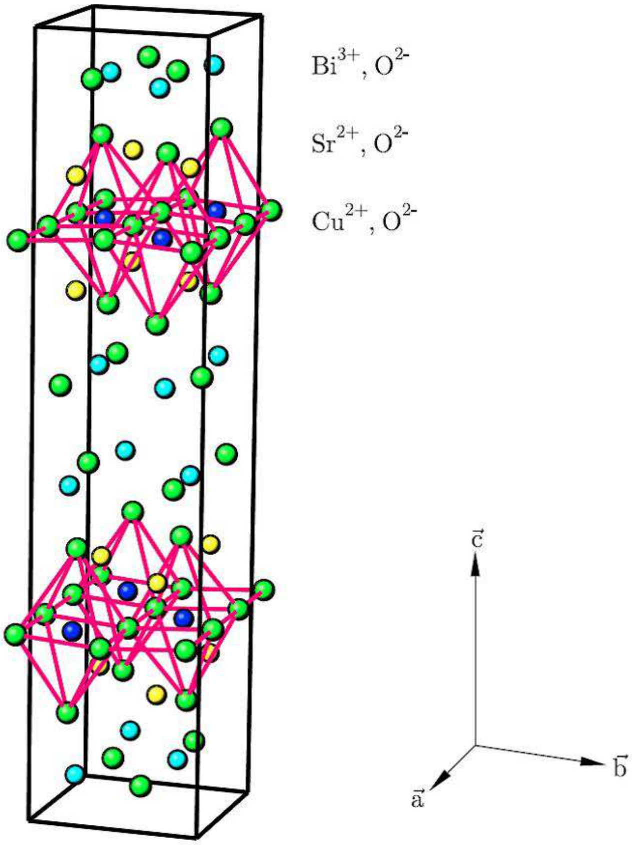

Figure 4.5: Crystalline Structure of $Ln_{0.4}Bi_2Sr_{1.6}CuO_{6+\delta}$ samples.

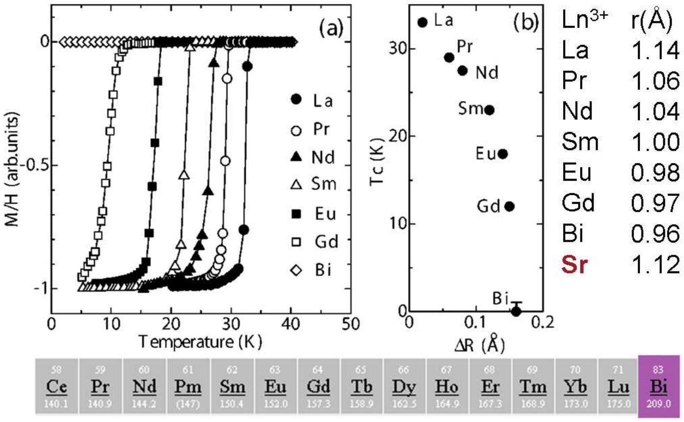

Figure 4.6: (a)$La_{0.4}Bi_2Sr_{1.6}CuO_{6+\delta}$ susceptibility curves, normalized to -1 at the lowest temperature. (b) T_c values as a function of $\triangle$R.

the extremely underdoped side ($p\approx0.08$) where the superconductivity is absent [22].

In this thesis, we focused on two dopings: nearly optimally doped $Bi_2Sr_{1.6}La_{0.4}CuO_{6+\delta}$ with a T_c of 32K (0.4La) and overdoped $Bi_2Sr_{1.9}La_{0.1}CuO_{6+\delta}$ with a T_c of 18K (0.1La).

4.2.3 $Bi_2Sr_{2-x}La_xCuO_{6+\delta}$ for STM study

Recently $La_xBi_2Sr_{2-x}CuO_{6+\delta}$ has attracted a lot of interest from STM groups all over the world along with other experimental techniques. In earlier text we put a few sentences on why we choose $La_xBi_2Sr_{2-x}CuO_{6+\delta}$ for our study. Here we summarize the reasons in detail:

(1) The single layer sample has lower T_c, so it is easier to probe the normal state.

(2) $Ln_xBi_2Sr_{2-x}CuO_{6+\delta}$ can be substituted with different elements and has different behavior, this can expand our study from doping dependence to dopant dependence and enrich our understanding of the physics.

(3) $La_xBi_2Sr_{2-x}CuO_{6+\delta}$ can cover a wide doping range from heavily underdoped region to heavily overdoped region.

(4) $La_xBi_2Sr_{2-x}CuO_{6+\delta}$ has the well separated energy scales for superconducting gap and pseudogaps.

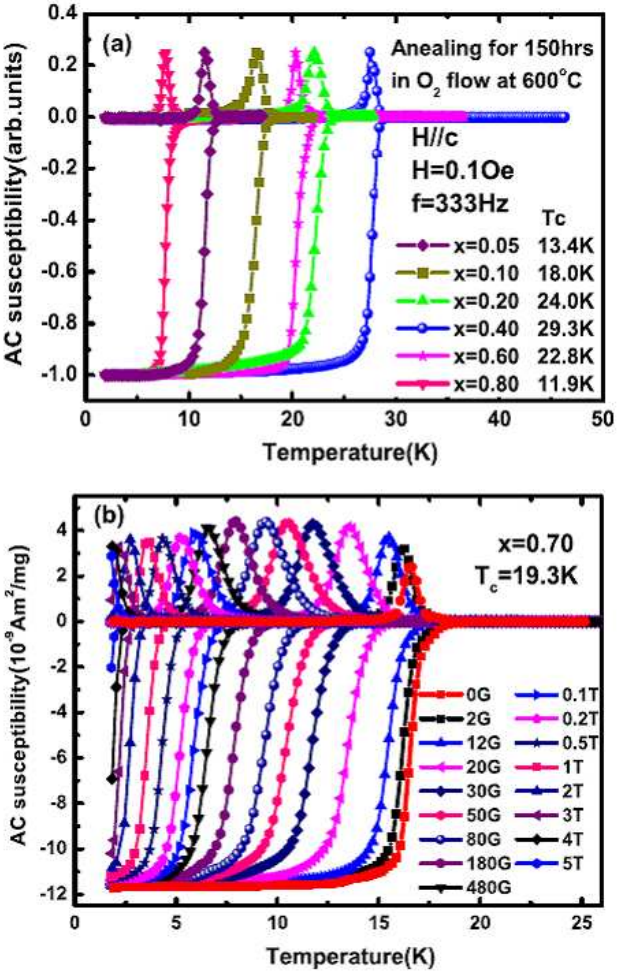

Figure 4.7: (a) The normalized AC susceptibility for the annealed single crystals with x=0.05,0.10,0.20,0.40,0.60 and 0.80. The T$_c$ was defined as the point where the real part deviates from the flattened normal state part. (b) The typical AC susceptibilities under different external DC fields, which show the easy suppression of superconductivity under low DC fields. From H. Luo *et al.* 2008. [20]

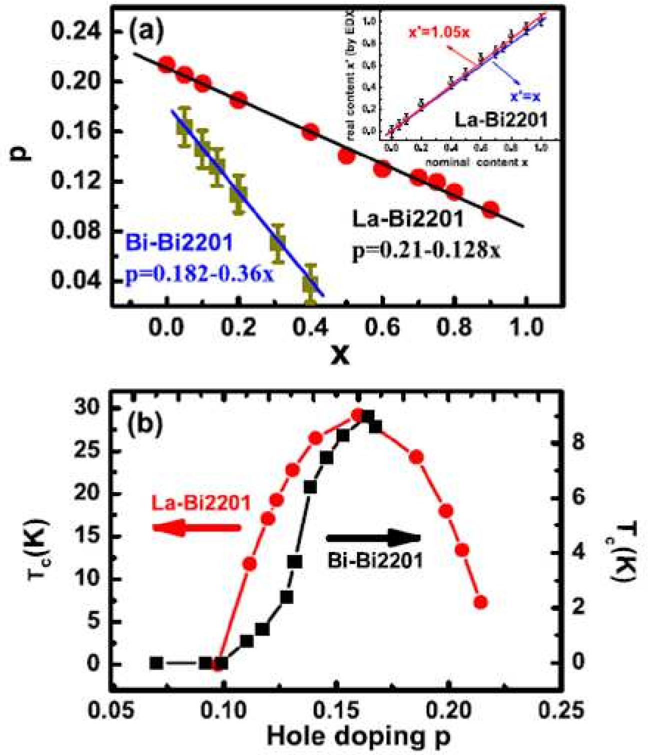

Figure 4.8: (a) The linear relation between hole concentration p and Ln doping level x. The solid lines are linear fitting for the scattering points. Inset: the real content doping of La for La-Bi2201, which is determined by DEX measurements. The crystal composition is very close to the starting material, where the segregation coefficient $K=C_s/C_i$ is only about 1.05, slightly above 1. (b) The superconducting dome for Bi and La doped Bi2201, where the hole concentration is deduced from the linear formulas in (a). It can be seen that the 'bell shape' is distorted in Bi-Bi2201. From H. Luo *et al.* 2008. [20]

4.3 Observation of two coexisting gaps

4.3.1 Bimodal gap distribution

Right after we approach the STM tip to a fresh cleaved sample, the first STM data we take is a topographic image. $Bi_2Sr_{2-x}La_xCuO_{6+\delta}$ has a well known surface and lattice constant. Once we obtain a surface with good atomic resolution then we can proceed with the confidence of having a good sample. (Figure 4.9 and Figure 4.10)

Typical linecuts of spectral data on 0.4La and 0.1La samples are shown in Figure 4.11 and Figure 4.12 respectively. which covers a 100Å distance. From the spectra shown in Figure 4.11 and Figure 4.12, we observe two distinct gaps coexisting at a given spatial location. Figure 4.13 shows how we define these two gaps. It is worth while mentioning that this is the first time coexistence of two energy scales clearly visible in a single STM spectrum.

Figure 4.14 shows the gap histograms based on the gap values. Both samples show a clear bimodal gap distribution histogram. For 0.4La sample, the small gap averages at 10.50meV and has a standard deviation of 2.8meV and the large gap has an average of 27.2meV and standard deviation of 5.4meV. For 0.1La sample, the small gap averages at 7.40meV and has a standard deviation of 1.6meV, the large gap averages at 20.7meV and has a standard deviation of 3.9meV. We also did the same gap analysis on dI/dV maps to extract the small and big gap maps, the results will be presented in later text. We emphasize that the average gap values and their standard deviations taken from the maps are consistent with the number taken from the linecuts.

One thing needs to be addressed is that the second gap or large gap of 0.1La is not visible for every single spectroscopy, the reason will be discussed in next chapter. For the moment we just include every single spectroscopy which shows a clear second gap for the histogram.

When we consider earlier data from other group we see that there are small gaps that have been neglected, as shown in Figure 4.15 [35]. A. Sugimoto *et al.* performed STM experiments on the same sample with a slightly different doping level. Their data did have the coexistence of two energy scales, but these small features were not defined as a gap. Instead the large gaps were counted as the only gap associated with the superconductivity. The red arrows show the small gaps which were neglected. Therefore the corresponding histogram of gap distribution only has one peak instead of our two. Attributing the large gap as the superconducting gap also cause some

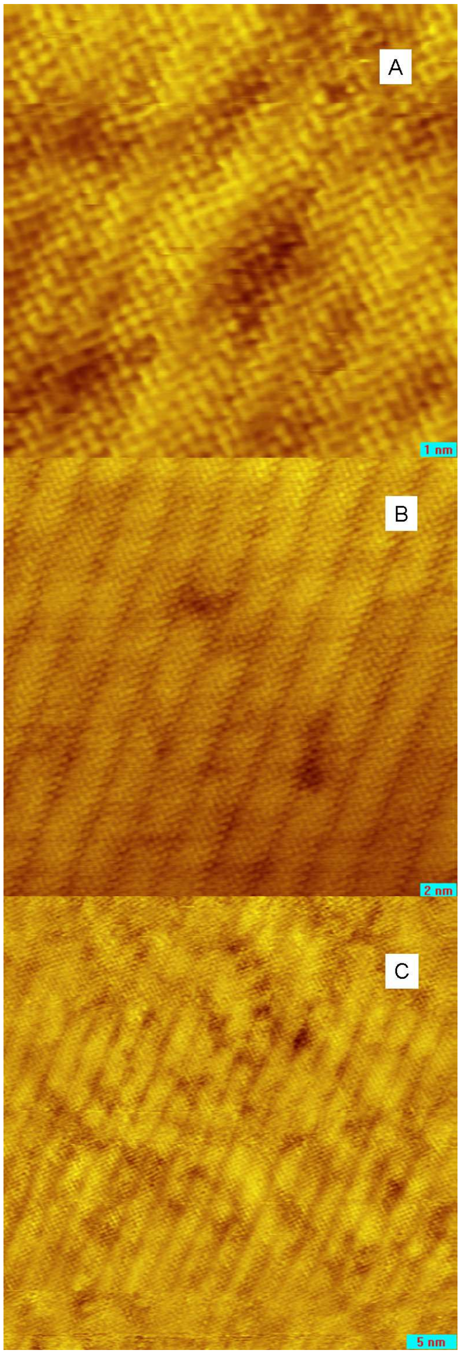

Figure 4.9: (A) STM topographic image of 0.4La at 4.2K 128 Å× 128 Å. (B) 256 Å× 256 Å. (C) 451 Å× 451 Å.

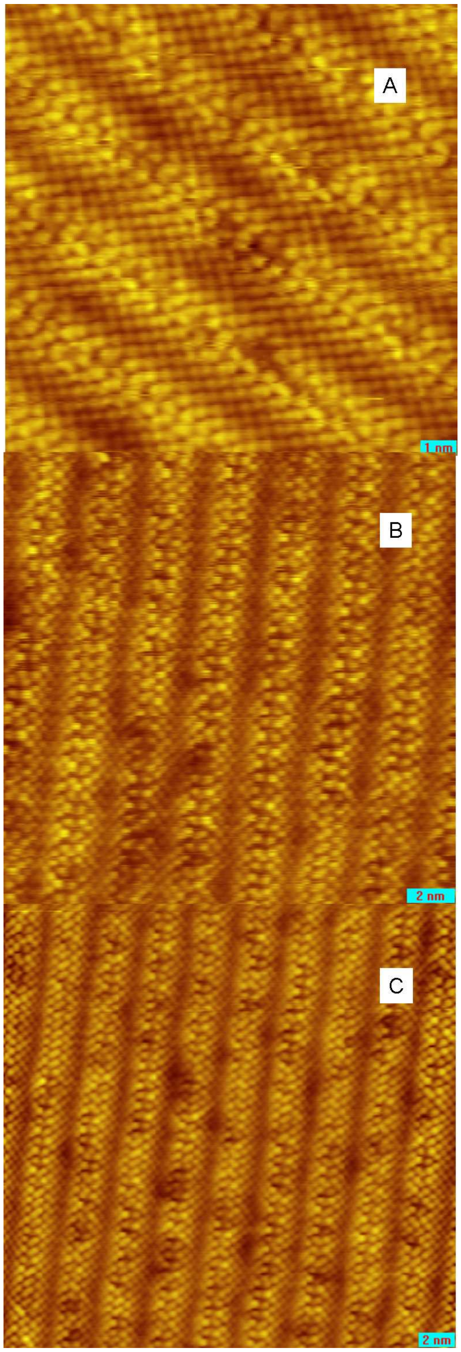

Figure 4.10: (A) STM topographic image of 0.1La at 4.2K 128 Å× 128 Å. (B) 192 Å× 192 Å. (C) 256 Å× 256 Å.

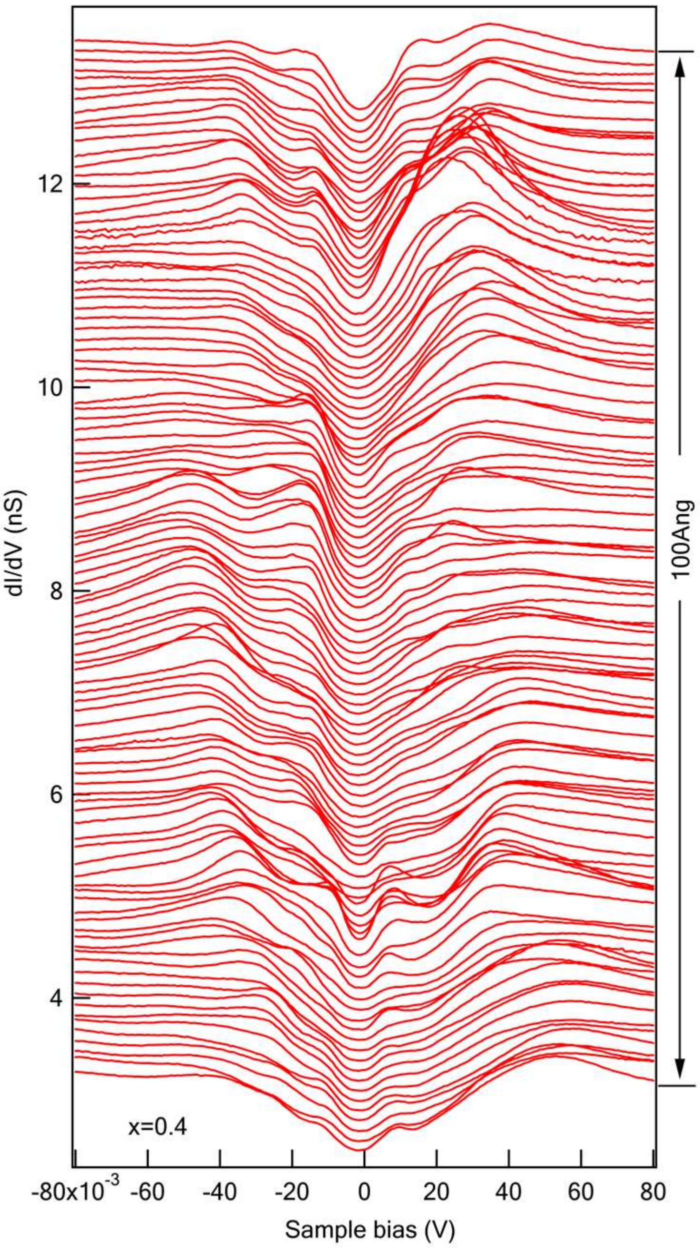

Figure 4.11: STM linecut spectrum taken on 0.4La sample 100Å distance.

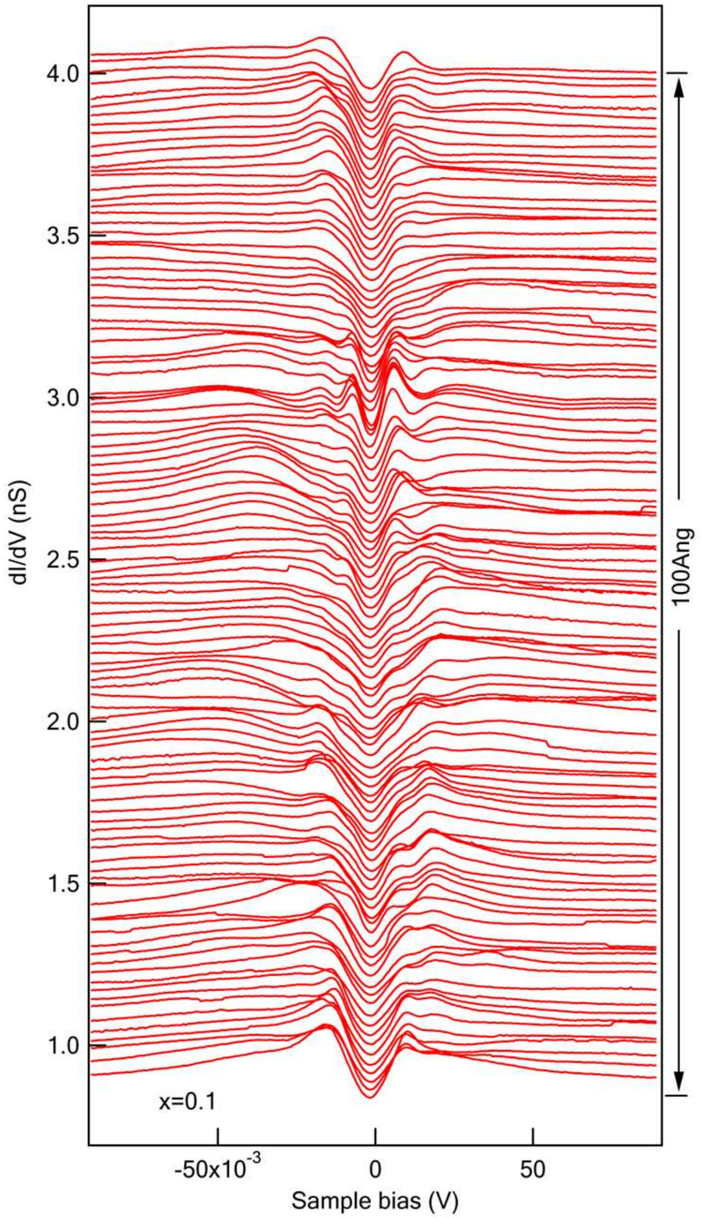

Figure 4.12: STM linecut spectrum taken on 0.1La sample 100Å distance.

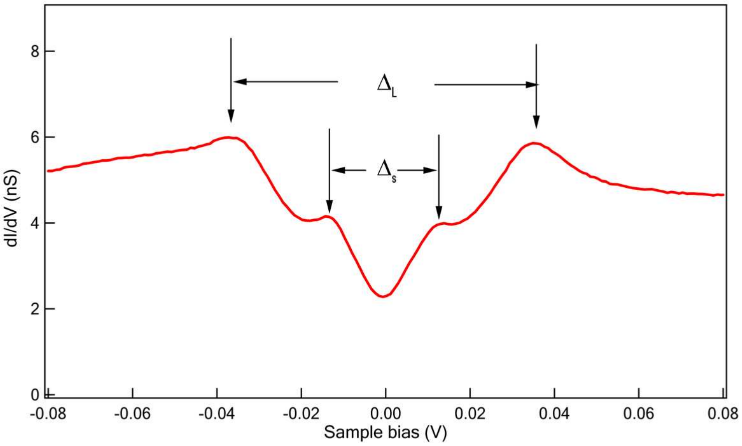

Figure 4.13: A single STM spectroscopy taken on 0.4La sample.

confusion since it exaggerated the value of the SC gap, resulting in a ratio of $2\Delta/K_BT_c$ as large as 20-30.

Based on our data, the $2\Delta/K_BT_c$ for small gap of 0.4La sample is 7.6, the $2\Delta/K_BT_c$ for small gap of 0.1La sample is 9.5. These numbers are close to the usual number of the superconducting gap value of high T_c cuprates. The $2\Delta/K_BT_c$ for large gap of 0.4La sample is 19.7 while the $2\Delta/K_BT_c$ for large gap of 0.1La sample is 26.7 which are too large to be associated with superconductivity.

4.3.2 Comparison between STM and ARPES data

From the data shown above, we know there is clear bimodal distribution of gap values from STM results. The $2\Delta/K_BT_c$ ratio for the small gap indicates that it may be the gap associated with superconductivity. Trying to identify the small gap with more convincing evidence, we obtained ARPES data on the same samples. (Figure 4.16). ARPES experiments were performed by ARPES group at BC at the Synchrotron Radiation Center in Wisconsin, and at the Tohuku University ARPES lab using a microwave-driven Xenon source ($h\nu$=8.437eV) with very high resolution (E_{Re}<4meV, k_{Re}<0.005Å^{-1}). Comparing the ARPES energy distribution curve (EDC) data along with our STM spectroscopy results, we find out that the average STM small gap is comparable to the ARPES gap at the arc tip (∼11mev). (Figure 4.17) And the small gaps observed by ARPES follows the *d* wave fitting when we plot the Δ against the Fermi angle. (Figure 4.18) Here two questions appear: (1) Is there any counterpart

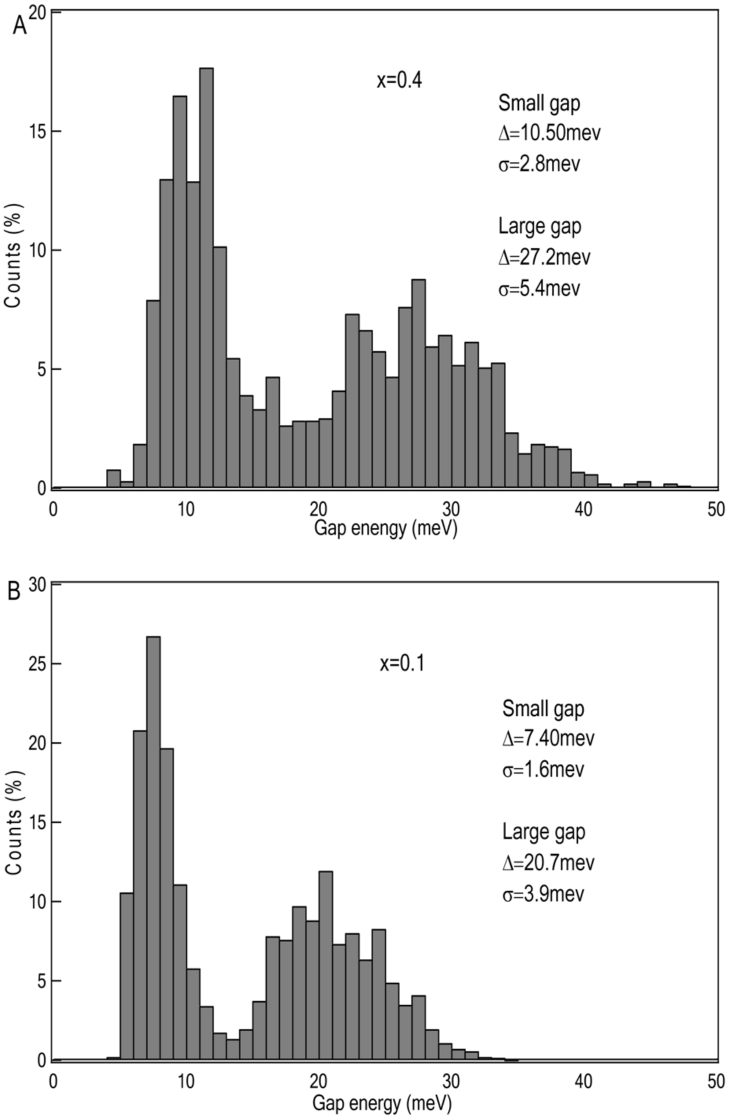

Figure 4.14: Bimodal gap histogram for (A) 0.4La sample, the small gap averages at 10.50meV and has a standard deviation of 2.8meV and the large gap has an average of 27.2meV and standard deviation of 5.4meV. (B) 0.1La sample, the small gap averages at 7.40meV and has a standard deviation of 1.6meV, the large gap averages at 20.7meV and has a standard deviation of 3.9meV.

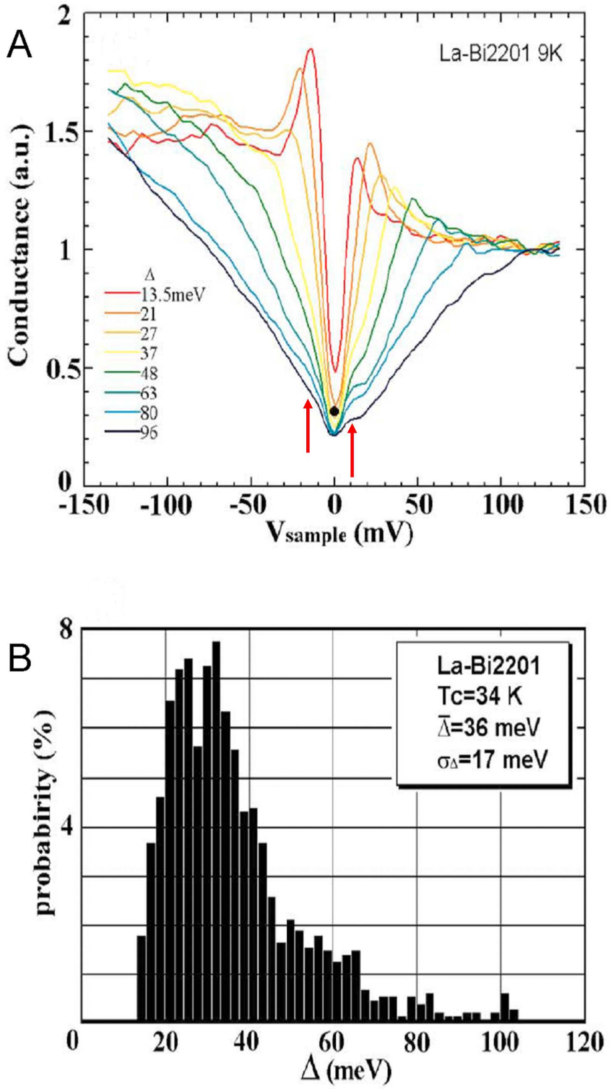

Figure 4.15: STM spectrum of optimal doped La-Bi2201 samples published by A. Sugimoto *et al.* (A) The averaged STM spectrum based on the gap values on optimal doped La-Bi2201 sample T$_c$=34K measuring temperature is 9K. Red arrows show the small gaps neglected. (B) the corresponding gap histogram.

of the large gap observed in STM spectrum in ARPES EDCs? (2) Earlier ARPES experiments on similar samples found a large antinodal gap of about 35meV both above and below T$_c$ without seeing the small gaps. How do we reconcile the two observations?

Our low photon energy, high resolution ARPES enhances the features of the coherent excitations such that even data near the antinodal region reveal smaller gaps which follow the d-wave fit reasonably well. This indicates a superconducting gap persisting to the antinodals. The observed "pairing beyond the Fermi Arc" can be explained by the fact that the large pseudogap near the antinodes. is a soft gap with suppressed but finite in-gap density of states that could facilitate pairing below T$_c$. In our data, we believe the reason why we don't see clear large gap near the antinode is the spectral weight associated with the superconducting coherence masks the signal from the large gap.

Further support for this idea comes from the temperature dependence of ARPES data. The large gap is clearly visible at the antinodal positions when we raise the temperature across T$_c$, as shown in Figure 4.19. For both 0.4La and 0.1La samples, the temperature dependent data show that while the small gap disappears above T$_c$, a large gap remains until the temperature reaches T*.

Figure 4.20 summarizes our findings regarding the gap values extracted from both ARPES and STM data on the two samples with different doping levels. Because STM is a probe sensitive to antinodal signals, we put the extracted values from STM at the antinodal positions. When T<T$_c$ we observe the two coexisting and competing energy scales at both real space and antinodal positions of momentum space. When T>T$_c$ the small gap disappears while the large gap survives.

4.3.3 Small gap and superconductivity

Here we summarize the evidence that allows us to associate the small gap with superconductivity.

(1) The temperature dependence data from STM experiments shows the small gap feature disappears and the large gap persists above the transition temperature (T$_c$). Figure 4.21 shows the linecut spectrum taken on 0.4La sample at 50K. The temperature dependence data from ARPES measurements are also consistent with this scenario, as shown in Figure 4.19.

(2) The gap value extracted from ARPES EDC data satisfy the d-wave gap function, as shown in Figure 4.18.

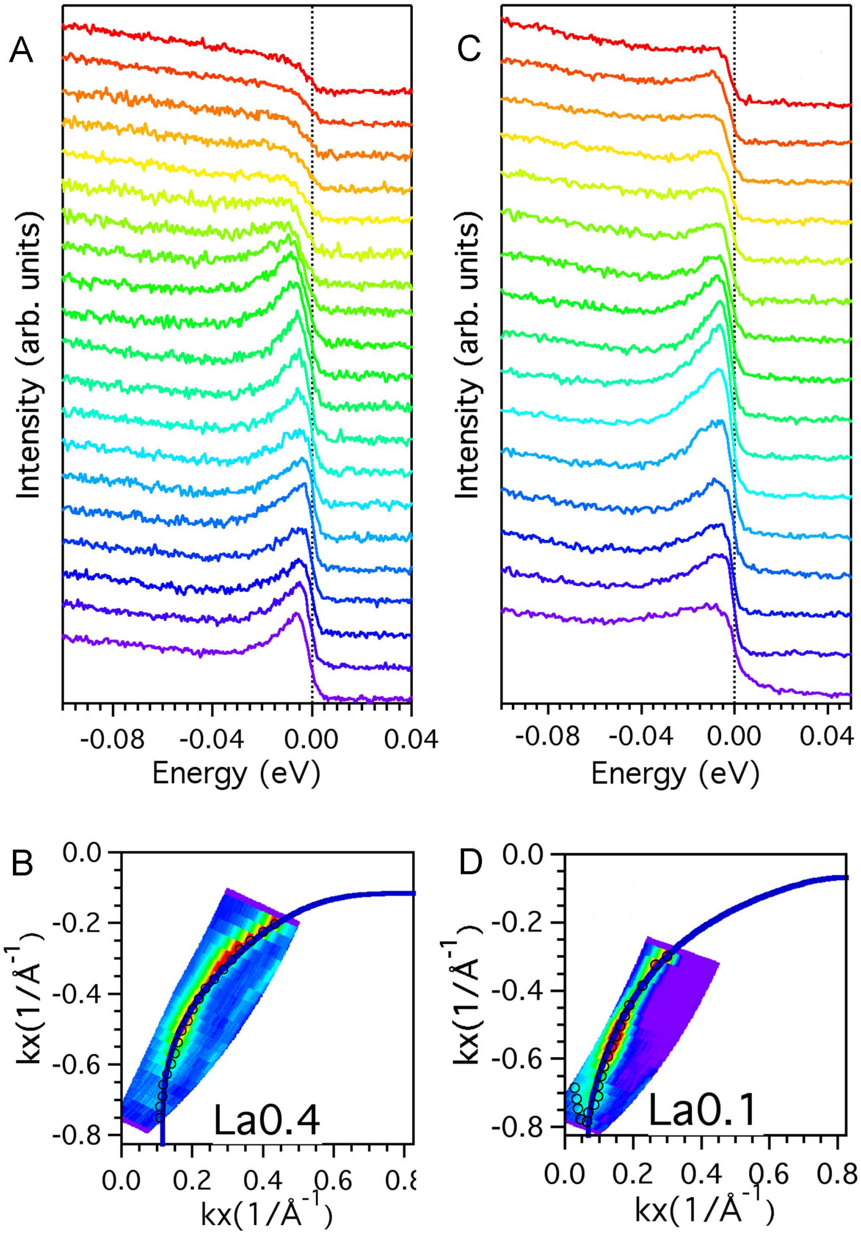

Figure 4.16: (A) and (B) Fermi surface mapping and EDCs along the Fermi surface of 0.4La sample at 5K. (C) and (D) Fermi surface mapping and EDCs along the Fermi Surface of 0.1La sample at 5K.

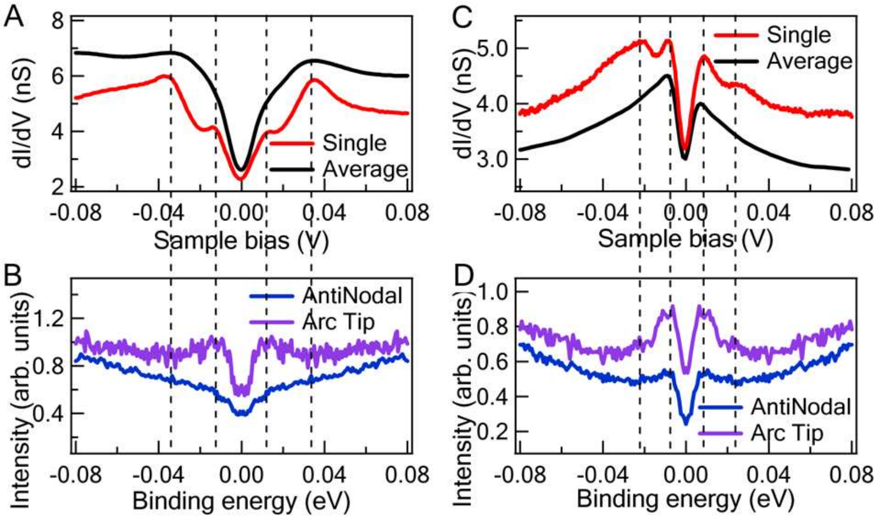

Figure 4.17: (A) Single STM spectrum (red) representative of the average Δ_s and Δ_L and spatially averaged STM spectrum (black) from a 240 $\mathring{A}$ dI/dV map (B) Symmetrized ARPES energy distribution curves (EDCs) taken at the antinodal position and at the arc tip (θ∼21°) (C) and (D) Similar data as (A) and (B), arc tip θ∼18°.

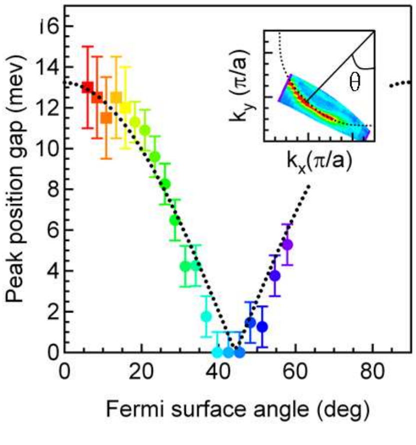

Figure 4.18: k-dependent gap value versus Fermi surface angle (defined in the inset) for data shown in Figure 4.16 (A) 0.4La.

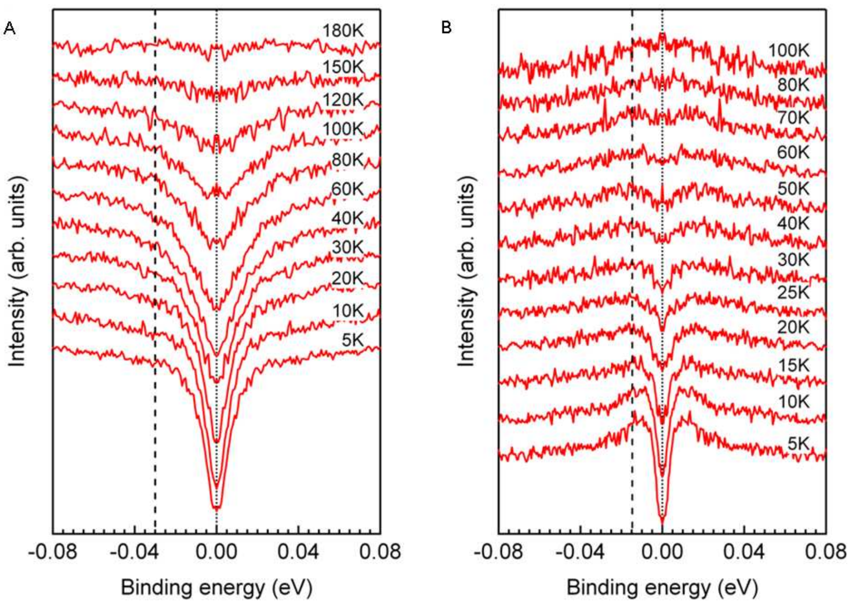

Figure 4.19: T-dependent EDC at antinodal positions for (A) 0.4La T_c=32K. (B) 0.1La T_c=18K.

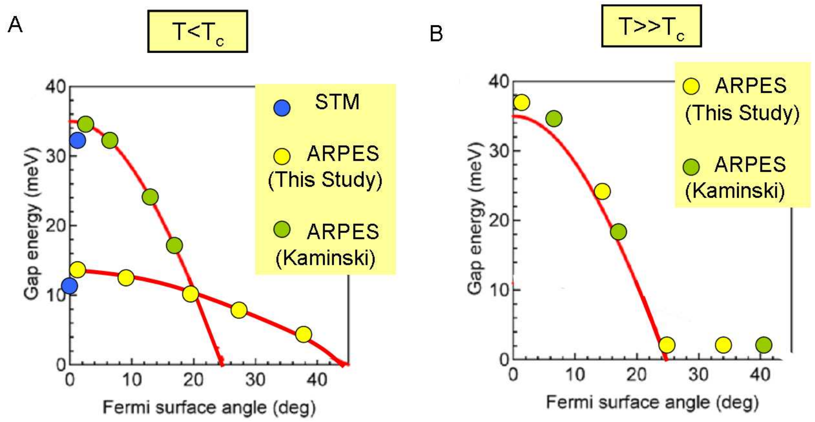

Figure 4.20: Gap values extracted from STM and ARPES results on 0.4La sample when (A) $T<T_c$. and (B) $T \gg T_c$.

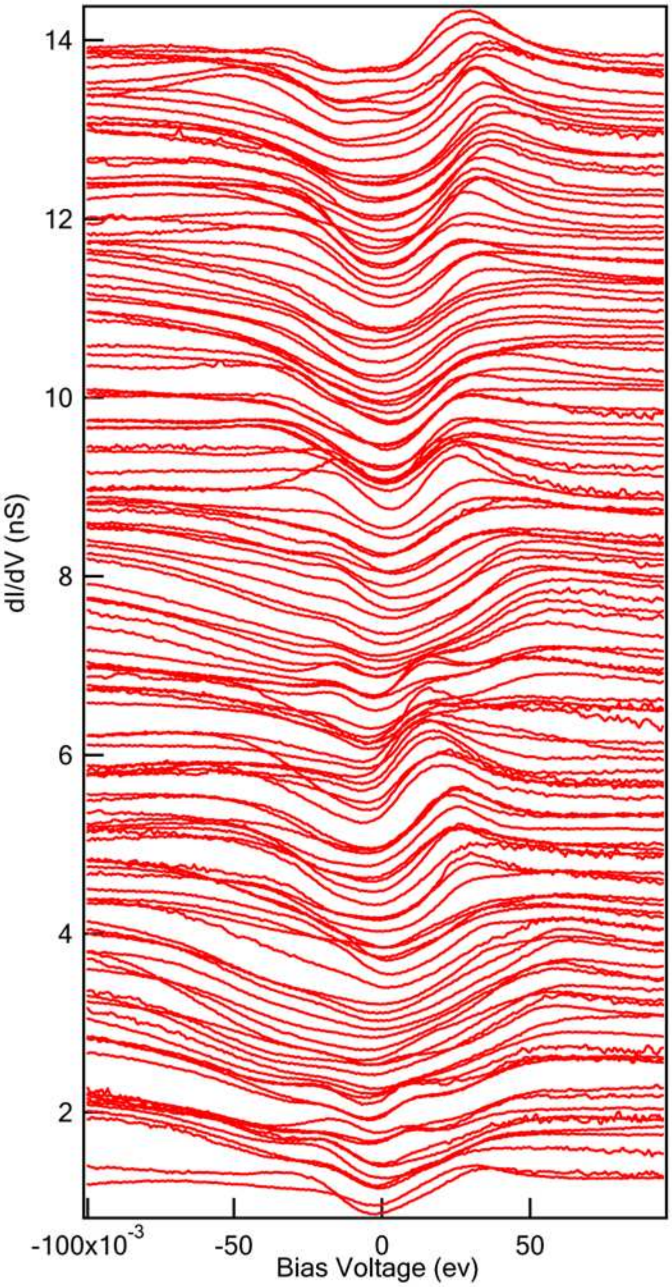

Figure 4.21: Linecut spectrum taken on 0.4La sample at 50K.

(3) The $2\Delta/\mathrm{K}_B\mathrm{T}_c$ calculated based on the small gap value for 0.4La sample equals to 7.6. For 0.1La sample, the ratio is 9.5 These numbers are consistent with other optimal doped high T_c cuprates.

Therefore we claim the small gap associated with the superconductivity. For the large gap, becaue in ARPES data we find these gaps survive above T_c, it can be considered as "Pseudogap". The detailed discussion on the pseudogap will be presented in next chapter. But one thing we will try here is when we replaced the T_c by T^* in the calculation of The $2\Delta/\mathrm{K}_B\mathrm{T}_c$. The new $2\Delta/\mathrm{K}_B\mathrm{T}^*$ for large gap of 0.4La sample is 4.2 while the $2\Delta/\mathrm{K}_B\mathrm{T}^*$ for large gap of 0.1La sample is 6.0. The number of T^* comes from the ARPES experiments, the T^* of 0.4La sample is around 140K and 0.1La sample is around 80K. These ratios make more sense.

4.4 Strong correlation

Another important observation is that there is a strong correlation between these small and large gaps observed in STM experiments. Figure 4.22 shows STM spectra on 0.4La samples that were sorted and averaged based on Δ_L. One can clearly see that as the large gap increases, so does the magnitude of the small gap. This is confirmed when we consider the *dI/dV* maps. Figure 4.23 shows the gap map based on a 256Å *dI/dV* map on 0.4La and Figure 4.24 shows the gap map based on a 128Å *dI/dV* map on 0.1La.

The cross correlation (Figure 4.25) between the two gaps gives a rather strong correlation on-site coefficient of 0.6 indicating both order parameters are influenced by the same underlying physical processes. A key point to note here is that while the second larger gap in the 0.1La samples is rather weak and not always observed, wherever it is visible it shows the same correlation with the superconducting gap as the 0.4La samples. This strong correlation is also true statistically by doing the scatter plot, as shown in Figure 4.26. Furthermore, the seamless continuation of the scatter plot for the 0.1La samples with the 0.4La samples suggests that the gap variations for both gaps may arise from doping inhomogeneities [27] [29] [44].

Recently L. Niestemski and Z. Wang proposed a VBG scenario for the coexistence of superconducting gap and pseudogap [26]. The low-energy fluctuations of the valence bond due to the superexchange are pinned by the electronic disorder from off-stoichiometric dopants, leading to a valence bond glass (VBG) pseudogap phase in underdoped high T_c Cuprates. The antinodal Fermi surface sections are gapped

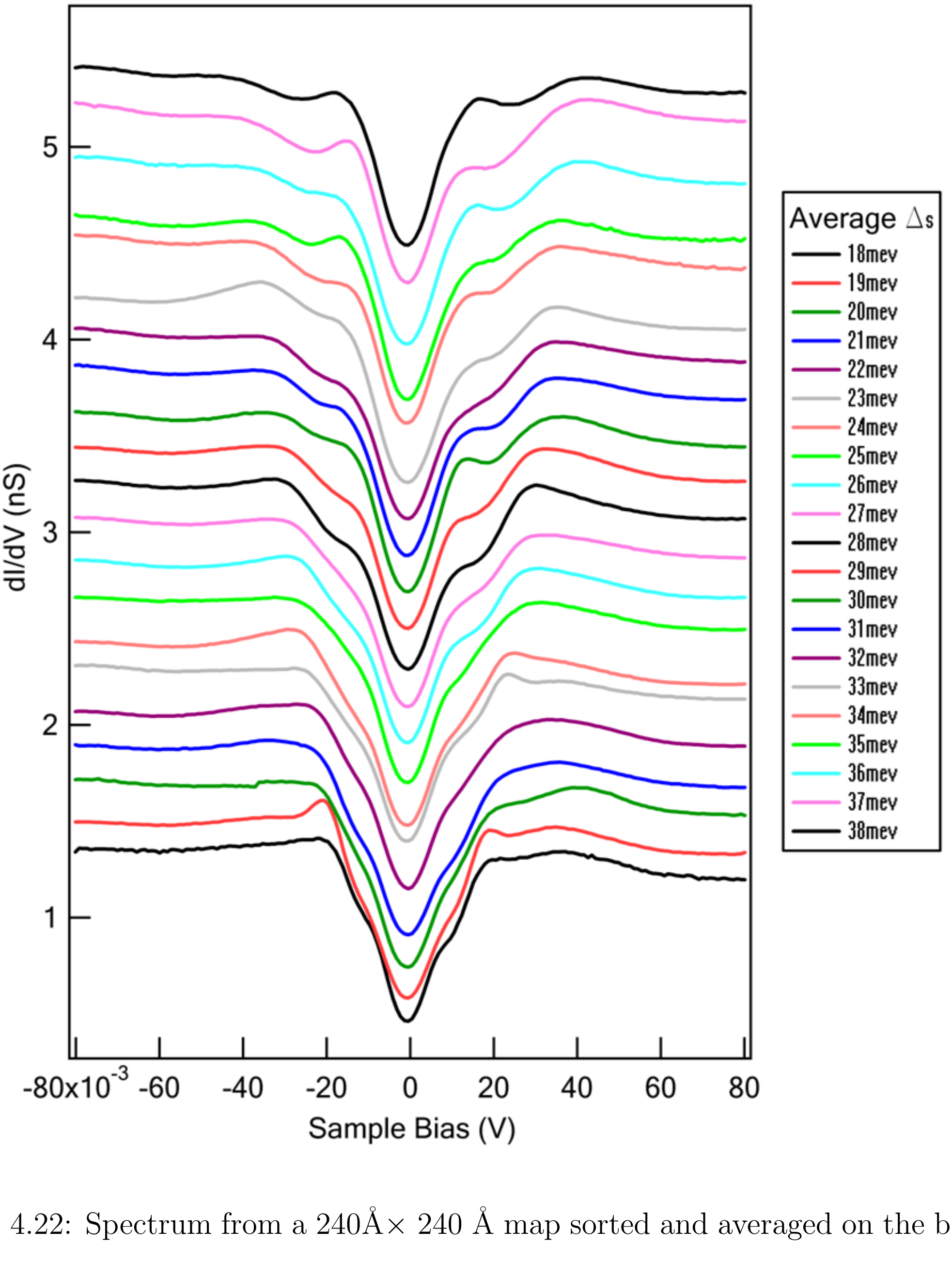

Figure 4.22: Spectrum from a 240Å× 240 Å map sorted and averaged on the basis of Δ_L.

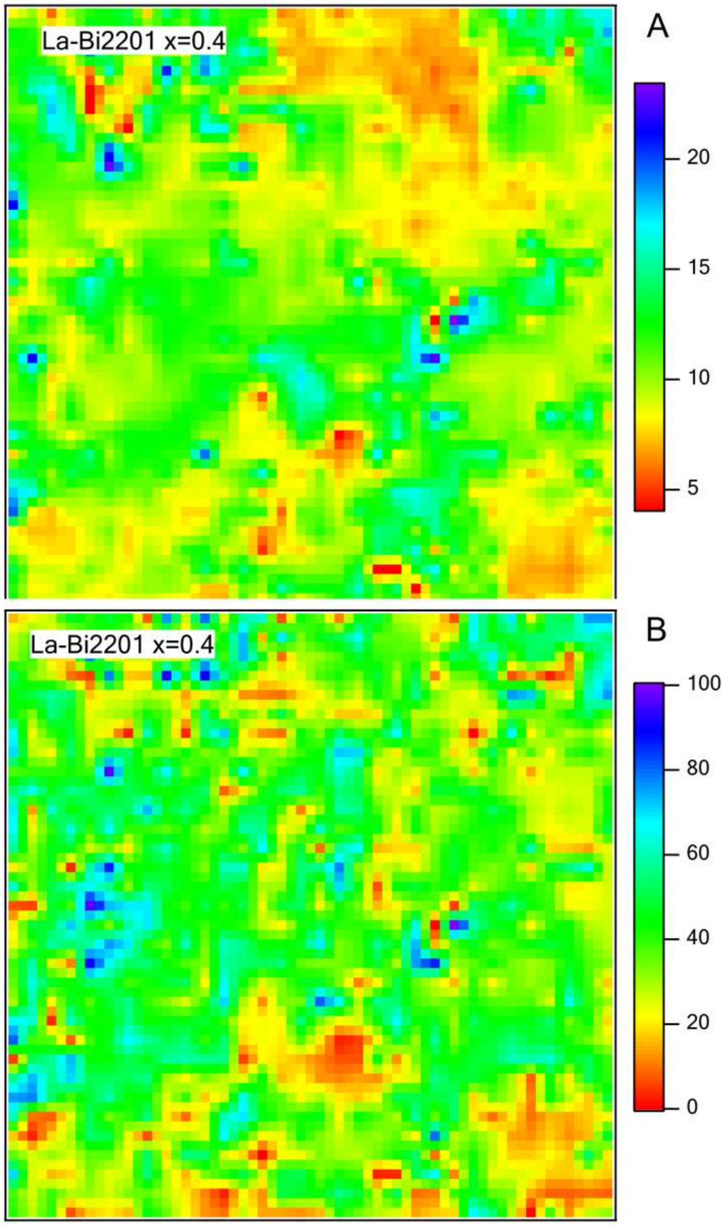

Figure 4.23: (A) Small gap map and (B) Large gap map on 0.4La sample. (256Å × 256Å).

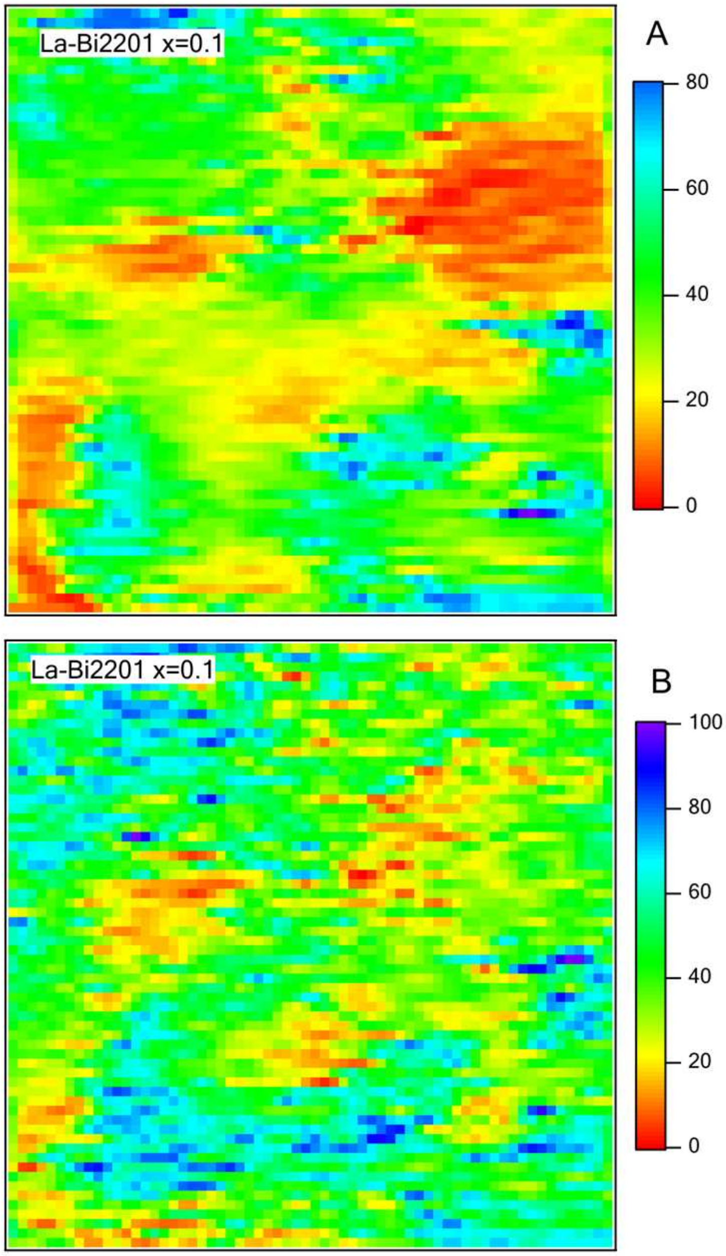

Figure 4.24: (A) Small gap map and (B) Large gap map on 0.1La sample. (128Å × 128Å).

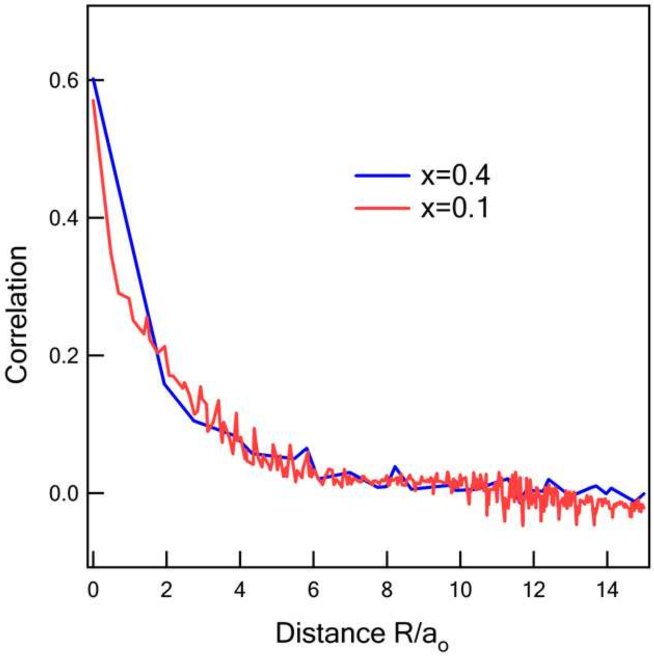

Figure 4.25: The spatial dependence of cross correlation between the Δ_s and Δ_L maps which retains a finite value up to a few lattice constants.

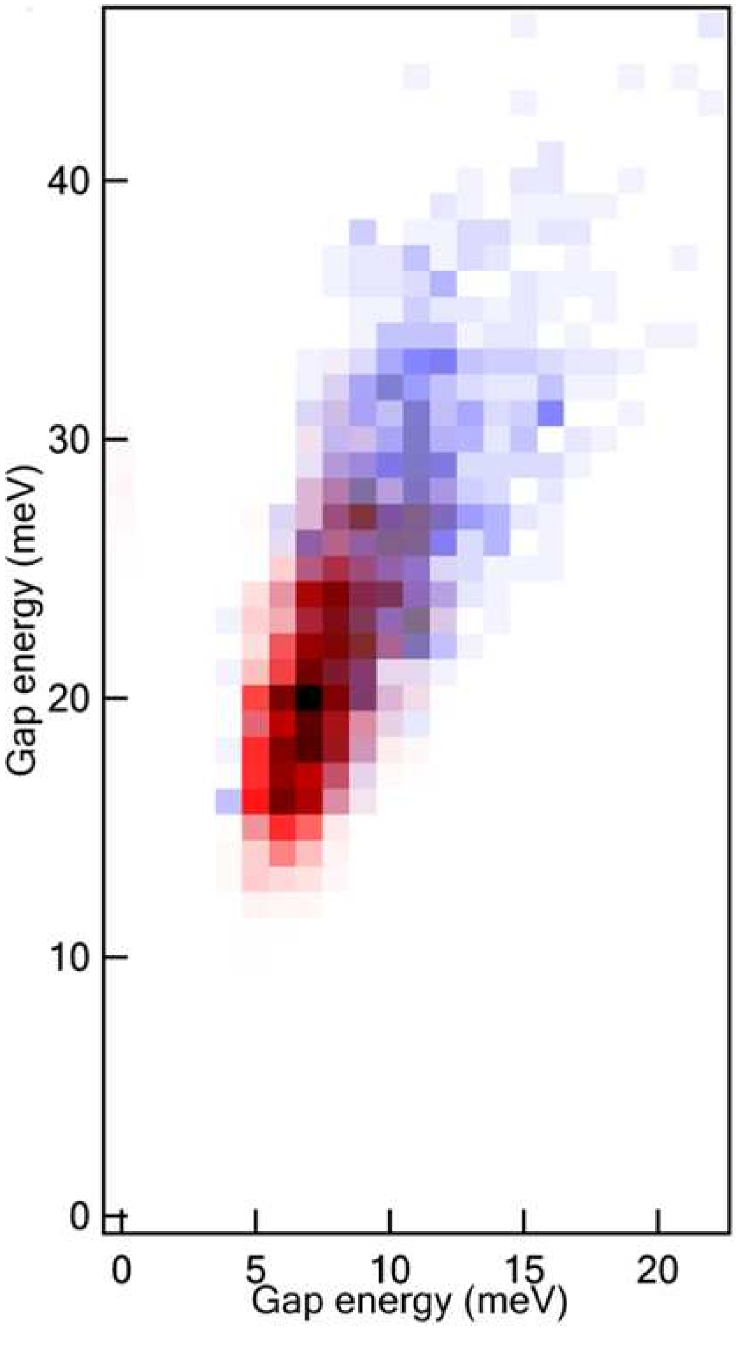

Figure 4.26: Scattering plot of occurrences of Δ_L and Δ_s

out, giving rise to a normal state Fermi arc whose length shrinks with underdoping. Below T$_c$, the superexchange interaction induces a *d*-wave superconducting gap that coexists with the VBG pseudogap. This might be one possible explanation for the same underlying physical processes we proposed above.

4.5 Summary

To summarize, through a combined scanning tunneling microscopy and angle-resolved photoemission spectroscopy study, we report the observation of two distinct gaps (a small and a large gap) that coexist both in real space and in the antinodal region of momentum space, below the superconducting transition temperature of $\mathrm{Bi_2Sr_{2-x}La_xCuO_{6+\delta}}$. We show that the small gap is associated with superconductivity. The large gap persists above transition temperature and can be considered pseudogap. We also find a strong correlation between the large and small gaps suggesting that they are affected by similar physical processes.

Bibliography

[1] B. M. Anderson *et al*, Phys. Rev. B **76**, 020507(R) (2007).

[2] M. C. Boyer *et al*, Nature Physics **3**, 802 (2007).

[3] M. Civelli *et al*, Phys. Rev. Lett. **100**, 046402 (2008).

[4] T. Das *et al*, Phys. Rev. B. **77**, 134516 (2008).

[5] H. Ding *et al*, Nature **382**, 51 (1996).

[6] K. Eisaki *et al*, Phys. Rev. B **69**, 064512 (2004).

[7] K. Fujita *et al*, Phys. Rev. Lett. **95**, 097006 (2005).

[8] G. Gruner *et al*, Phys. Rep. **119**, 117 (1985).

[9] T. Hanaguri *et al*, Nature **430**, 1001 (2004).

[10] T. Hanaguri *et al*, Nature Physics **3**, 865 (2007).

[11] J. Hoffman *et al*, Science **295**, 466 (2002).

[12] S. Hufner *et al*, Rep. Prog. Phys. **71**, 062501 (2008).

[13] H. Kambara *et al*, Rev. of Sci. Insturm. **78**, 073703 (2007).

[14] Y. Kohsaka *et al*, Science **315**, 1380 (2007).

[15] T. Kondo *et al*, Nature **457**, 296 (2009)

[16] T. Kondo *et al*, Phys. Rev. Lett. **98**, 267004 (2007).

[17] M. Kugler *et al*, Phys. Rev. Lett. **86**, 4911 (2001).

[18] W. S. Lee *et al*, Nature **450**, 81 (2007).

[19] A. G. Loeser *et al*, Science **273**, 325 (1996).

[20] H. Luo, *et al*, Supercond. Sci. Technol. **21** 125024 (2008).

[21] T. Machida *et al*, Journal of the Physical Society of Japan **75, 8**, 083708 (2006).

[22] W. Meevasana *et al*, Phys. Rev. Lett. **96**, 157003 (2006).

[23] K. McElory *et al*, Nature **422**, 592 (2003).

[24] A. J. Millis *et al*, Science. **314**, 1888 (2006).

[25] F. Niestemski *et al*, Nature **450**, 1058 (2007).

[26] L. Niestemski *et al*, Phys. Rev. Lett. **102**, 107001 (2009).

[27] S. H. Pan *et al*, Nature **413**, 282 (2001).

[28] S. H. Pan *et al*, International Patent Publication NUmber WO **93**, 19494 (1993).

[29] S. H. Pan *et al*, Appl. Phys. Lett. **73**, 2992 (1998).

[30] S. H. Pan *et al*, Rev. Sci. Instrum. **70**, 1459 (1999).

[31] C. Renner *et al*, Phys. Rev. Lett. **80**, 149 (1998).

[32] P. Romano *et al*, Phys. Rev. B **73**, 092514 (2006).

[33] M. Shi *et al*, Phys. Rev. Lett. , 047002 (2008).

[34] S. Souma *et al*, Rev. Sci. Instrum. **78**, 123104 (2007).

[35] A. Sugimoto *et al*, Phys. Rev. B. **74**, 094503 (2006).

[36] M. Le Tacon *et al*, Nature Physics **2**, 537 (2006).

[37] K. Tanaka *et al*, Science **314**, 1910 (2006).

[38] T. Timusk and B. Statt, Rep. Prog. Phys. **62**, 61 (1999).

[39] M. Vershinin *et al*, Science **303**, 1995 (2004).

[40] Z. Wang *et al*, Phys. Rev. B. **65**, 064509 (2002).

[41] J. Wei *et al*, Phys. Rev. Lett. **101**, 097005 (2008).

[42] W. D. Wise *et al.*, Nature Physics **4**, 696 (2008).

[43] W. D. Wise *et al.*, Nature Physics **5**, 213 (2009).

[44] S. Zhou *et al*, Phys. Rev. Lett. **98**, 076401 (2007).

Chapter 5

Pseudogap and charge density wave

5.1 Pseudogap

In last chapter we identified small gap (Δ_s) as superconducting gap. Here we address the question: what is the nature of this pseudogap? Usually the pseudogap is defined as the gap observed above the transition temperature and occurs mostly in the underdoped samples. There are many conjectures for the pseudogap state in hole-doped cuprates ranging from static order to fluctuating order of density waves in the particle-particle or the particle-hole channels. But recently there have been many reports on the observation of a second gap in the superconducting phase (below T_c)other than the superconducting gap.

Trying to understand the origin of the larger gap (Since the second typically large gap persists above T_c, we call this the "Pseudogap".)observed in our STM data, we obtain Fourier transforms of dI/dV maps at various energies. We find fourier spots representing a periodicity other than the atoms and/or supermodulation. Revisiting the dI/dV maps, we see where it comes from, as shown in Figure 5.4. There are patterns about 4 to 5 times the lattice constant. The Fourier transform of all energies data shows the pattern is non-dispersive and it represents a periodicity of $5a_\circ$. Figure 5.1 shows the FFT linecut marked on the inset FFT image. The fact that charge ordering has been observed in similar samples [3] [6] suggest that this pattern may due to charge ordering. Since a charge density wave (CDW) is expected to generate a CDW gap, is there any relationship between the large "pseudogap" and the CDW gap?

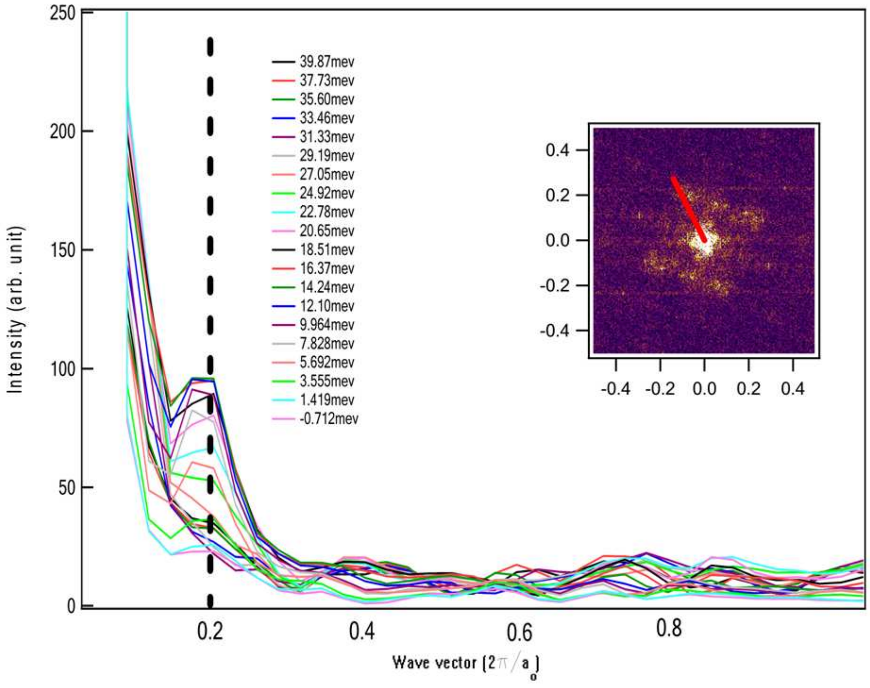

Figure 5.1: The linecut taken on the Fourier Transform images of 20 energies layers showing the 5a$_\circ$ periodicity is not dispersing. The position of the linecut is showed in the inset.

To claim that this is a charge density wave, we still need to answer two questions: (1) Is there any STM phenomenal evidence for CDW? (2) Is there any Fermi surface nesting effect because nesting is one of the well known driving force to form the CDW?

In STM studies, contrast reversal is an important signature for CDW. Figure 5.2 shows the conductance maps at high energies: 50mev,0meV and -50mev. And when we choose two random linecuts at both 50meV and -50meV conductance maps, we find there is clear contrast reversal, as shown in Figure 5.3. To answer the second question, we first obtain the corresponding wave vectors for both 0.4La and 0.1La sample, as shown in Figure 5.4. For 0.4La sample, the STM q vector matches well with the vector connecting the Fermi arc tip observed in ARPES data which is $2\pi/(5.2\pm0.7)$a$_\circ$. The Fermi surface nesting effect could potentially induce the charge density wave. The nesting vector matches the CDW pattern very well in both amplitude and direction. So we believe the charge density wave (CDW) may be the explanation for the patterns we observe.

In the overdoped 0.1La samples, the vector connecting the arc tip observed by ARPES ($2\pi/(7\pm0.5)a_\circ$) is expected to result in a spatial ordering with periodicity $\sim$27 $\mathring{A}$. Since the CDW displays short-range coherence, this larger periodicity is not likely to be sustainable. More importantly, the kinetic motion of the increasing number of doped holes is enhanced in the overdoped samples. Correspondingly, we find no clear CDW pattern at this doping and the large gap is suppressed in magnitude. The concomitant suppression of the large gap and the CDW pattern suggests an intimate connection between the two, even implying a likely causal relationship. The weak pseudogap in the overdoped samples could potentially arise either from CDW fluctuations or a static CDW that is too weak or disordered to be observed by STM.

Finally, CDW ordering is just one amongst many explanations for this pseudogap and while we cannot entirely rule out the possibility that the occurrence of the CDW is coincidental or a surface phenomenon.

5.2 STM measurement effect

5.2.1 Behavior of contrast reversal at low energy

In our conductance maps we observe a "Checkerboard" pattern at all energies on 0.4La [9] [13]. Now let's focus on the low energy data. Figure 5.6 shows the conductance maps at the energies: 7meV,0meV and -7meV. And when we choose a random linecut on the 7meV and -7meV conductance maps, we find there is no contrast reversal, as shown in Figure 5.7. To conclude, we observe a "checkerboard" pattern through all energies, but we only see the contrast reversal between opposite bias at high energies. There is no contrast reversal within the low energy states.

The observation of contrast reversal at high energies and no contrast reversal between low energies poses an immediate question. If the STM bias is chosen randomly, will the low energy states' pattern follow the positive high energy states or the negative ones. Are we confronting some logical difficulties? Furthermore we find a surprising behavior in the low energy patterns. Depending upon the sign of the bias the low energy pattern aligns itself with either the positive or negative bias [25] [24]. If we use a positive bias on the sample, then the low energy states follow the contrast of the negative high energy maps and show a reversed contrast from the positive bias maps. Similarly we use a negative bias on sample, the low energy states follow the

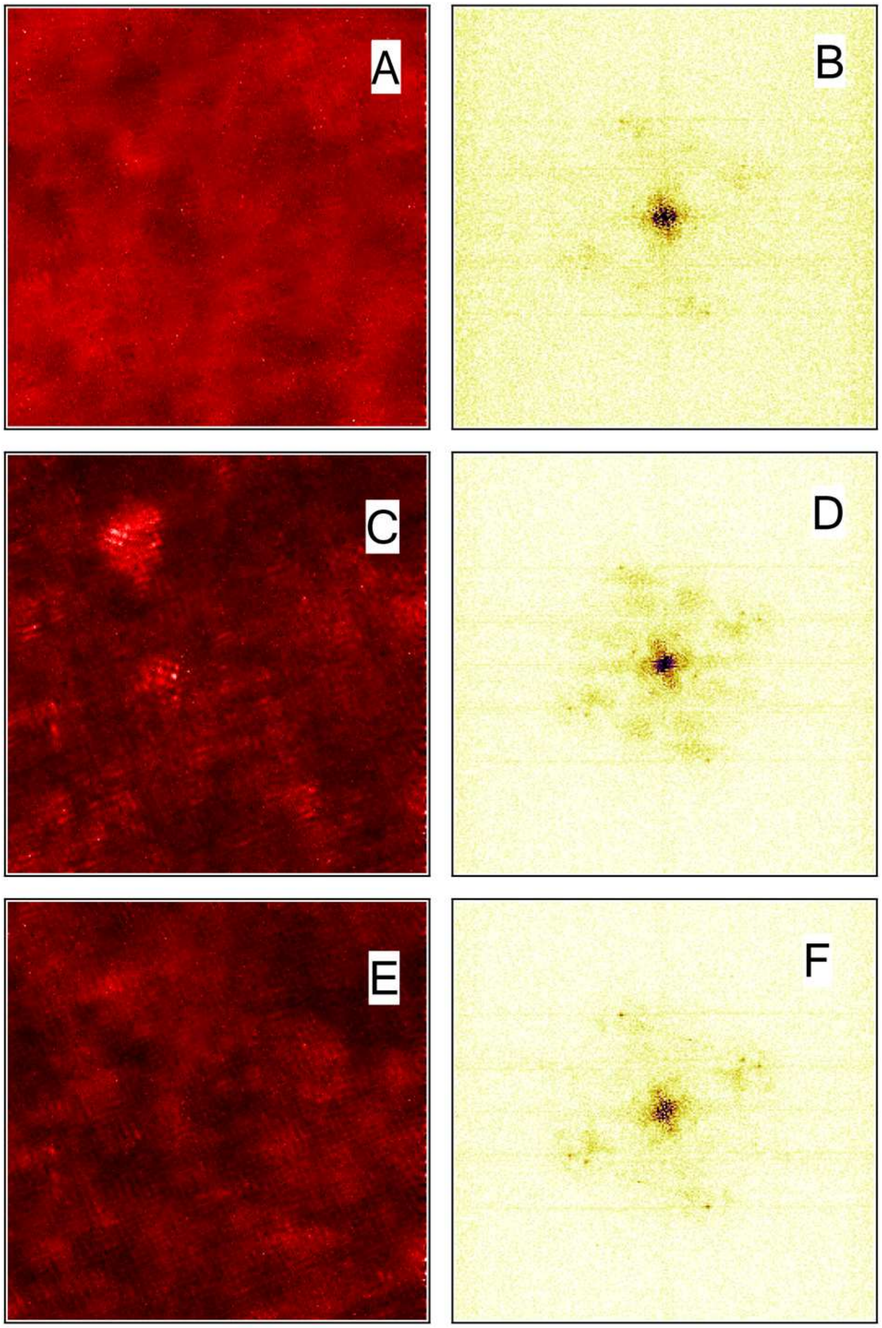

Figure 5.2: Conductance maps at (A) 50meV, (C) 0meV and (E) -50meV (256 Å× 256 Å) 0.4La sample. (B), (D) and (F) are the corresponding FFT image to (A), (C) and (E).

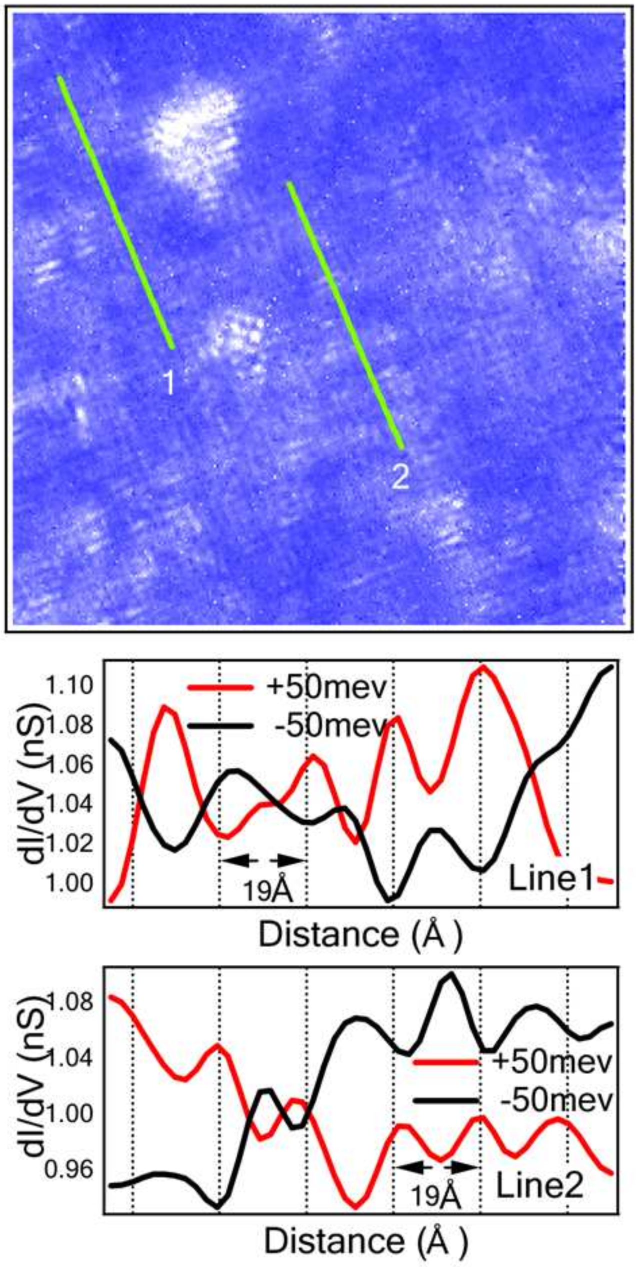

Figure 5.3: Two random linecuts showing clear contrast reversal taken at +50meV and -50meV. The position of the linecuts is marked on the inset topographic image.

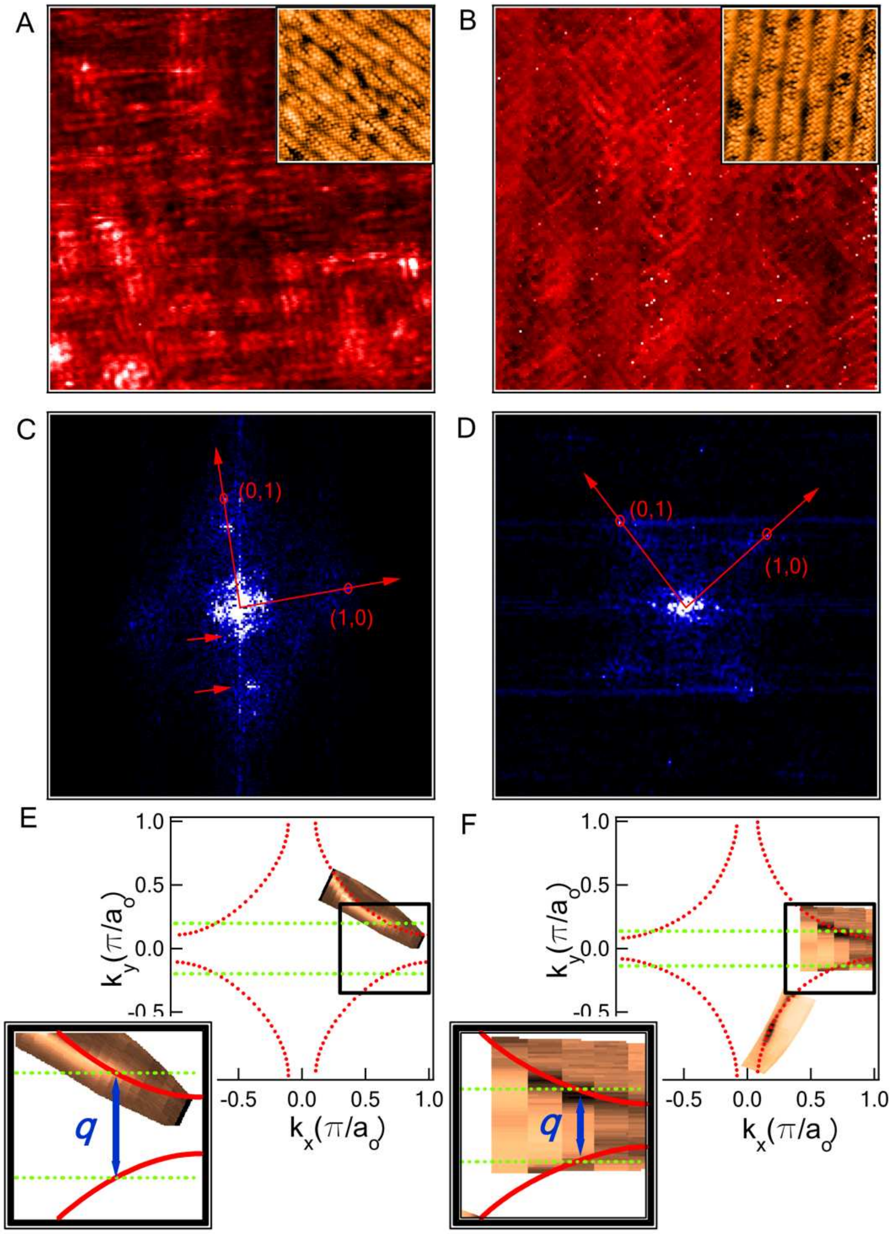

Figure 5.4: (A) 160 Å dI/dV map of 0.4La sample at energy (E)=+7meV. Inset shows simultaneous topography. (B) 160 Å dI/dV map of 0.1La sample at energy (E)=-11meV. Inset shows simultaneous topography. (C) Fourier transform of map in (A) showing the q vectors arising from the CDW pattern. The unit for the axis is $2\pi/a_\circ$ where lattice constant $a_\circ$=3.83Å. (D) Fourier transform of map in (B). (E) ARPES Fermi surface mapping of 0.4La sample. The inset shows the nesting vector at the arc tip which matches the average STM periodicity. (F) ARPES Fermi surface mapping of 0.1La sample showing the smaller q vector.

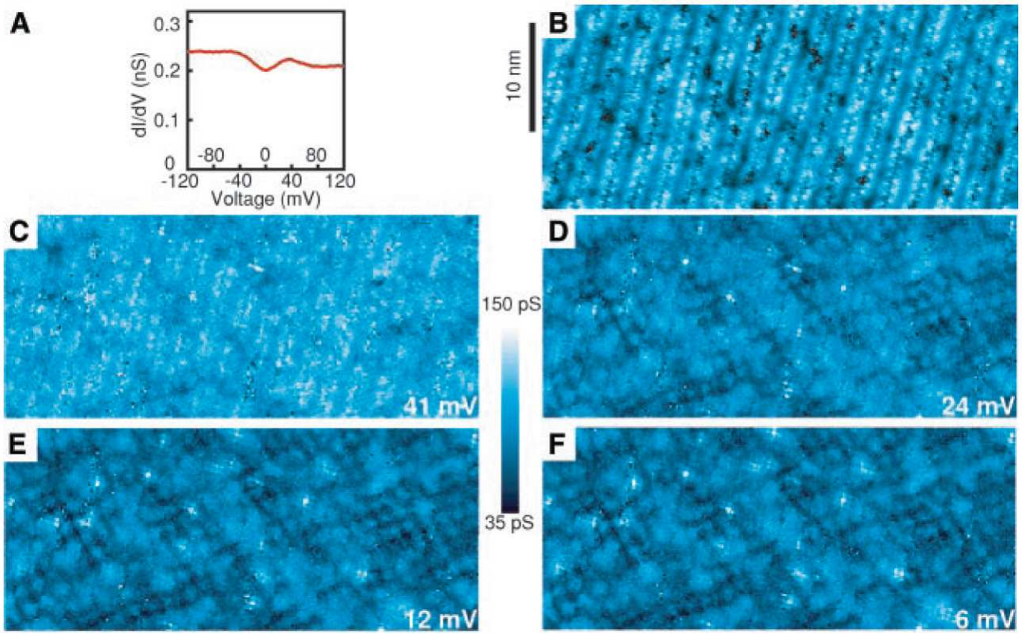

Figure 5.5: Energy and spatial dependence of the DOS of Bi2212 sample at 100K. (A) A typical conductance spectrum shows a pseudogap in the DOS at the Fermi energy. (B) A typical topograph. (C)-(F) Real space conductance maps recorded simultaneously at 41mV, 24mV, 12mV and 6mV show the appearance and energy evolution of DOS modulation along the Cu-O bond directions. From M. Vershinin *et al.* 2004. [28]

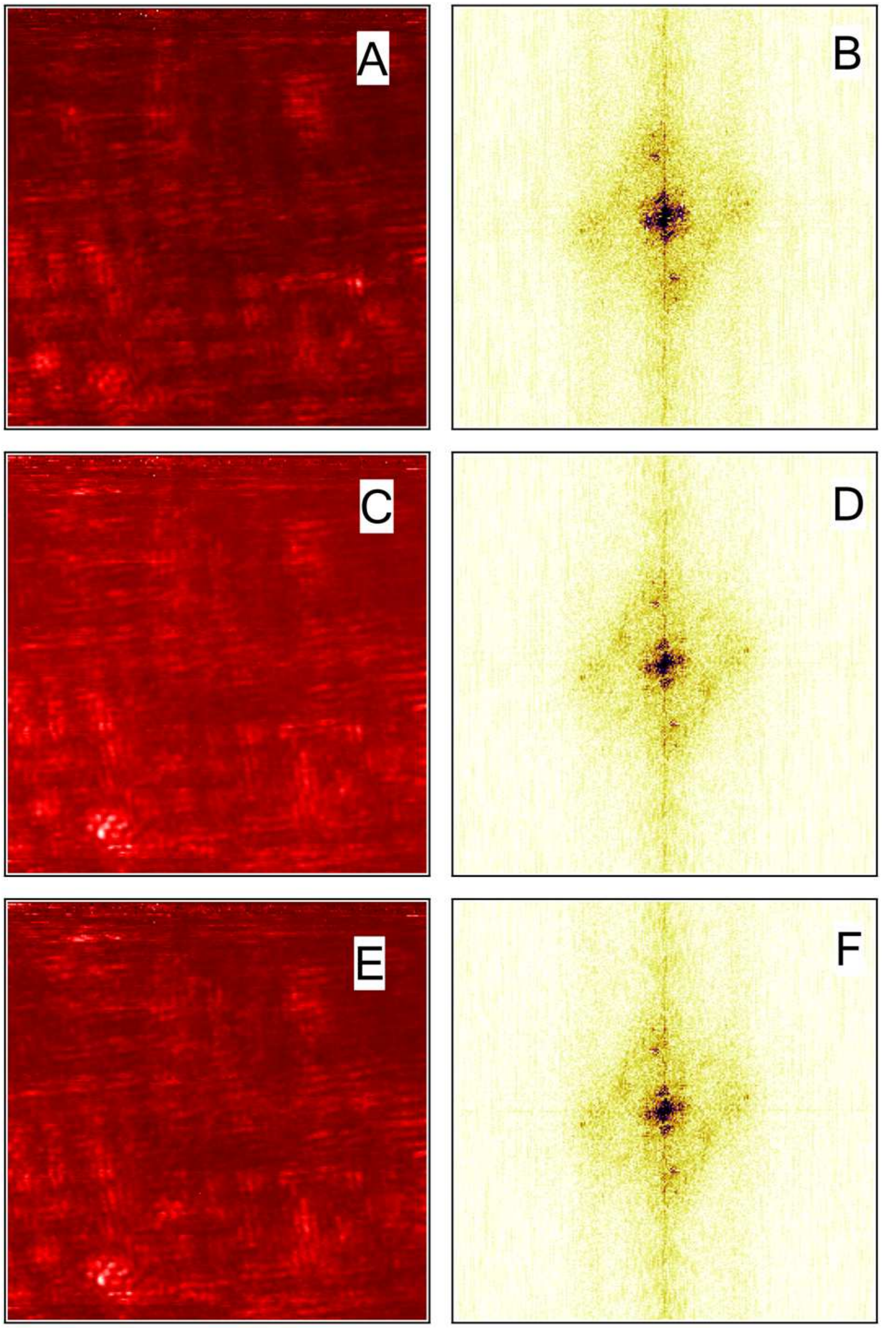

Figure 5.6: Conductance maps at (A) 7meV, (C) 0meV and (E) -7meV (200 Å× 200 Å) 0.4La sample. (B), (D) and (F) are the corresponding FFT image to (A), (C) and (E).

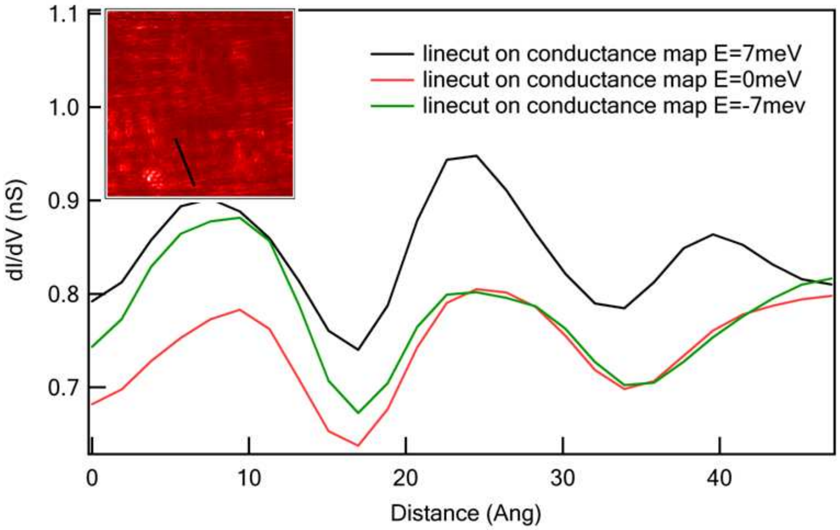

Figure 5.7: One random linecut showing clear contrast reversal taken at +7meV, 0meV and -7meV. The position of the linecut is marked on the inset topographic image.

positive high energy maps and are reversed from the negative high energy maps. Figure 5.8 shows the results when we using the negative bias, and the -50meV states has the strong contrast reversal with the last two layers: -30meV and -10meV. Figure 5.9 shows the similar results but using the positive bias, and the 40meV states has the strong contrast reversal with the last two layers: 20meV and 0meV.

5.2.2 STM measurement effect

Besides these interesting contrast reversal phenomena in last section, questions remain such as what is the nature of the "checkerboard" pattern at low energies? To explain our observations, we make the following proposal [29] [31]:

Our STM measurements are all under constant current mode which means during scanning, the tunneling current is kept in a constant value by the feedback loop. Since the tunneling current is determined by both LDOS and the tunneling range, once the LDOS is changing, the tunneling distance will be changing as well to keep the constant current. Therefore instead of the "Real LDOS", the data we collected is the "Observed LDOS" modified by the tunneling distance.

Here we use Figure 5.10 as a simple simulation. Spectrum in red represent the A

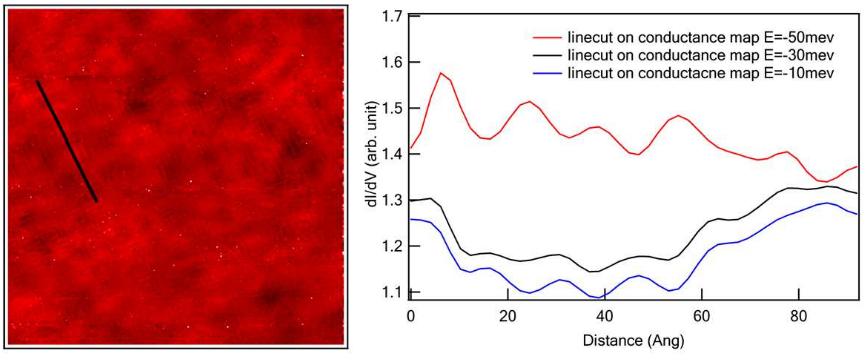

Figure 5.8: One random linecut showing clear contrast reversal taken at -50meV, -30meV and -10meV. The position of the linecut is marked on the inset topographic image.

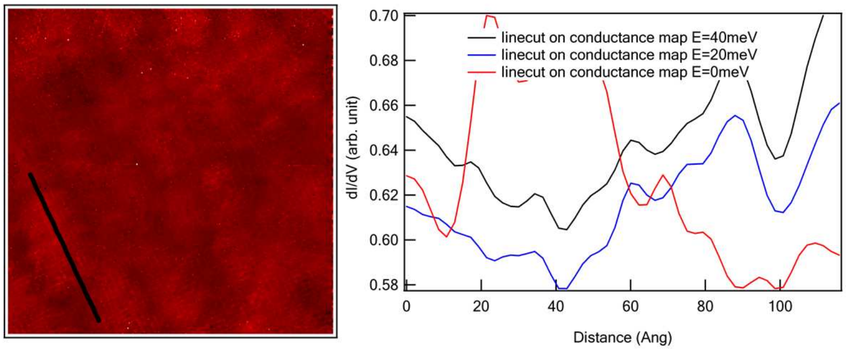

Figure 5.9: One random linecut showing clear contrast reversal taken at 40meV, 20meV and 0meV. The position of the linecut is marked on the inset topographic image.

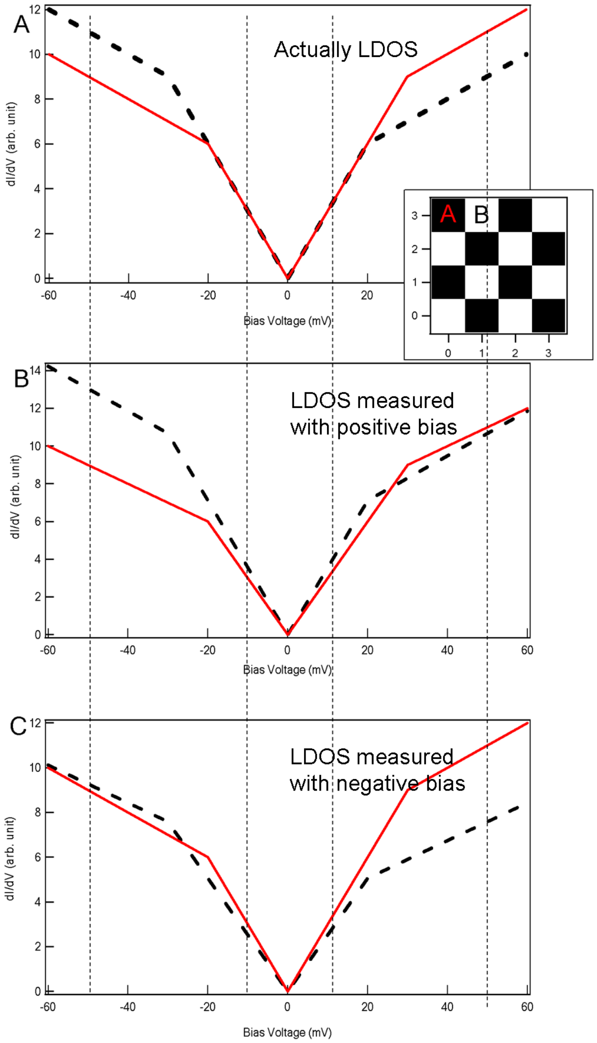

Figure 5.10: (A) Ideal DOS showing the CDW contrast reversal. Inset shows the corresponding dI/dV map. (B) Using positive bias setting so the two spectrum were normalized to the positive side spectral weight. (C)Using negative bias setting so the two spectrum were normalized to the negative side spectral weight.

spot in the inset simulated LDOS map while the spectrum in black represent the B spot. The map is at positive high energy (50meV). Black and white represent high and low intensity of the LDOS maps respectively. The tunneling current is in fact the integration of the conductance over the energy range. Under the positive bias, the two spectrum must be re-normalized to have the same tunneling current on the positive bias side. As we can see in the Figure 5.10(B), the contrast between A and B spot does not change at high energies after the re-normalization; it only become weaker at positive side and stronger at negative side. But the low energy maps now start to show a weak pattern which is new. A similar phenomenon occurs at the negative bias. In summary since the spectra are re-normalized to the negative side spectral weight, a contrast shows up at low energies, and the contrast becomes weaker at negative high energy side and stronger at positive high energy side.

The re-normalized LDOS map is shown in Figure 5.11. In this figure we use the same color scale for all the panels. The observed change in contrast matches our observation and be understood as one possible explanation for the appearance of the residue checkerboard effect at low energies.

To verify this proposal, we can do the normalization in reversal direction. By doing so, we should be able to recover the "constant height mode" data which should have no periodic feature at the low energies. However in reality we still see some murky periodic feature and the reason we believe is that the atomic feature in our data dominates the tunneling current.

A simple test of our proposal is to check if the CDW pattern is observed in the topography. By removing the atomic feature, we do find the CDW pattern at exactly periodicity and direction as in the conductance map, which supports our explanation for the residue checkerboard effect. Figure 5.12 shows the topographic image we obtained along with the conductance map. Because the sharp atomic features mask the CDW, we do not see the pattern clearly in the raw data. After blocking the spots representing the atoms and their satellite dots in the fourier image, the inverse FFT brings up the CDW pattern as expected.

While our explanation for the residue checkerboard effect certainly fits the data, it is possible that there are other explanations. More data and analysis are required to settle this issue.

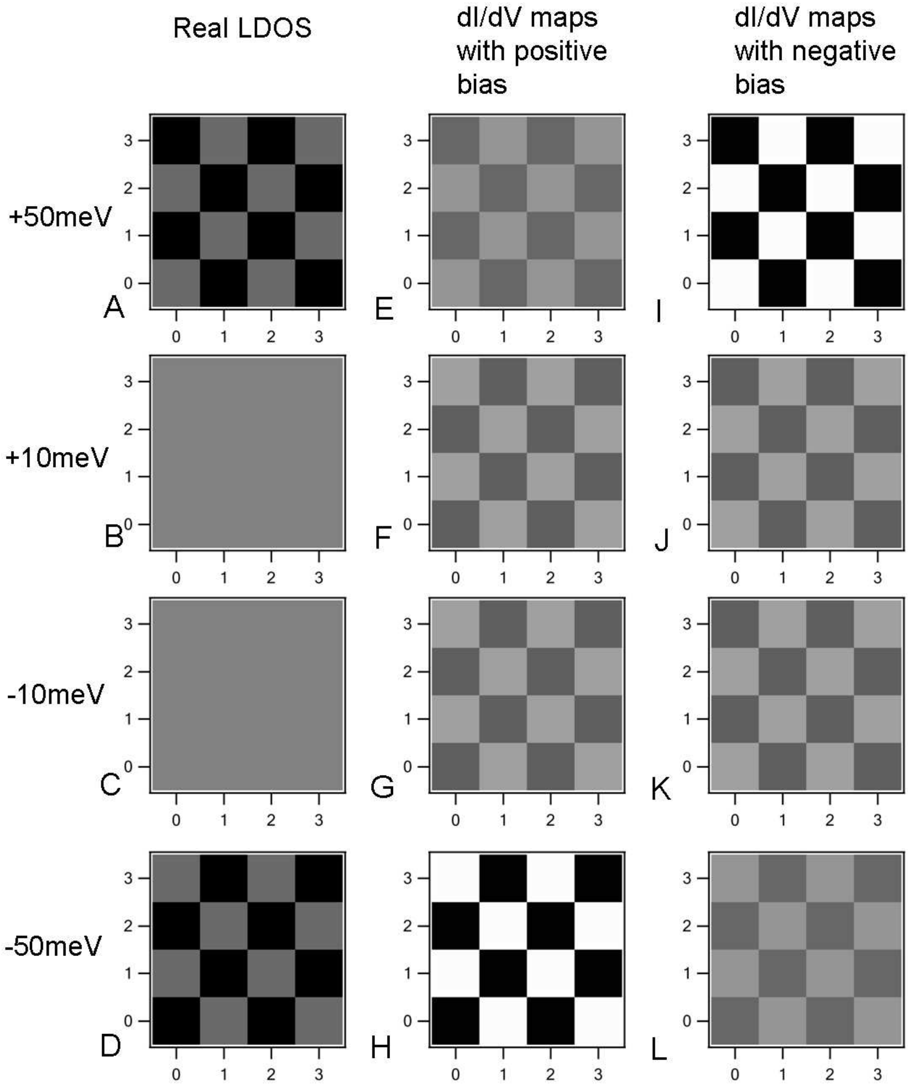

Figure 5.11: The real DOS at (A) 50meV. (B) 10meV. (C) -10meV and (D) -50meV. Using positive bias makes the conductance map to be re-normalized at (E) 50meV. (F) 10meV. (G) -10meV and (H) -50meV. Showing the last three layers has the same contrast but reverse to 50meV layer. Using negative bias makes the conductance map to be re-normalized at (I) 50meV. (J) 10meV. (K) -10meV and (L) -50meV. Showing the first three layers has the same contrast but opposite to -50meV layer.

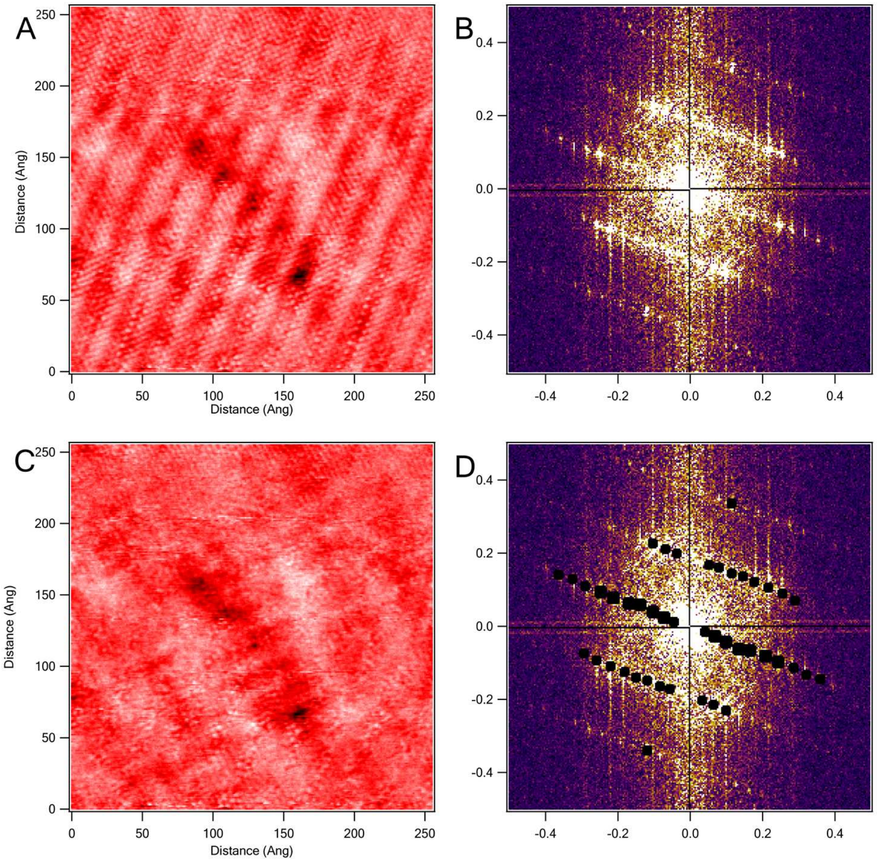

Figure 5.12: (A) The raw data of STM topographic image. (B) The Fourier Transform image corresponding to (A). (D) FFT image in which we masked the atomic and supermodulation feature. (C) Inverse FFT of (D) showing clear pattern hide underneath the atomic and supermodulation features.

5.3 Comparison with "checkerboard pattern" of Bi2212

We now make a comparison to the Bi2212. Since the CDW pattern observed here looks like the checkerboard feature of Bi2212, it is possible that they are all associated with the charge ordering. In paper published by McElroy *et al.* [16] as shown in Figure 5.13, The authors claimed to observe a checkerboard only at low energies. They first setup a gap value of 65mev as the threshold. By doing fourier transform of the integrated conductance map above and below this energy, they observed two different phases respectively: the one with the "checkerboard" fourier spot and the one without.

The similarity between their data and ours make us believe there is an unified scenario in both Bi2212 and Bi2201 materials i.e. there are two coexisting and competing phases below T_c. The difficulty is how to distinguish between these two phases. In Bi2201, we clearly have two different energy scales corresponding to the two phases. The large gap which associated with the pseudogap phase is well separated from the superconducting phase. So it is easier to see the spatial difference below and above the pseudogap energy scale. In Bi2212, it is more difficult since these two gaps are not well separated according to ARPES results. The threshold of 65meV for Δ helps to separate these two phases [6] [7] [5] [10] [4] [26].

5.4 Summary

dI/dV maps on La-Bi2201 observed a pattern whose periodicity is about five times lattice constant and not energy-dispersive. Based on the contrast reversal evidence at the high energies, we believe this is charge density wave. By making the comparison with the ARPES Fermi surface nesting vector, we think the charge density wave can be a possible explanation for the pseudogap.

Besides the "checkerboard" pattern observed at high energy states, we also observed the pattern at the low energies, where there is no contrast reversal. In this case we propose that the pattern is mainly due to the STM setup condition that demand a constant current at every point. By comparing to a similar "checkerboard" feature of Bi2212, we believe that a unified picture emerges for the cuprates when there are two coexisting and competing phase below T_c.

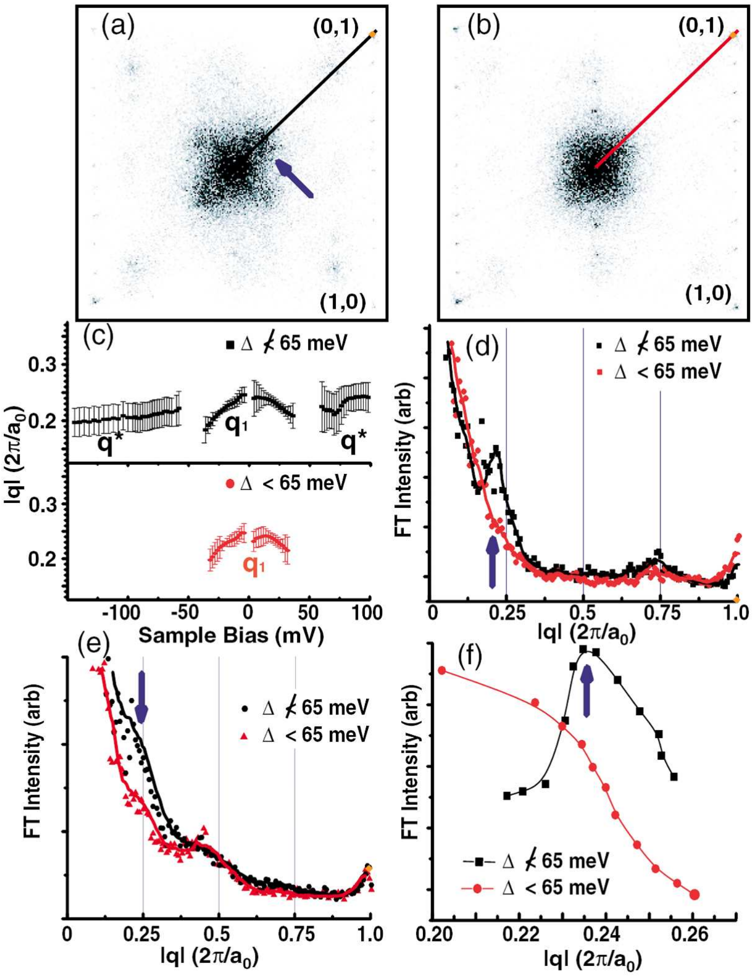

Figure 5.13: (A) FT of integrated conductance map from E=-65meV to E=-150meV. (B) FT of integrated conductance map from E=-65mev to E=+65meV. (C)Dispersion of $\vec{q}_1$ in regions with dSC coherence with ZTPG spectra. $\Delta<$65meV (red circles) and in regions with ZTPG spectra for $\Delta<$36meV (black squares). At low energies the dispersive LDOS modulation q_1 are identical in the two regions. For E>65meV, a new wave vector, $\vec{q}^{*}$, modulation is found only in the ZTPG regions (black). To within our uncertainty they do not disperse and $\vec{q}^{*}=(\pm 2\pi/4.5a_\circ,0)$, $(0,\pm 2\pi/4.5a_\circ)$. (D) The magnitude of the integrated conductance map along the $\vec{q} \| (\pi, 0)$ direction for $\Delta\not<$65meV ($\Delta<$65meV) black (red). (E) The magnitude of the FFT of the masked topographic image along the $\vec{q} \| (\pi, 0)$ direction for $\Delta\not<$65meV ($\Delta<$65meV) black (red). (F) A plot of the amplitude of the $\vec{q}_1$ LDOS modulation as a function of $\vec{q}_1$. The maximum intensity of the modulation in the ZTPG regions occurs at $\vec{q}_1=2\pi/4.5a_\circ$. No enhanced scattering of the quasiparticle in the dSC regions (red) is seen. From McElroy *et al.* 2005. [16]

Bibliography

[1] J. M. Carpinelli *et al*, Nature **381**, 398 (1996).

[2] H. L. Edwards *et al*, Phys. Rev. Lett. **73**, 1154 (1994).

[3] G. Gruner and A. Zettl, Phys. Rep. **119**, 117 (1985).

[4] W. Guyard *et al*, Phys. Rev. B **77**, 024524 (2006).

[5] T. Hanaguri *et al*, Nature **430**, 1001 (2004).

[6] T. Hanaguri *et al*, Nature Physics **3**, 865 (2007).

[7] J. E. Hoffman *et al*, Science **297**, 1148 (2002).

[8] J. Hoffman *et al*, Science **295**, 466 (2002).

[9] Howald *et al*, Phys. Rev. B **67**, 014533 (2003).

[10] S. Hufner *et al*, Rep. Prog. Phys. **71**, 062501 (2008).

[11] T. Kondo *et al*, Phys. Rev. Lett. **98**, 267004 (2007).

[12] W. S. Lee *et al*, Nature **450**, 81 (2007).

[13] J.-H. Ma *et al*, Phys. Rev. Lett. **101**, 207002 (2008).

[14] T. Machida *et al*, Journal of the Physical Society of Japan **75, 8**, 083708 (2006).

[15] P. Mallet *et al*, Phys. Rev. Lett. **73**, 1154 (1994).

[16] K. McElroy *et al*, Phys. Rev. Lett. **94**, 197005 (2005).

[17] K. McElory *et al*, Nature **422**, 592 (2003).

[18] A. J. Millis *et al*, Science. **314**, 1888 (2006).

[19] H. Morikawa *et al*, Phys. Rev. B **70**, 085412 (2004).

[20] L. Niestemski *et al*, Phys. Rev. Lett. **102**, 107001 (2009).

[21] M. R. Norman *et al*, Phys. Rev. B **76**, 174501 (2007).

[22] S. H. Pan *et al*, Nature **413**, 282 (2001).

[23] R. E. Peierls Quantum Theory of Solids. **Clarendon Press**, Oxford (1955).

[24] W. Sacks *et al*, Appl. Phys. A **A 66**, S952 (1998).

[25] W. Sacks *et al*, Phys. Rev. B **57, 20**, 13118 (1998).

[26] M. Le. Tacon *et al*, Nature Physics **2**, 537 (2006).

[27] A. Tomic *et al*, ArXiv: 0808.2638.

[28] M. Vershinin *et al*, Science **303**, 1995 (2004).

[29] Z. Wang *et al*, Phys. Rev. B. **65**, 064509 (2002).

[30] W. D. Wise *et al.*, Nature Physics **4**, 696 (2008).

[31] J. X. Zhu *et al*, Phys. Rev. Lett. **89,6**, 067003 (2002).

Chapter 6

Technical notes

In this chapter, we will review some technical notes collected during the construction and operation of the STM systems. Some notes are also from the data-acquisition and analysis.

These notes are important not only for the experiments on STM system, but also can be referred to other experimental techniques in the field of condensed matter physics.

6.1 Introduction to charge density wave

The charge density wave is one of the usual phase can be found in many materials. The easiest way to understand CDW is the one dimensional model proposed by Peierls [1] [2] [3]. Figure6.1 shows the schematic drawing of the basic idea.

A one dimensional chain of atoms, with lattice constant a, has a dispersion relation as pictured in Figure6.1 A. In the case of half-filling, electrons will occupy those states within $\pm \mathrm{K}_F$, out to the Fermi wave vector k_F (half the Brillouin zone). The electronic energy of this system can be significantly reduced, however, if the edge of the Brillouin zone were to be brought into coincidence with the Fermi wave vector (in this case, if it were cut in half). This can occur, as pictured in Figure6.1 B, if every other atom in the chain is displaced slightly from its equilibrium position. In that case, the unit cell is doubled (now with lattice constant 2a) and the Brillouin zone is halved. The gap that opens at the edge of the Brillouin zone now has the effect of significantly lowering the energies of the occupied states (and raising the energies of the unoccupied states), thus reducing the overall energy of the system.

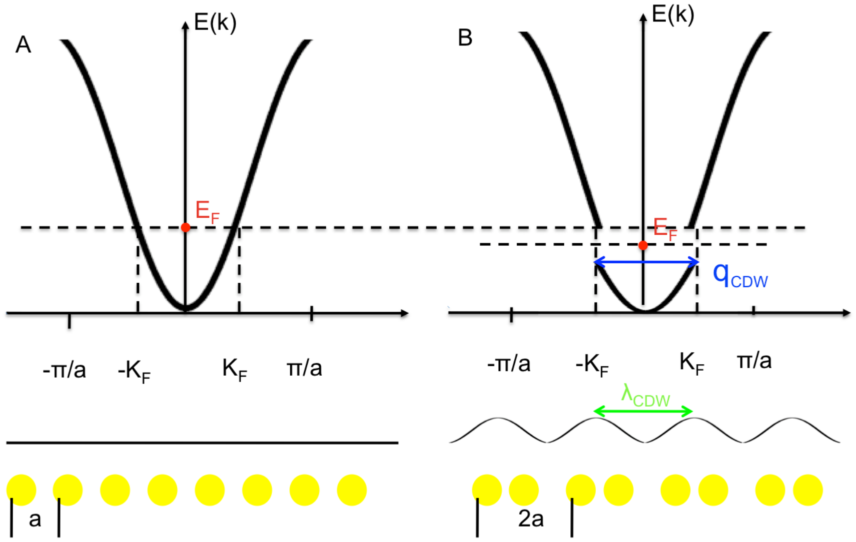

Figure 6.1: (A) A 1D material at half filling. (B) A periodic lattice distortion occurs, inducing a charge density modulation with wave vector $q_{CDW}=2K_F$, then a gap opens up about the fermi energy,reducing the energy of the filled electron states.

Charge density waves can in general form in any system where the presence of a periodic lattice distortion, which costs potential energy, leads to a more than offsetting reduction of the electronic energy by opening a gap at the Fermi energy. As there is a strong relationship between the wave vector of the charge density wave q_{CDW} and the Fermi wave vector k_F ($q_{CDW}\sim 2\ k_F$), CDW's occur most often in materials whose Fermi surfaces are nested, that is, whose Fermi surfaces have fairly flat, parallel portions. In these cases a single CDW wave vector can gap more of the Fermi surface, and thus produce a larger energy reduction.

Usually CDW is accompanied by a periodic lattice distortion with the presence of the charge density modulation. Also CDW is accompanied by a gap in the density of states.

$NbSe_2$ along with $CeTe_3$ [5] are the some of the famous material which have the obvious CDW state, and there are also a lot of high temperature Superconductivity were reported to have the similar CDW states, for instance, the checkerboard charge modulation found in large gap regions/underdoped Bi2212 [7], KMoO samples [4] and the YBCO samples [8]. Here we will try to find the signature of CDW in our study: 0.4La and 0.1La of $La_xBi_2Sr_{2-x}CuO_{6+\delta}$ samples. Some similar results are also presented recently [9] [6].

6.2 Tip preparation

The STM tips for the present study in this thesis were made of 20 mil Pt/Ir (0.85/0.15) wires by hand cutting. During our experiments, we have tried a number of tips made of different materials and different preparation procedures.

To image a flat sample, such as that of a highly ordered pyrolytic graphite (HOPG), and the Bi2201 samples we studied in this thesis. a simple mechanically cut tip can produce good atomic images as long as the apex of the tip is free of undesirable atoms or molecules. To avoid the future oxidization, we choose the inert metals such as Pt/Ir wires and Pt/Rd wires.

Besides the cutting, electrochemical etching is the other important method to yield sharp and high quality tips [10]. After the tips are pulled out of the chemical solution, certain cleaning procedure such as cleaning with saturated hydrochloric acid (HCl) or field emission should be followed to remove the unwanted materials. The etch tungsten tips are proved to be very stable probes compared to mechanically cut tips. Some scanning electron microscopy (SEM) images of the tips are shown in Figure 6.2.

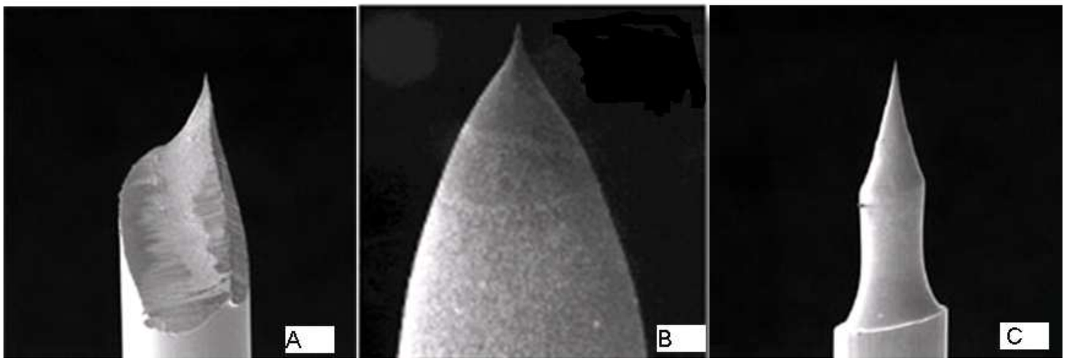

Figure 6.2: (A) SEM image of Pt/Rd cut tip. (B) SEM image of Pt/Ir etched tip. (C) SEM image of W etched tip.

Besides the W and Pt/Rd tips, other materials are also been used for STM study. Recently there is also proposed the bulk Cr tips can be used for spin-polarized STM and yields high quality and high resolution results. that also confirms that different tips suit different samples [12].

6.3 Piezo calibration

To calibrate the shear piezos of the coarse approach motor, a Michaelson interferometer is set up to measure both their polarization and displacement coefficient. Among all piezos, we pick those with similar coefficients for the STM head construction.

For the fine motion, a 0.125" O.D., 0.19" long, 20 mil thick EBL2 tube serves as our STM scanner. To calibrate the piezo tube scanner, atomic resolved images on HOPG are taken at room temperature, 100K and 4.2K. (Figure 6.3)

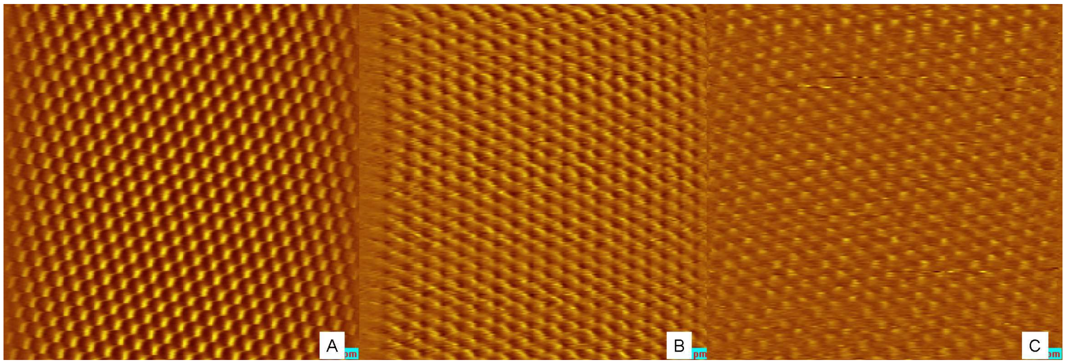

Figure 6.3: (A) STM topographic images of HOPG at room temperature (50 Å× 50 Å). (B) at 100K (50 Å× 50 Å).(C) at 4.2K (50 Å× 50 Å).

Knowing the lattice constant of HOPG, we then extract the piezo coefficient for lateral scanning. Notice that the coefficient decreases linearly with decreasing temperatures. Therefore, at any intermediate temperatures, a simple linear interpolation is sufficient to re-scale the STM data.

Also the topographic images of $NbSe_2$ sample can be used to calibrate the piezo coefficient as well because of it's well known lattice constant although people studied $NbSe_2$ mostly because its vortex states [11]. Figure 6.4 shows the topographic images we acquired under similar experimental environments as we used in $La_xBi_2Sr_{2-x}CuO_{6+\delta}$ samples

6.4 Noise Measurement and control

Noise measurement and control is always one of the center issue of scanning tunneling microscopy system construction and operation. To measure the noise's frequency and amplitude, several ways can be applied, the most used way is the accelerometer (or

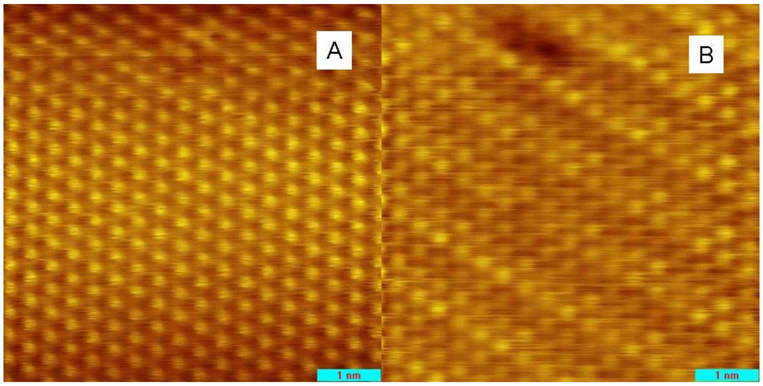

Figure 6.4: (A) STM topographic images of $NbSe_2$ at 4.2K (60 Å× 60 Å) using negative bias on sample. (B) using positive bias on sample.

called Geophones). By doing FFT on the noise signals, we got s power spectrum which we can tell the frequency and amplitude. Figure 6.5 shows the FFT of our noise data, the noise spectrum were acquired from the tunneling current. By getting rid of the biggest noise peaks, we can proceed with our experiments.

The noise can from different sources, according to its driving force, we attribute them into two basic categories: Mechanical Noise and electronics noise. They also can tell from the frequencies.

The mechanical noise usually comes from the vibration of the building, system setup, operation shaking and the environmental audio noise. The typical frequencies are from a few Hz (floor vibration), dozens Hz (system operation shaking) to a few hundreds Hz (Environmental audio noise).

To decrease the mechanical noise as much as possible, people usually set up the lab in the lower level or basement of the building and the STM room should be isolated and sound proof. Also a special set of vibration isolation system should be provided such as a sound table or springs. Figure 6.6 shows one of the commercial vibration isolation table which we use in our STM system.

The electronics noise are much more complicated. Beside the easy-telling 60Hz noise (AC power), the grounding loop can easily introduce the electronics noises.

Here we will discuss three special and important sources of the electronics noise:

(1) Crosstalk refers to a signal transmitted on one circuit or channel of a transmission system creates an undesired effect in another circuit or channel. Crosstalk is usually caused by undesired capacitive, inductive, or conductive coupling from one

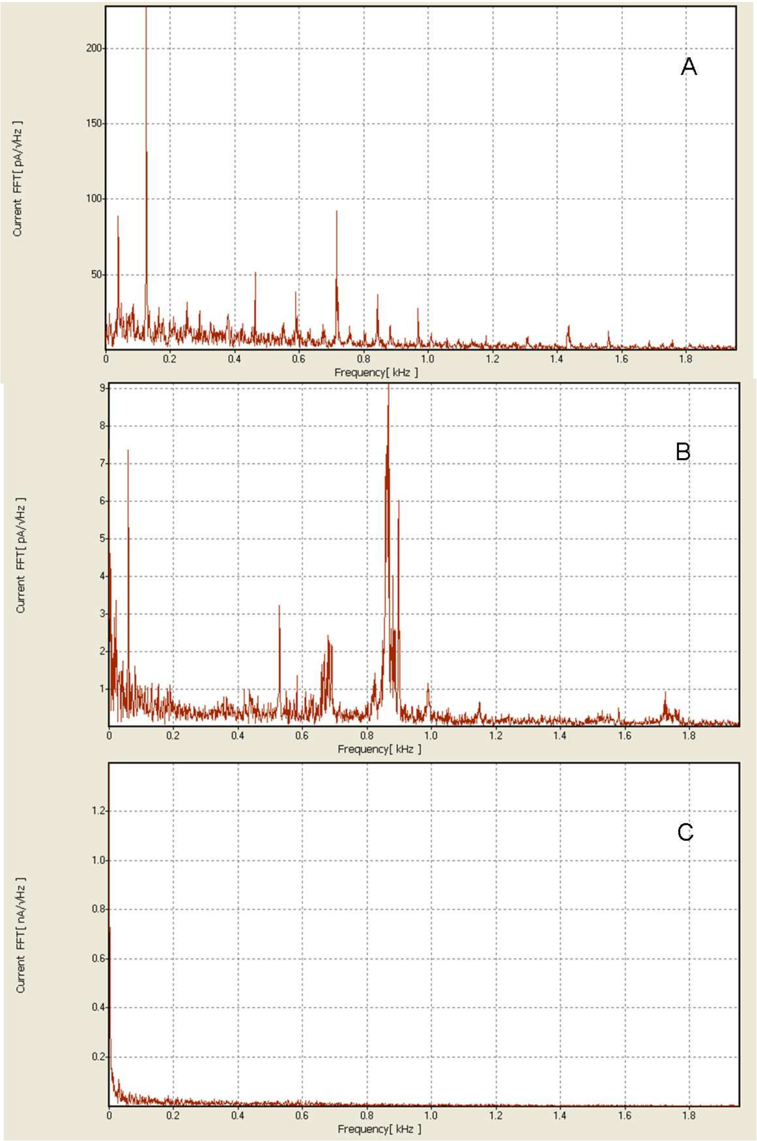

Figure 6.5: (A) FFT noise spectrum showing huge noise. (B) FFT noise spectrum showing noise improved from (A). (C) FFT noise spectrum showing noise level during the experiment after getting rid of the noise on (B).

Figure 6.6: TMC Active Vibration Isolation Tables 20 series.

circuit, part of a circuit, or channel, to another. In STM case, the tunneling current wire can be very close to the piezo tube which have a few wires carrying high voltage, high frequency signals, so the tunneling current wire need to be separated from the other parts very well.

(2) Feedback oscillation is another common case when the feedback look is taking control improperly, it's not a single noise source but usually coming with some noises with different frequencies. But the feedback loop will amplify this noise effect to unacceptable situation.

(3) Radio frequency noise (also called electromagnetic interference) is another unwanted disturbance that affects an electrical circuit due to either electromagnetic conduction or electromagnetic radiation emitted from an external source. And since the RF noise can not be killed from the source, RF filter can be applied here to reduce the amplitude.

Last thing need to be addressed is the preamplifiers. All voltage amplifiers can have a cutoff frequency (also called bandwidth), a carefully selected range can get rid of noise and keep the signal, easily improve the signal noise ratio.

6.5 Pumps

A brief introduction to the main kind of pumps is presented below:

Mechanical pump A typical mechanical pump consists of an inlet, and an exhaust with a one-way valve, and an off-center rotating piston in a cylindrical cavity. When the piston rotates, gas is pulled into the cavity, and then forced out through the exhaust port. The rotating piston has spring-loaded vanes to create a seal with the cavity wall. The seal, and the exhaust port valve, are lubricated with a low-vapor-pressure oil (Oil need to be filled constantly to avoid the damage caused by the friction when running out of oil). Also there is design for a two-stage mechanical pump which consists of two pumping cavities in series to achieve a lower vacuum pressure.

Accessories of a pump are a mist filter (or vent) to trap oil mist in the pump exhaust, and a trap to prevent oil vapor from backstreaming into the volume being evacuated [13].

There is Diaphragm pump also named dry pump or membrane pump and can do the same rough pumping as the mechanical pump (oil pump) mentioned above.

Turbo pump Turbomolecular pumps use a series of high-speed rotors (25,000 to 75,000 rpm) and flow stabilizing, stationary stators to impart a preferential motion to gas molecules and create molecular flow through the pump.

A turbomolecular pump mechanism cannot exhaust directly to atmosphere and thus requires a backing pump such as a scroll or oil sealed rotary vane pump to reduce the pressure in the exhaust of the turbo pump. The turbo inlet is typically connected directly to a vacuum chamber and the exhaust is fed into a backing pump [13].

Ion pump Ion pumps utilize a sputtering process to ionize gas molecules and embed them into anode or cathode wall. The entrainment process can utilize a getter such as titanium to bind and bury the molecules. They can operate in the ultra high vacuum range and eliminate contamination by organic molecules.

Sputter ion pumps operate by ionizing gas within a magnetically confined cold cathode discharge. Burial is the basic means of pumping heavy noble gases. Argon ions neutralized via glancing collisions with a sputter cathode impact the pump wall and are coated with sputtered titanium. Triode pumps are specially designed to maximize the kind of collisions that produce energetic neutrals [13].

Sublimation pump Getter or titanium sublimation pumps (TSP) entrain gas molecules in a getter, or material that is vaporized in order to absorb or capture the molecules, and embed them on the cold outer wall of a chamber. One can also use non-evaporating Gettering sorption technique by using a large-surface-area porous matrix for entrainment [13].

Cryogenic pump Cryogenic pumps utilize extremely cold (liquid N_2 and He temperatures) surfaces and absorption surfaces to freeze or trap molecules. Cryogenic pumps can operate with relatively high force or exhaust pressures. Cryogenic pumps must be periodically re-generated to purge the frozen or trapped gases. Cryosorption pumps evacuate gas molecules from a volume by adsorbing them on the chilled surface of a molecular sieve. These molecular sieves are designed to have a large surface area-to-volume ratio to maximize the adsorbing area [13].

In our STM system, the cold stage is automatically working as a cryo pump. So when the pressure of main chamber (2nd stage) is about 1E-10 Torr, the STM head area (3rd stage) is in much better vacuum.

We are lucky to have all of the pumps mentioned above to help to improve the vacuum of our system, and the lowest vacuum we achieved at this system was 2E-11 Torr in the main chamber.

6.6 Pressure gauges

A brief introduction of two main kind of pressure gauges: Pirani gauge and Ion gauge.

Pirani gauge Pirani gauge works from 100 Torr to 10E-3 Torr. Arguably it is the most common gauge used in surface science for measurement at the high pressure end of the scale. The physical principle underlying the operation of a pirani gauge is the pressure dependence of the thermal conductivity of a gas below a pressure of ∼100 Torr. (Above 100 Torr thermal conductivity of a gas does not vary with pressure because the increase in the number density of molecules is exactly compensated by a reduction in the mean free path. However the smaller number density of molecules at lower pressures means that the kinetic model picture of heat transfer as being due to colliding molecules breaks down.)

The setup of the pirani gauge can be described as following: A metal filament, usually tungsten, is held within a metal tube connected to the vacuum system and is heated by an electric current. The variation of the filament temperature (and thus its resistance) with pressure is monitored using a simple Wheatstone bridge set-up.

Ion gauge Ion gauge measures the pressure of 10E-3 Torr to 10E-11 Torr). Its operation is based on the ionization of molecules via a sufficiently high energy electron beam. The ionization rate and thus the ion current (I+) is directly dependent on the gas pressure.

The ion Gauge consists of three distinct parts, the filament, the grid, and the collector. The filament is used for the production of electrons by thermionic emission. A +V charge on the grid attracts the electrons away from the filament; they circulate around the grid passing through the fine structure many times until eventually they collide with the grid. Gas molecules inside the grid may collide with circulating electrons. The collision can result in the gas molecule being ionized. The collector inside the grid is -V charged and attracts these +V charged ions. Likewise they are repelled away from the +V grid at the same time. The number of ions collected by the collector is directly proportional to the number of molecules inside the vacuum system. By this method, measuring the collected ion current gives a direct reading of the pressure.

6.7 List of some vendors

Here we list some of the manufacturers and distributors for the reference reason:

Scanning tunneling microscopy system
—Omicron
—RHK
—Unisoku

UHV parts
—VG
—Nor-cal
—Fisher
—Pfeiffeer
—Varian
—Kurt J. Lesker

—MDC

Cryogenics System
—LakeShore Cryotronics, Inc
—AMI

Vibration Isolation system
—Technical Manufacturing Corporation

Sample preparation
—Varian: Torr-Seal
—EPOXY Technology, Inc: Ag Epoxy

Elements, Ceramics and wires
—Alfa Aesar
—Ceramic Products
—California Fine Wire
—Staveley Sensor, Inc: Pizeo stacks/tube
—FerroCeramic, Inc: Macor parts
—Amphenol
—Belden

Electronics, Instruments
—D.L instruments
—Stanford Research system: Lockin Amplifier

Miscellanies
—McMaster
—Small parts, Inc
—Newark in One
—Digikey

Bibliography

[1] R. E. Peierls Quantum Theory of Solids. **Clarendon Press**, Oxford (1955).

[2] J. M. Carpinelli *et al*, Nature **381**, 398 (1996).

[3] H. Morikawa *et al*, Phys. Rev. B **70**, 085412 (2004).

[4] P. Mallet *et al*, Phys. Rev. Lett. **73**, 1154 (1994).

[5] A. Tomic *et al*, ArXiv: 0808.2638.

[6] T. Machida *et al*, Journal of the Physical Society of Japan **75, 8**, 083708 (2006).

[7] Howald *et al*, Phys. Rev. B **67**, 014533 (2003).

[8] H. L. Edwards *et al*, Phys. Rev. Lett. **73**, 1154 (1994).

[9] W. D. Wise *et al.*, Nature Physics **4**, 696 (2008).

[10] I. Ekvall *et al*, Meas. Sci. Technol. **10**, 11-18 (1999).

[11] Ch. Renner *et al*, Phys. Rev. Lett. **67**, 1650 (1991).

[12] A. Li. Bassi *et al*, Appl. Phys. Lett. **91**, 173120 (2007).

[13] http://vacuum-pumps.globespec.com